

**Ambient seismic noise tomography
of the Antarctic continent**

Presentata da: Paride Legovini

Supervisore

Prof. Alberto Armigliato

Co-supervisore

Prof. Andrea Morelli

Coordinatrice dottorato

Prof. Nadia Pinardi

Contents

List of Figures	v
List of Tables	ix
Abstract	11
Acknowledgements	15
1 Antarctic Seismology	17
1.1 General notions on Antarctica	17
1.2 Seismicity of the Antarctic plate	25
1.3 Seismography in Antarctica	28
1.4 Field work	33
2 Noise interferometry	45
2.1 Seismic noise	45
2.2 From noise to the Green's function	47
2.3 The phase cross-correlation	55
2.4 The phase-weighted stack	57
3 Modelling surface waves	63
3.1 Surface waves	63
3.2 Group and phase velocity measurements	71
4 Data retrieval and processing	75
4.1 Introduction	75
4.2 Raw data operations	77
4.3 Preprocessing	81

4.4	Cross-correlation and stacking	82
4.5	Velocity measurements	87
4.6	Convergence measurements	91
4.7	Seasonal variations	95
5	Inversion	99
5.1	Seismic tomography	99
5.2	Tomographic inversion	102
5.3	Velocity maps and profiles	106
6	Conclusions	119
A	Hermes: technical documentation	121
	Bibliography	129

List of Figures

1.1	Antarctica overview map	18
1.2	The Bedmap2 bed elevation model	20
1.3	Antarctic territorial claims	20
1.4	West and East Antarctica	21
1.5	Broad geological structure of Antarctica	23
1.6	Antarctic surface temperature	23
1.7	Countries maintaining antarctic stations	24
1.8	Research stations in the Antarctic	24
1.9	Aerial view of Mario Zucchelli Station	26
1.10	Aerial view of Concordia Station	26
1.11	2000–2010 seismic events with $M_W \geq 6$ south of 50° S	27
1.12	Seismic arrays in Antarctica	30
1.13	The Terra Nova Bay observatory	31
1.14	The Concordia observatory	33
1.15	The Starr Nunatak station	34
1.16	The 1 January 2016 peri-Antarctic earthquake	35
1.17	The TNV new acquisition system	36
1.18	TNV: data acquisition diagram	39
1.19	TNV: power system diagram	40
1.20	Diagram of the Hermes system	43
2.1	One day of seismic record	46
2.2	PSD for QSPA between 2007 and 2012	48
2.3	A diffuse noise field	52
2.4	Seismic interferometry: principle	52
2.5	An ideal noise cross-correlation	53

2.6	Classic seismic interferometry workflow	54
2.7	A stack of cross-correlations	55
2.8	How the PCC behaves differently	58
2.9	PCC+PWS seismic interferometry workflow	60
2.10	Comparison between classic techniques and PCC/PWS	61
3.1	Arrival of body and surface waves	64
3.2	Velocity of seismic waves in the Earth versus depth	66
3.3	PREM's main parameters	68
3.4	PREM dispersion curves	69
3.5	PREM sensitivity kernels	69
3.6	Sensitivity kernels for Antarctica	70
3.7	Sample FTAN diagrams	73
4.1	Map of the seismic stations in Antarctica	79
4.2	Station pairs in Antarctica	80
4.3	Cross correlation: AU.MAW G.DRV	84
4.4	Cross correlation: AU.MAW IU.SBA	84
4.5	Cross correlation: G.CCD.10 IU.QSPA	84
4.6	Cross correlation: G.DRV IU.CASY	85
4.7	Cross correlation: G.DRV IU.QSPA	85
4.8	Cross correlation: G.DRV IU.SBA	85
4.9	Cross correlation: GE.SNAA IU.CASY	86
4.10	Cross correlation: GE.SNAA IU.SBA	86
4.11	Cross correlation: IU.QSPA IU.SBA	86
4.12	Dispersion curve for AU.MAW G.DRV	88
4.13	Dispersion curve for G.DRV IU.CASY	88
4.14	Dispersion curve for G.DRV IU.QSPA	88
4.15	Dispersion curve for G.DRV IU.SBA	89
4.16	Dispersion curve for IU.QSPA IU.SBA	89
4.17	FTAN diagram with spectral notches	91
4.18	Convergence plot: G.CCD-GE.SNAA	92
4.19	Convergence plot: G.CCD-AU.MAW	93
4.20	Actual ray coverage	94
4.21	Strong yearly seasonality	96

4.22	Convergence using summer days	96
4.23	Convergence using winter days	97
5.1	Velocity measurements binning (full)	104
5.2	Velocity measurements binning (clean)	104
5.3	Cubed sphere used for the inversion	106
5.4	Raw model: rays for $T = 30$ s	109
5.5	Raw model: rays for $T = 80$ s.	110
5.6	Rayleigh waves velocity model ($T = 30$ s)	111
5.7	Rayleigh waves velocity model ($T = 80$ s)	112
5.8	Velocity measurements binning (W. Antarctica)	114
5.9	Velocity measurements binning (E. Antarctica)	114
5.10	Avg. dispersion curves for W. and E. Antarctica	115
5.11	Avg. dispersion curves for W. and E. Antarctica (slowness)	115
5.12	1D v_S profiles	116

List of Tables

1.1	Quanterra Q330HR specifications	31
1.2	TNV data QA: reference events	36
1.3	Centering of the TNV instruments	38
3.1	Ten entries of the PREM model	68
4.1	Intel Xeon E5-4607 v2 specs	76
4.2	Number of stations per year	79
4.3	Coords for the stations of figures 4.3 to 4.11	83

Abstract

The lithosphere of Antarctica reacts to both the stress variations due to the dynamics of the mantle and the variation of the glacial load due to changes in climate. These two factors, active at different spatial and temporal scales, act on the dynamics of the glacial mass, on the evolution of the continent's topography and on the seismicity of the Antarctic plate. The knowledge of these interactions is still scarce, but the need for a better comprehension of the processes that involve interactions between climate and the geosphere is increasingly clear.

The main aim of this work is to improve on the current knowledge of the three dimensional structure of the Antarctic lithosphere producing a new continental-scale tomographic model. The knowledge of spatial variations in lithospheric thickness is recognized as a necessity to build a reliable glacial isostatic adjustment model for Antarctica (Nield et al. 2018). Seismic tomography studies of Antarctica already exist but, to the best of my knowledge, they are based on earthquake data and their resolution is limited by the fact that seismic networks on the continent are very scarce and often made by temporary stations installed on the ice sheet, whose quality is not on par with that of permanent seismic stations installed on rock. There is ample room for improvement.

The classic data source for tomographic studies is a set of seismic signals produced by earthquakes. In this work I use a different technique: the information on the elastic properties of lithosphere is extracted by cross-correlating the continuous background vibrations (often referred to as "ambient seismic noise") recorded in different locations. This approach is presented in [chapter 2](#) and has some advantages with respect to more classic earthquake-based studies. The possibility to perform tomography without

earthquakes is especially valuable in Antarctica, considered its very low seismic activity. Besides, the correlation of signal recorded by a pair of stations brings information on the structure comprised between the two stations, giving then optimal sensitivity to continental structure – as opposed to paths from earthquakes, mostly on ocean ridges, that mix oceanic and continental structure. Interferometric techniques have shown unquestioned ability to map crustal structure using microseismic data, but also capacity to image mantle structure using the long-period seismic hum.

Instead of a the classic cross-correlation, this work uses the *phase cross correlation* technique, which appears to be more robust than the classic one in our use case, where input data is often not very clean. Signal phases are used even to improve the correlogram stacks, by weighting the stack samples according to the correlograms' instantaneous coherence.

I also contributed to the maintenance and development of the seismic observational infrastructure in Antarctica. This thesis then also recaps the activities I carried out during my participation to the 31st campaign of the Italian National Antarctic Research Program (PNRA), to which I participated during the PhD course. These activities did in part follow up to what was my job during the 10th winter campaign at the Concordia research station, which saw me on the ice for the entire year 2014.

The present work is organized as follows. [Chapter 1](#) is an overview of the geography, geology and seismicity of Antarctica. Within this chapter, [section 1.3](#) explains how seismic stations are installed on the continent and what are the difficulties and peculiarities of these deployments. This section also accounts for my activities on the field. [Chapter 2](#) treats ambient seismic noise in general and how useful information is extracted from it by cross-correlation and stacking. The chapter introduces the correlation and stacking techniques used in this work: the *phase cross-correlation* and the *phase weighted stack*. [Chapter 3](#) is an overview on surface waves and on how they are modelled to gather useful information to later construct a seismic tomography. [Chapter 4](#) is more technical, concentrating on the data retrieval and actual processing, and on the difficulties encountered during the analysis. Finally, [chapter 5](#) is about the inversion, with an introduction to the inverse problem, a description on the parametrization used in this

study and finally some surface wave velocity maps. [Chapter 6](#) draws some conclusions followed by two appendices with additional material.

The phase cross-correlation, and the phase-weighted stacking technique, showed clear advantages — with respect to the conventional linear cross-correlation and stack — in dealing data of heterogeneous quality, as in this case. However, the phase-weighted stack in many cases did not perform optimally, so I had to use a hybrid linear/phase-weighted stacking technique. The preliminary linear stack somehow pre-conditions the signal, letting some coherence grow so that it is then optimally exploited by the later phase weighted stage. Rayleigh-wave dispersion curves could thus be obtained (through automatic frequency-time analysis) from 20 s to 180 s, with the best-observed period interval between 30 s and 80 s. I observed some seasonality effects in several, but not all, station pairs, where winter data are faster to converge to a stable Rayleigh wave dispersion curve, than summer data. The reason for this behavior is not completely clear, but it should have to do with better conditions (more coherent ocean-generated microseismic noise, less contamination from local atmospheric-induced disturbance). Performance of observatory-grade seismic installation was obviously more reliable than capacity of temporary stations, particularly so at longer period. This was of course expected. Temporary stations, however, showed generally good performance. Field experiments can also provide very usable data.

I inverted dispersion measurements for maps of Rayleigh group velocity at different periods. Shorter-period maps carry resemblance of crustal and uppermost mantle structure. In Antarctica, the 30 s Rayleigh wave group velocity map shows lower velocities in East Antarctica, and higher velocities in West Antarctica, coherently with expectations related to a thicker cratonic crust in the East, and thinner extending crust in the West. Deeper sensitivity of longer periods make the color pattern switch for the 80 s map, sensing the upper mantle and consequently higher velocity at the cold roots of cratonic East Antarctica and lower velocity in the tectonically active West. So far, the maps I have produced rely entirely on my own measurements. A forward extension will formally include additional information resulting from previous studies, as *a priori* information in the Bayesian inverse formalism.

Acknowledgements

I would like to thank my advisor Andrea Morelli for his guidance during the last three years: I have learned a lot and I owe it mostly to him. I would also like to thank Alberto Armigliato for his feedback and support during the development of my work and the writing of this thesis: it has been of great importance.

Thanks to Martin Schimmel, Sergi Ventosa and to all the Barcelona group: the discussions we had during my stay at ICTJA have been an invaluable source of ideas and scientific insight.

Thanks to Peter Danecek and Alberto Delladio for giving me the opportunity to participate to the 31st PNRA expedition: working on the field in such a challenging environment has been an extraordinary experience I will never forget.

Chapter 1

Antarctic Seismology

1.1 General notions on Antarctica

Geography

Located in the Earth's southern hemisphere, the Antarctic continent is centered around the South Pole and largely south of the Antarctic Circle, running at about $66^{\circ}33'$ south of the Equator. It has an area of more than 14×10^6 km² and is washed by the Southern (or Antarctic) Ocean, which is the southern part of the Pacific, Atlantic, and Indian Oceans (Drewry 1983). About 98% of the continent is covered by the Antarctic ice sheet, the world's largest ice sheet. Its average thickness is of 1.6 km, peaking at 4.8 km, and it is so massive that it has depressed the continental bedrock below sea level (Fretwell et al. 2013). The coastline measures about 18×10^3 km and is characterized by the presence of ice shelves¹, floating ice and other ice formations (Drewry 1983). A general map of the continent is shown in [figure 1.1](#).

A standard gridded map of the surface elevation, ice-thickness and of the the sea floor and subglacial bed elevation of the Antarctic has been produced by the British Antarctic Survey and is known as Bedmap2 (Fretwell et al. 2013). The model incorporates over 25 million measurements from different geophysical and cartographic sources. A preview of the model is shown in [figure 1.2](#). In September 2018, the National Geospatial–Intelligence Agency (NGA) released the Reference Elevation Model of Antarctica (REMA): a

1. An *ice shelf* is a floating platform of ice that forms where a glacier or ice sheet flows down to a coastline onto the ocean surface.

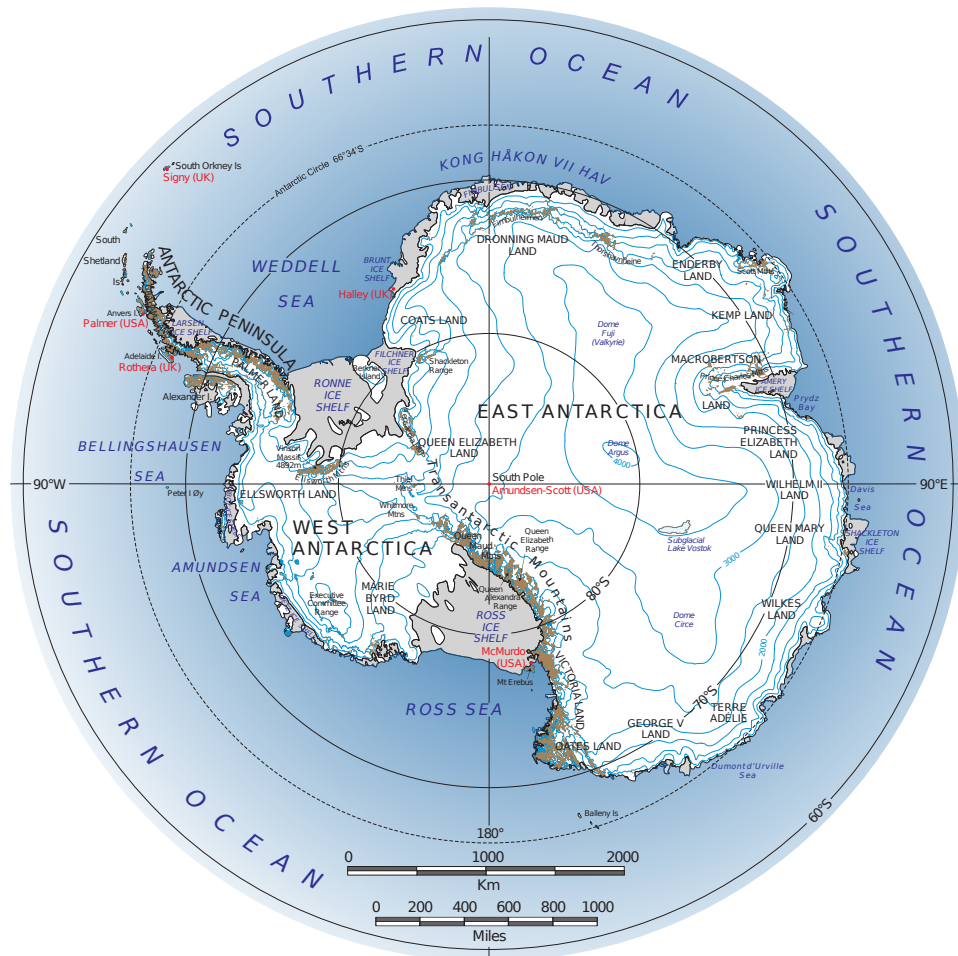


Figure 1.1 Antarctica overview map showing the main geographic features of the continent with their names (USGS 2018). Dome Circe, Dome Argus and Dome Fuji are also respectively known as Dome C, Dome A and Dome F.

high resolution (8 m) terrain map of nearly the entire continent (Howat et al. 2018).

Seven countries have the partially overlapping territorial claims on part of Antarctica shown in [figure 1.3](#): Argentina, Australia, Chile, France, New Zealand, Norway and the United Kingdom. The validity of these claims is not universally recognized (Division 2018). The United States and Russia (formerly as the Soviet Union) reserved the right to make claims in the future. The international relations with respect to Antarctica are regulated by the Antarctic Treaty. The treaty entered into force in 1961 as a peace-keeping effort and currently has been signed by 53 countries. The treaty sets aside Antarctica as a scientific reserve, establishes freedom of scientific investigation and bans military activity on the continent.

Geological structure

Antarctica is roughly divided in two by Transantarctic Mountains, a mountain range of uplifted sedimentary rock which extends across the continent from the north-easternmost peninsula in Victoria Land to Coats Land ([figure 1.1](#)). The two halves are conventionally called West Antarctica and East Antarctica and approximately correspond to the eastern and western hemispheres relative to the Greenwich meridian. East Antarctica is larger and includes both the South magnetic pole and geographic South Pole. This division is shown schematically in [figure 1.4](#).

Geologically, West Antarctica closely resembles the Andes of South America (Stonehouse 2002). The Antarctic Peninsula was formed by uplift and metamorphism of sea-bed sediments during the late Paleozoic and the early Mesozoic eras. This sediment uplift was accompanied by igneous intrusions and volcanism. The only anomalous area of West Antarctica is the Ellsworth Mountains region ([figure 1.1](#)), where the stratigraphy is more similar to the eastern part of the continent (Stonehouse 2002).

East Antarctica is geologically very old, dating from the Precambrian², with some rocks formed more than 3 billion years ago. It is composed of a metamorphic and igneous platform which is the basis of the East Antarctic

2. The earliest part of Earth's history, spanning from the formation of Earth about 4.6 billion years ago to the beginning of the Cambrian Period, about 541 million years ago.

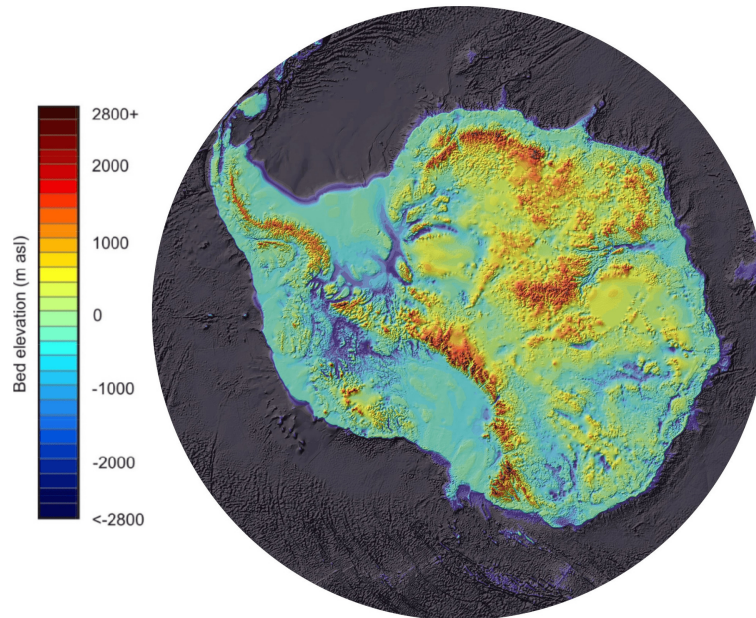


Figure 1.2 The Bedmap2 bed elevation model (Fretwell et al. 2013).

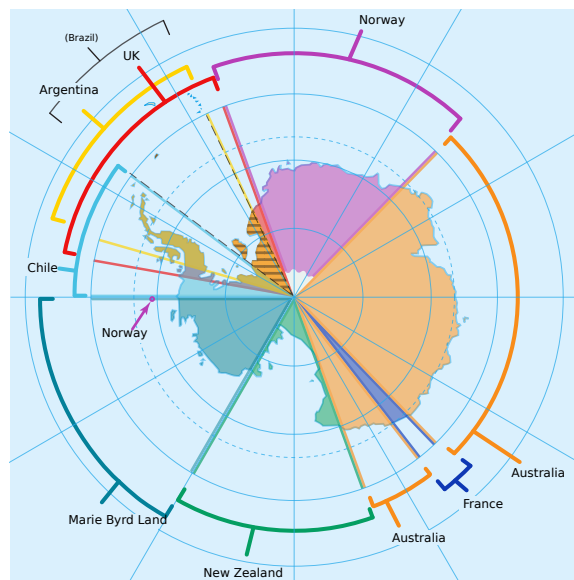


Figure 1.3 Antarctic territorial claims (Division 2018). The countries with territorial claims (Argentina, Australia, Chile, France, New Zealand, Norway and the United Kingdom) are all signatories of the Antarctic Treaty. The Marie Byrd Land territory is unclaimed.

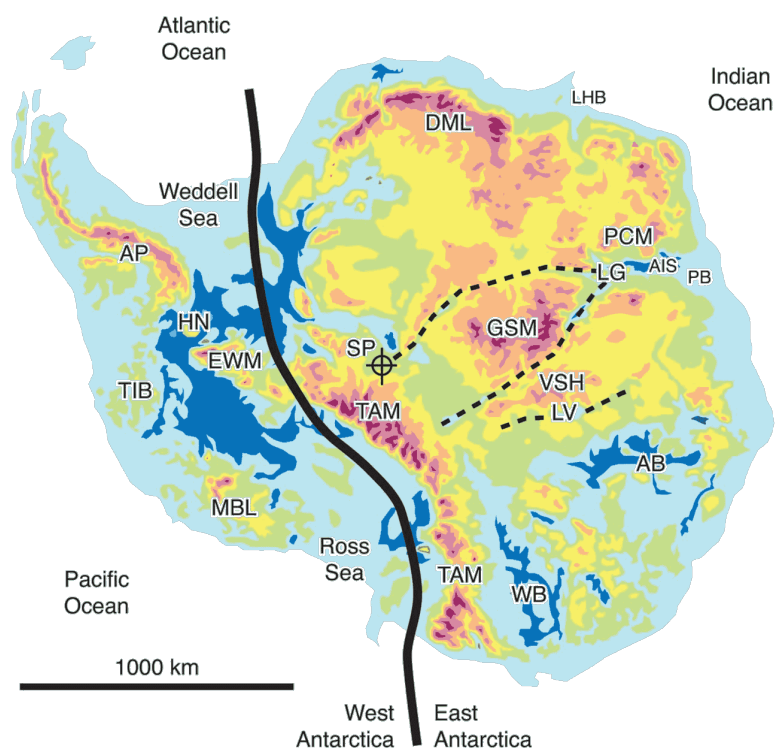


Figure 1.4 The Transantarctic Mountains range conventionally divides the continent in two halves: West Antarctica and East Antarctica (modified from Harley 2011). The two halves roughly correspond to the eastern and western hemispheres relative to the Greenwich.

Shield or Antarctic Craton: the old and stable part of the lithosphere that covers the majority of the continent (Drewry 1976).

Climate

Antarctica has the coldest climate on Earth. Temperatures reach a minimum of between -80°C and -89.2°C in the interior in winter and a maximum of between 5°C and 15°C near the coast in summer (Chapman and Walsh 2007). The coldest air temperature ever recorded on Earth was -89.2°C at the then Soviet Vostok Station (East Antarctica) in July 1983 (Turner et al. 2009). A map of the average surface temperature of Antarctica in winter and summer is shown in figure 1.6.

East Antarctica is colder than its western counterpart because of its higher elevation. Weather fronts rarely penetrate far into the continent, leaving the centre cold and dry. Antarctica is in fact a cold desert, with a snowfall equivalent to 150 mm of water each year (BAS 2018). The edge of the continent is often interested by very strong katabatic winds coming from the plateau, while in the interior wind speeds are typically moderate (Parish and Bromwich 1991).

Research facilities

As of October 2018 a total of 30 countries maintain permanent research stations in Antarctica. Some of these stations are staffed year-round, while others operate only during the austral summer (COMNAP 2018). The population of people performing and supporting scientific research on the continent and nearby islands varies from approximately 4000 during summer to 1000 during winter. Figure 1.7 shows the countries that currently maintain at least one permanent research facility in Antarctica, while figure 1.8 is a map of the permanent facilities.

Italy maintains two permanent research stations: Mario Zucchelli Station (MZS) and Concordia. The stations are run by the National Antarctic Research Program (*Programma Nazionale di Ricerche in Antartide*, PNRA) with their logistics is managed by the National Agency for New Technologies, Energy and Sustainable Economic Development (*Agenzia nazionale per le*

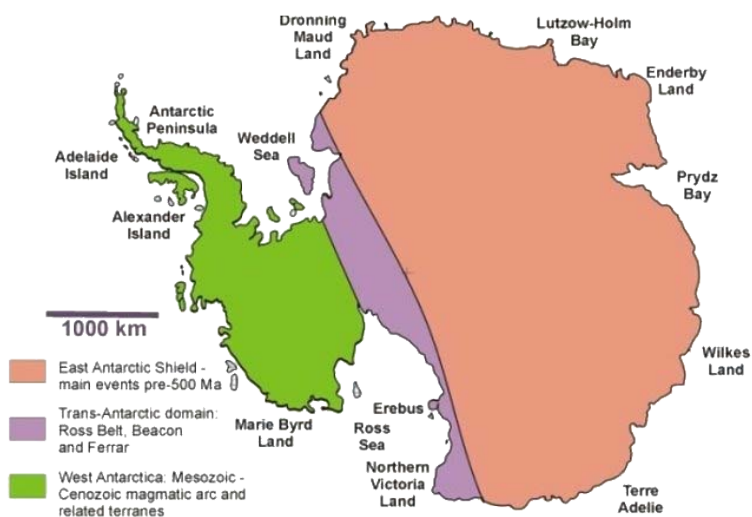


Figure 1.5 A coarse geological subdivision of Antarctica into three geological regions: the old and stable East Antarctic Shield, the generally younger West Antarctic domain, and the Trans-Antarctic domain, along the Transantarctic Mountains (modified from Harley 2011).

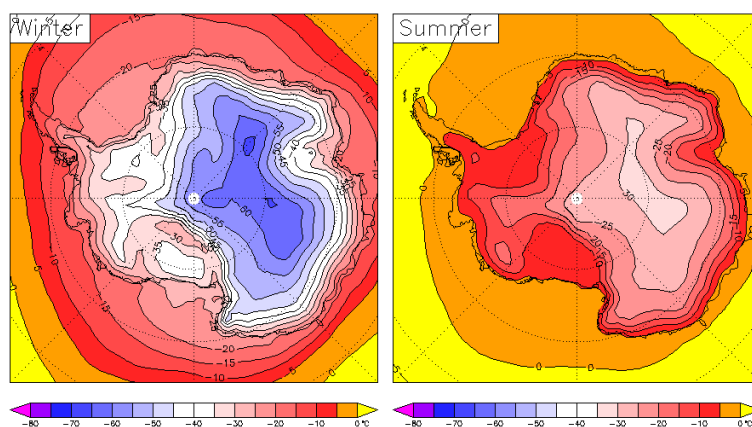


Figure 1.6 Near surface (1.5 m) temperature of Antarctica in winter and summer from European Centre for Medium-Range Weather Forecasts (ECMWF) 40 year reanalyses, for the period 1979-2001 (Credit: W. M. Connolley).



Figure 1.7 Countries that maintain at least one permanent research station in Antarctica (COMNAP 2018).

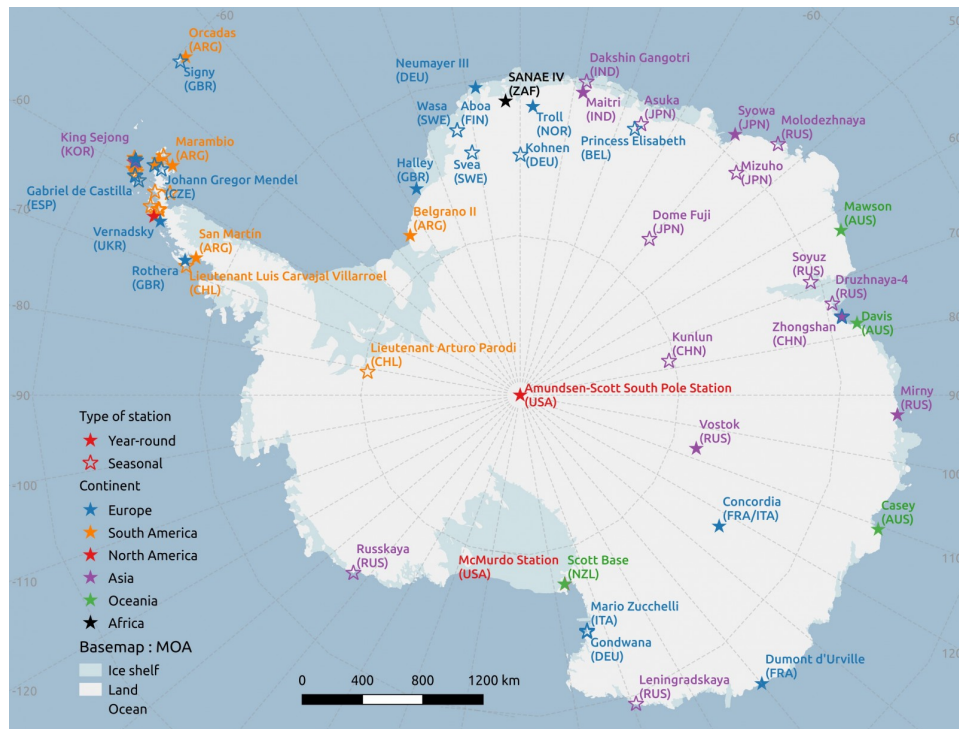


Figure 1.8 The permanent research stations in Antarctica (COMNAP 2018, credit: S. Berger).

nuove tecnologie, l'energia e lo sviluppo economico sostenibile, ENEA). Mario Zucchelli Station ([figure 1.9](#)) was created in 1985 and is located at Terra Nova Bay, at the coast of Victoria Land, and is staffed only during the austral summer, between October and February. Concordia Station ([figure 1.10](#)) is jointly operated by PNRA and the French polar institute Paul-Émile Victor (IPEV), is staffed year-round since 2005 and is located at Dome C, on the East Antarctic plateau, at 3233 m above sea level. Concordia is the third permanent, all-year research station on the Antarctic Plateau, the other two being Vostok Station (Russian, formerly Soviet), located near the geomagnetic South pole, in inland Princess Elizabeth Land, and the Amundsen–Scott South Pole Station (USA) located at the geographic South Pole.

1.2 Seismicity of the Antarctic plate

Seismic activity

The Antarctic continent has a number of unique features, one of these is its tectonic setting: its margins are almost everywhere divergent, with only a small fraction of convergent or transformed margins. One consequence of this fact is that the seismicity of the Antarctic plate is quite low when compared with other continental plates. This scarce seismic activity was largely unknown up to a few decades ago due to the lack of instrumentation deployed on the continent. It is noteworthy that the first confirmed earthquake in continental Antarctica has been recorded in 1985 (Adams, Hughes, and Zhang 1985).

A map of the seismic events occurred below 50° S between year 2000 and 2010 and with $M_W \geq 6$ is shown in [figure 1.11](#). From this figure it is immediately evident how the seismic activity is concentrated on the boundaries of the continental plate. The highest magnitudes determined for Antarctic continental intraplate earthquakes are approximately $M_W = 4.5$, with only a small minority reaching $M_W \geq 5.0$ (Reading 2007). The following outline of the seismicity of Antarctica is best read while keeping [figure 1.1](#) as a reference.

The most seismically active region in continental Antarctica is the region of the Transantarctic Mountains, which forms a belt of larger earthquakes.



Figure 1.9 Aerial view of Mario Zucchelli Station (Terra Nova Bay, along the coast of Victoria Land). The station is staffed only during the austral summer and is operative since 1985.

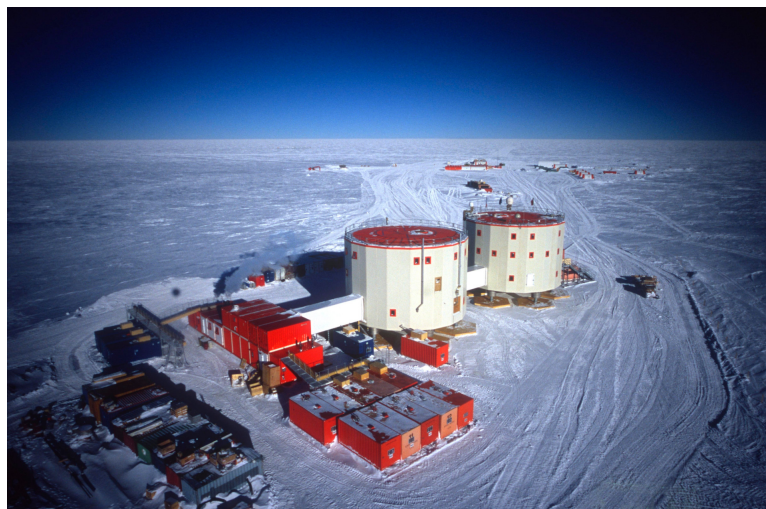


Figure 1.10 Aerial view of Concordia Station (Dome C, East Antarctic plateau). The station is staffed year-round since 2005. The picture has been taken installing a camera on a weather balloon.

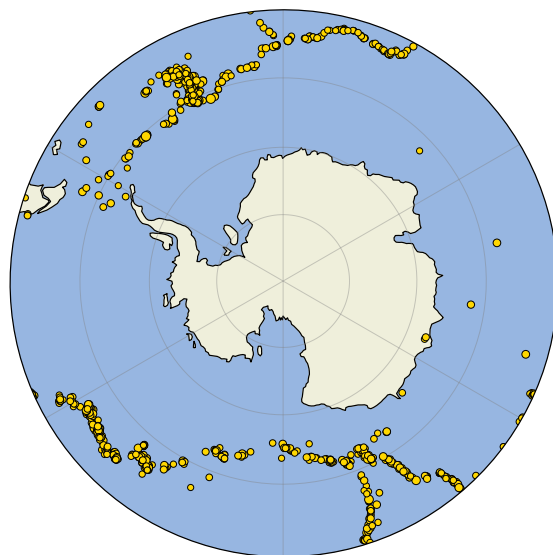


Figure 1.11 Map of $M_W \geq 6$ seismic events happened south of 50° S between 2000 and 2010 (USGS data).

Events occurring along the Ross Sea margin through Victoria Land are recorded relatively frequently and microseismicity clusters are known to be associated with the activity of some major glaciers. Isolated events occurred in the regions of Lake Vostok and Dome F, in the East Antarctic. Seismicity in the Weddell Sea has been confirmed by records from an array located near the German Neumayer station on the Dronning Maud Land coast. Recorded earthquakes in the northern part of the peninsula are associated with subduction in the Bransfield Strait (between the South Shetland Islands and the Antarctic Peninsula), while a few are located on the continental rise in the southern Pacific Bellingshausen Sea. In East Antarctica seismic events are clustered along the coast, in the region of Adélie Land. Seismic events are also observed further along the coast of Wilkes Land and offshore of Enderby Land (Kanao 2014; Reading 2007).

Away from the continental area, the intraplate region northwest of the Balleny Islands (north of Victoria Land) has a very high seismicity, as can be expected given its location close to the plate boundaries that form the junction between the Pacific, Australian, and Antarctic plates. Intraplate seismicity is also observed between the Australian–Antarctic Ridge and the Antarctic continent (Kanao 2014; Reading 2007). Scattered groups of

intraplate earthquakes occur on the Kerguelen Plateau, in the southern Indian Ocean, while the Crozet Islands and the Prince Edward Islands are very quiet (Reading 2007).

1.3 Seismography in Antarctica

Seismic stations

Antarctica represents one of the most extreme and exceptional environments on Earth. It is the most remote continent and in terms of logistics probably the most challenging region to reach, in particular when considering locations in the interior of the continent. As a consequence, the availability of scientific data is rather scarce and the density of instrumental observation points is low. This makes any geophysical observation extremely valuable. At the same time these environmental conditions and practical constraints require special approaches and operational practice.

Seismic instrumentation of Antarctica was a priority for the International Geophysical year (IGY) in 1957 (Hatherton and Evison 1962; Lander 1959). A total of twelve stations were installed, several becoming permanent in 1963 with the installation of the World Wide Standard Seismographic Network (WWSSN) (Lander 1959; Okal 1981). Even with the limited station coverage of IGY six events were located south of 65° and twenty were located south of 55° (Lander 1959). Before 1963 the earthquake detection threshold was approximately $M_W = 6$, with the improved WWSSN coverage the detection threshold dropped to approximately $M_W = 4.9$ (Okal 1981).

It is only since the late 1990s that larger scale deployments of temporary stations have become feasible with the advent of more cost efficient, high quality equipment along with increased logistical support. These deployments have typically been very localized, often only covering several hundred square kilometers. As equipment evolved array size also improved. The Transantarctic Seismic Experiment (TAMESIS, Anandakrishnan and Wiens 2000) array, operating during the austral summers of 2000–2003, crossed the Transantarctic Mountains and extended into East Antarctic. The Gamburtsev Mountains Seismic Experiment (GAMSEIS, Wiens and Nyblade 2007a), operative between 2007 and 2009 was deployed across the Gamburt-

sev Subglacial Mountains, in East Antarctica, just underneath the Dome A. The Polar Earth Observing Network (POLENET, Wiens and Nyblade 2007b), started in 2007 and still operative, has seismic stations deployed across West Antarctica. The locations of these arrays are shown in [figure 1.12](#).

The stations that are part of these temporary seismic arrays complement a smaller number of permanent, observatory grade stations. The difference between the two is on all levels, from the choice of the instruments to the installation site, which is an extremely important factor in the overall data quality. An observatory grade station is visible in [figure 1.13](#), note how the seismometers are installed on a concrete block built within a granite cave. On the contrary [figure 1.15](#) shows a temporary deployment where the instrument is merely protected by some rocks.

The Italian National Institute for Geophysics and Volcanology (INGV) maintains two permanent seismic observatories in Antarctica, installed in the premises of the Italian permanent research stations. Moreover, the institute maintains a semi-permanent station at Starr Nunatak and a number of temporary stations. The stations are part of the MedNet network (INGV 1990).

The Terra Nova Bay observatory

The Terra Nova Bay seismological observatory (station code TNV, 74.70° S 164.12° E) is based at the Mario Zucchelli Station. The first seismological experiments started shortly after the establishment of the Italian scientific station at Terra Nova Bay and led in 1988–1989 to the construction of the permanent seismological observatory, located in an artificial cave dug in granite about 2 km away from the research station and equipped with a set of Streckeisen STS-1/VBB (very broadband) seismometers. With a low frequency corner of the response located at 360 s, the STS-1 is widely regarded as one of the best instruments available for seismological research for long and very long period studies. The entrance of the cave and the instrumentation are pictured in [figure 1.13](#).

In the current setup the station has two separate and almost independent acquisition chains, one with the original Streckeisen STS-1 sensors, the other with a Streckeisen STS-2 sensor (another observatory-grade instrument, this

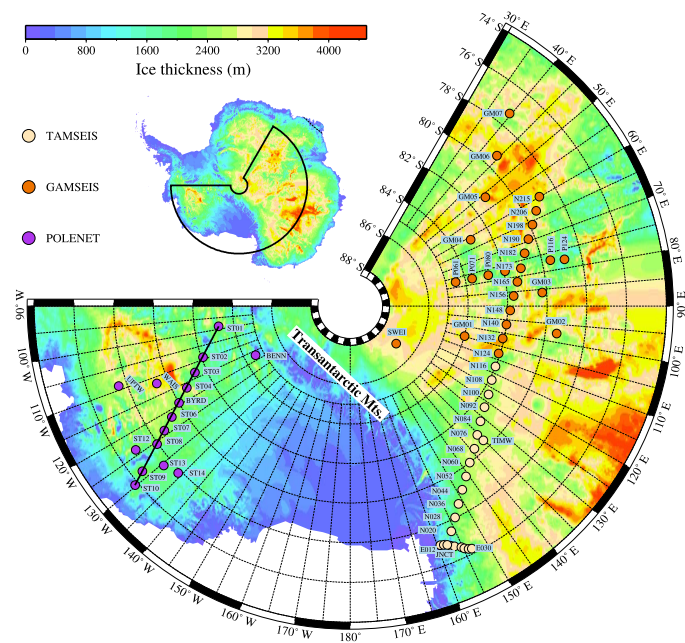


Figure 1.12 Locations of the three main seismic arrays in Antarctica: TAMSEIS, GAMSEIS, and POLENET (modified from Yan et al. 2018).

one with a low frequency corner of the response located at 120 s). Experience shown that the adverse environmental conditions and the unmanned operation during Antarctic winter requires significant level of redundancy for the acquisitions systems. The current setup features several acquisition and data storage systems both at the cave and in the base. More details will be given in section 1.4.

Regular maintenance is performed yearly along with the recovery of the recorded data. In the recent years the observatory's acquisition system has been upgraded with modern Quanterra Q330HR digitizers (table 1.1 reports the digitizer's specifications) and new rugged servers (ALPHA2000 PrioComP) at the cave.

There are plans to bring further improvements on the redundancy and the site infrastructure, in particular regarding power supply, networking and cabling. The ageing STS-1 sensors are increasingly difficult to maintain and opportunities to replace them are being explored.



Figure 1.13 The entrance of the Terra Nova Bay seismic observatory artificial cave and its instrumentation during the evacuation of the STS-1 vacuum chambers.

Main Channels	3 26 bit and 3 24 bit channels
Aux channels	4/8 DI/SE 16 bit 1 sps. Full range 50 V
Dynamic range	144 dB to 145 dB wireband rms typical
HR Channels	0.02 Hz to 20 Hz 147 dB to 158 dB
Gain	Selectable per channel: 1 to 20
Filtering	Linear or Minimum Phase FIR
Sample rates	1 sps to 200 sps
Time base	Precision TCXO, phase-locked GPS

Table 1.1 Technical specifications of the Quanterra Q330HR digitizer.

The Concordia observatory

The Concordia observatory (station code CCD, 75.11° S 123.31° E, Dome C, East Antarctic Plateau) is jointly operated by INGV and the *École et observatoire des sciences de la terre* (EOST) of Strasbourg, France. The first seismological experiments started already before the opening of the permanent base in 2001. In 2005 a permanent observatory was established in an artificial cavity constructed with shipping containers at approximately 12 m of depth. Two independent sensors and acquisition chains are currently operated at the observatory, one equipped with a Streckeisen STS-2 (figure 1.14), the other with a Nanometrics Trillium T240 sensor. The temperature in the cave is very stable at about -55°C , but the STS-2 is heated to about -30°C to keep it within its operational limits.

Both chains were recently upgraded with modern Quanterra Q330S digitizers and rugged ALPHA2000 PrioComP servers installed in the seismology shelter (hut). Moreover a real-time data transmission to France and a near-realtime data transmission to Italy were recently established. Regular maintenance and recovery of all the recorded data is performed each year.

The observatory is currently undergoing a major upgrade due to the limited lifetime of the subsurface cavity and installations. This upgrade foresees the installation of a post-hole seismic sensor in a borehole approximately 130 m deep. The seismology shelter which in the meantime has been completely covered by snow drift will be replaced by a new wooden shelter on stilt. Currently tests are being carried out with the temporary installation of a near surface Nanometrics Trillium T240 sensor and a Nanometrics Trillium T120 Posthole. During the 2018–2019 summer campaign the drilling and casing of the borehole will be carried out along with the construction of a new shelter for the instrumentation.

The Starr Nunatak station

Figure 1.15 shows the semi-permanent autonomous seismic station at Starr Nunatak³ at a distance of approximately 150 km from Mario Zucchelli station and was first installed in the framework of a temporary network in 2003. Later

3. A *nunatak* is a rocky peak not covered with snow or ice which raises within or at the boundary of a glacier, ice field or polar ice cap.



Figure 1.14 The Streckeisen STS-2 seismometer, part of one of the two acquisition chains of the Concordia seismic observatory (CCD). The sensors are installed at a depth of about 12 m, in a niche dug in snow. The ambient temperature is quite stable at about -55°C , but the sensor is heated to -30°C .

its operation continued on a semi-permanent basis and with surprisingly good reliability. This station is powered by solar panels and hibernates during Antarctic winter.

Regular visits to Starr Nunatak are performed in order to retrieve the locally recorded data and perform maintenance operations. For the future we strive to upgrade the station with modern instrumentation and to enable permanent and fully continuous operation.

1.4 Field work

During the PhD course I participated to the 31st expedition of the Italian National Antarctic Research Program (PNRA) to work on the Mario Zucchelli and Concordia seismic observatories. This section summarizes the field activities done during the campaign; more details are available in the yearly expedition reports compiled by PNRA (PNRA 2015a,b, 2016). The data retrieved during the expedition became part of the dataset that had been used in the work that follows in the next chapters.



Figure 1.15 The semi-permanent Starr Nunatak seismic station, about 150 km away from Mario Zucchelli station. Starr Nunatak marks the north side of the mouth of Harbord Glacier, on the coast of Victoria Land. The station operates on solar panels and batteries.

Activities at MZS

Some important interventions were to be done on the Terra Nova Bay observatory on this expedition. This was due the end of the service life of some instruments, and due to some malfunctions that occurred during the austral winter of 2015. Before the beginning of the expedition the state of the instruments was largely unknown, as the mentioned faults interfered with the possibility to remotely control the instruments. The planned interventions, in addition to the ordinary maintenance of the observatory, were the following:

- Replacement of a faulty Quanterra Q4120 digitizer with a newer Quanterra Q330HR;
- Installation of a new acquisition server;
- Check-up and maintenance of the backup acquisition servers,
- Retrieval of the acquired seismic data from the acquisition server installed in the seismic cave.

The seismological observatory is equipped of two independent data acquisition chain, which are not identical but equivalent. One chain begins with three single-component Streckeisen STS-1 seismometers, while the

second one has a three component STS-2. At the beginning of the campaign I found the STS-1 seismometers and their Quanterra Q4120 digitizer in good working order, but the acquisition server they were connected with had stopped working since September 2015 because of a hard drive failure. The backup acquisition servers installed at the base were functioning, but suffered from power outages during the winter. The Quanterra Q4120 digitizer of the STS-2 acquisition chain had been found faulty, so the status of the sensor could not be immediately evaluated.

I retrieved a full copy of all the available seismic data to brought back to Italy and be made available to the scientific community. I verified the consistency of this dataset against the list of known seismic events happened during the previous year reported in [table 1.2](#). As an example, [figure 1.16](#) shows the Western Indian-Antarctic Ridge earthquake happened on 1 January 2016 as recorded by the STS-1 acquisition chain.

A central part of the field activities has been the replacement of the faulty and obsolete Quanterra Q4120 with the modern Quanterra Q330HR shown in [figure 1.17](#). I removed the old instrument with its cables and sent it back to Italy. The removal of the cables has been very hard as they were completely embedded in the ice which formed over the year on the cave's walls. I then proceeded to install the Q330HR, configuring it according to the rest of the observatory's systems. In order to complete the installation it has been necessary to install a new GPS antenna on the outside of the cave, an operation for which logistical support has been needed. The GPS antenna RF cable has been installed in a UV resistant duct.

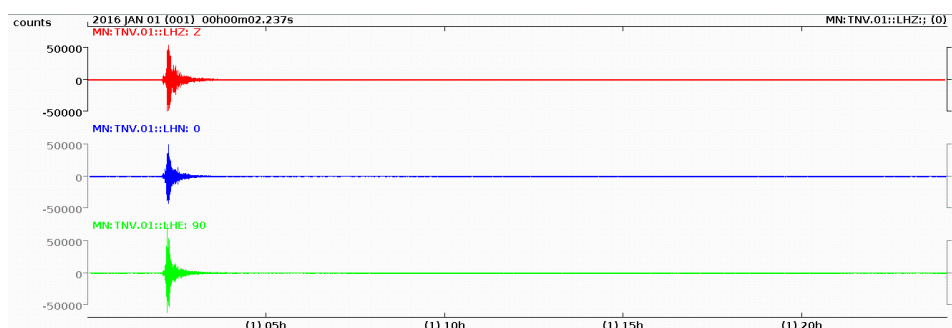


Figure 1.16 The 24-hour seismic of the STS-1 acquisition chain showing the 1 January 2016 peri-Antarctic earthquake.

UTC time	Lat	Lon	Depth	Mag	Location
2015-02-13 18:59:12	52.6487	-31.9016	16.68	7.1	Northern Mid-Atlantic Ridge
2015-02-27 13:45:05	-7.2968	122.5348	552.1	7	130 km N of Nebe, Indonesia
2015-03-29 23:48:31	-4.7294	152.5623	41	7.5	53 km SE of Kokopo (PNG)
2015-04-25 06:11:25	28.2305	84.7314	8.22	7.8	36 km E of Khudi, Nepal
2015-05-05 01:44:06	-5.4624	151.8751	55	7.5	130 km SSW of Kokopo (PNG)
2015-05-07 07:10:19	-7.2175	154.5567	10	7.1	143 km SW of Panguna (PNG)
2015-05-12 07:05:19	27.8087	86.0655	15	7.3	19 km SE of Kodari, Nepal
2015-05-30 11:23:02	27.8386	140.4931	664	7.8	189 km WNW of Chichi-shima (JP)
2015-06-17 12:51:32	-35.3639	-17.1605	10	7	Southern Mid-Atlantic Ridge
2015-07-18 02:27:33	-10.4012	165.1409	11	7	83 km WNW of Lata (SB)
2015-07-27 21:41:21	-2.6286	138.5277	48	7	228 km W of Abepura, Indonesia
2016-01-01 02:00:39	-50.5751	139.4469	10	6.3	Western Indian-Antarctic Ridge
2016-01-03 23:05:22	24.8339	93.6556	55	6.7	29 km W of Imphal, India

Table 1.2 Reference seismic events used to quickly assess the reliability of the seismic data retrieved during the 31st antarctic expedition. The coordinates are in degrees, the depths in kilometers.



Figure 1.17 The overhauled TNV acquisition system. The big orange box is an old Quanterra Q4120, on it is its replacement: a Q330HR.

The data acquisition server installed in the cave has been replaced with an ALPHA2000 PrioComP: a rugged, fanless system developed to be installed in demanding environments. The main storage of this system constituted on a 4 GiB industrial Compact Flash for the operating system and on a 32 GiB one for the data. I installed the Debian GNU/Linux 8.2 operating system and the SeisComP acquisition software, configured to acquire data from both the acquisition chains. The server is powered by the 12 V battery pack that powers the rest of the instrumentation, it is therefore protected from temporary issues with the diesel generators. On the server I wrote and installed a script to send the data to Italy using the Hermes system (detailed later) on a daily basis. This script takes into account the possibility of power or connectivity outages.

The backup servers installed within Mario Zucchelli station acquire and store data from both the acquisition chains. These server also offer a web interface that allows to locally view the acquired seismic data almost in real time. The acquisition is therefore done in parallel by three servers: one directly installed in the seismic cave and two installed at the station. In this configuration the possibility of experiencing a significant data loss is extremely remove.

While installing the new instrumentation in the seismic cave it became apparent that the flooded lead-acid backup batteries were not holding a charge anymore. I disposed of and replaced them; backup power is now provided by three 85 Ah Sonnenschein gel lead-acid batteries connected in parallel. The UPS installed in the cave and powering the Ethernet switch and the HDSL modem has been replaced with a better 1500 VA APC SmartUPS connected to an external battery pack.

After installing the new Quanterra Q330HR digitizer and the new acquisition server I verified the centering of the seismometers and the status of the vacuum chambers the STS-1s are installed in to prevent noise from convection in the surrounding air. The mass offsets were found in the expected value range, considered that the previous centering had been done on year before. From this point of view, the sensors were found in perfect working order. There were no problems in centering the masses, the results of the operation is summarized in [table 1.3](#). The pressure in the vacuum chambers

the STS-1 sensors are installed in was found very good for the North and East components (86 mbar and 158 mbar respectively), while not as good for the vertical component, at 837 mbar. After evacuating the vacuum chambers (figure 1.13) the pressure for all the three components was less than 100 mbar.

At the end of the expedition, the seismic observatory acquires, saves and automatically sends to Italy the seismic data acquired by the two acquisition chains in a stable and reliable way. The diagrams of the new data acquisition setup (figure 1.18) and power system (figure 1.18) were submitted as part of the campaign's annual report (PNRA 2016).

Activities at Concordia

The campaign at Concordia has been relatively short (less than 10 days), as the planned activities were mostly ordinary:

- Prepare a complete report of the working status of the instrumentation of the CCD observatory and of the INGV acquisition servers;
- Retrieve the seismic data of the previous year;
- Check the quality of the recorded data of the past year, verifying the absence of gaps or other kind of disturbances;
- Write and install a script that automatically sends the daily data to Italy using the Hermes system;
- Compile a general inventory.

Sensor	Offset	1st centering	2nd centering
STS-1 Z	3.6 V	0.1 V	< 0.1 V
STS-1 N	0.1 V		
STS-1 E	0.1 V		
STS-2 Z	1.9 V	0.5 V	0.6 V
STS-2 N	2.5 V	0.2 V	0.4 V
STS-2 E	1.8 V	0.7 V	0.8 V

Table 1.3 Centering parameters of the instruments of the Terra Nova Bay seismic observatory.

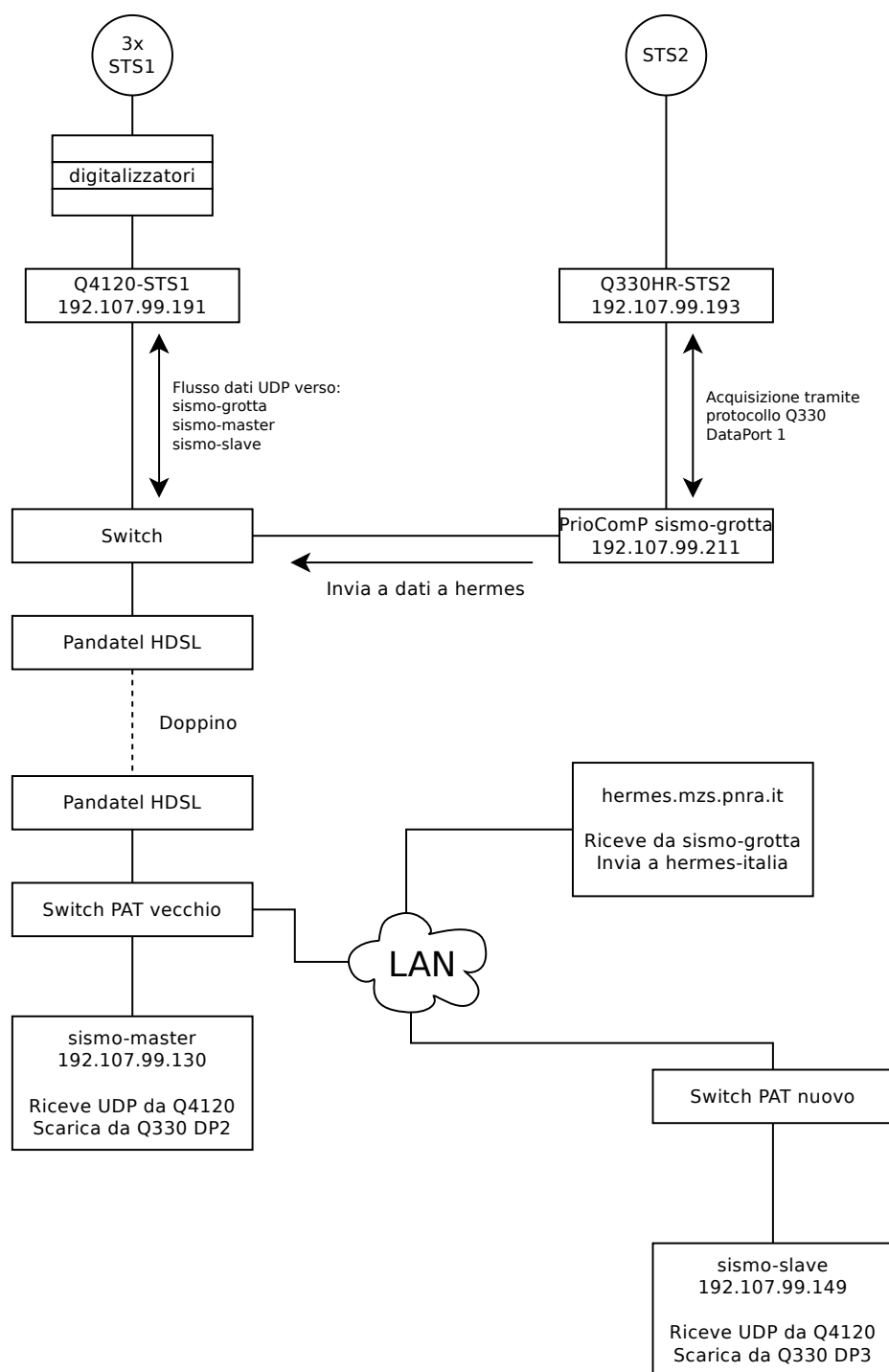


Figure 1.18 Diagram of the two data acquisition chains of the TNV seismic observatory after the 31st PNRA expedition as attached to the expedition report.

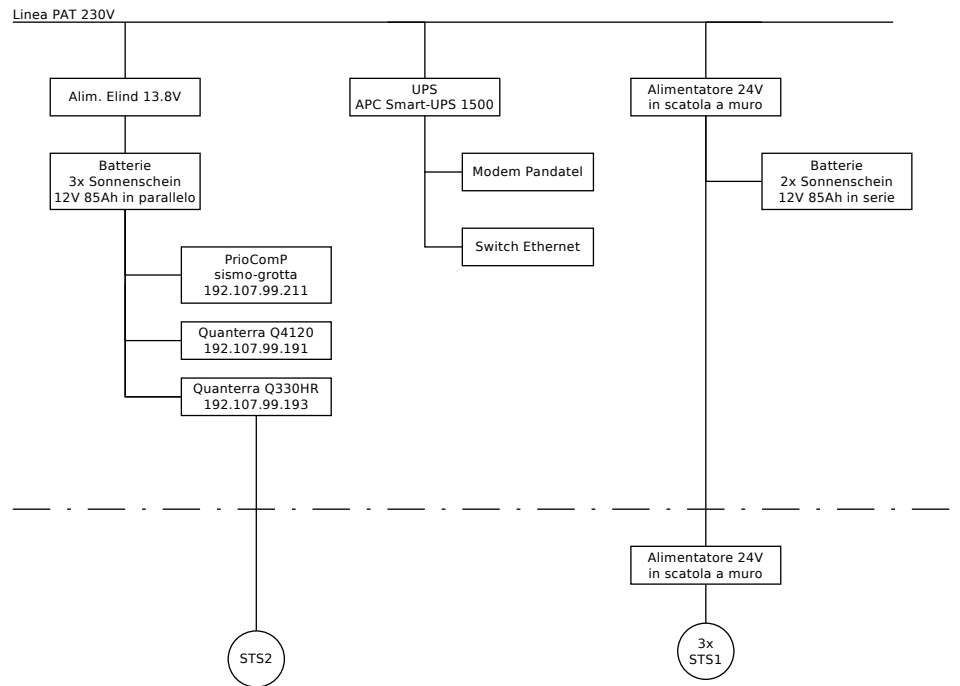


Figure 1.19 Diagram of the redundant power system of the TNV seismic observatory after the 31st PNRA expedition as attached to the expedition report.

Once at Concordia, it became immediately apparent that the replacement of a Quanterra Q4120 digitizer with a newer Quanterra Q330S happened in the last days of the previous year's summer campaign interfered with one of the two branches of the acquisition system.

After studying the new setup I set up a new acquisition server, configured it to acquire data from the new digitizer and installed it in the shelter, connecting it to the local battery backed-up power line. This acquisition server is analogous to the one installed at Terra Nova Bay. It relies on a 30 GiB compact flash for both the operating system (Debian GNU/Linux 7) and the data storage. This computer also sends the daily data to Italy using the Hermes system and sends a daily email report about the data transfer. The Hermes script cleanly handles failed transfers due to power or network problems.

After the replacement of the Q4120 with a Q330S the configuration of the two INGV backup servers already present at Concordia did not correspond to the upgraded instrumentation installed at the observatory. Moreover,

these servers suffered from some hardware issues during the 2015 austral winter. I managed to fix one server using spare parts taken from the other. This server was reconfigured to acquire and store the data and host a website that graphically shows the seismic signal to the local Intranet almost in real time. This server is now installed in Concordia's quiet building.

The data acquired during 2015 have been saved in double copy, quality checked against a list of known seismic events and brought to Italy.

During all these operations I trained the overwintering electronics technician for science of the 12th winter campaign on the activities to carry on during the winter in order to keep all the systems up and running.

The status before leaving Concordia is the following: the data is correctly acquired, saved locally and regularly sent to Italy in an automatic way. Up to this point, there was no need for any manual intervention, and all the systems appear stable and reliable.

The Hermes data transfer system

Hermes (High Efficiency Relay of Mission Experiments data Sharing) is a system to transfer scientific data from the Antarctic stations to Italy which I developed during the 10th PNRA winter campaign in Concordia and the 31 PNRA summer campaign. This section summarizes the way it operates, more information is available in the annual expeditions reports (PNRA 2015a, 2016).

Hermes has been developed from the need to transfer scientific data from Concordia to Europe and to make them available to the interested parties. An ad-hoc system is necessary as the bandwidth available to the Antarctic stations is heavily limited: in the case of Concordia a VSAT⁴ link provides a 512 Kbit/s connection to the Internet. The satellite link is not stable and suffers from a very high latency (from hundreds of milliseconds to several seconds, when the link is congested). An effort towards the implementation of a scientific data transfer system had already been done by the electronic technician for science of the 9th winter campaign in Concordia, A. Litterio, but his implementation relied on very different tools from the ones I've used.

4. A very small aperture terminal (VSAT) is a two-way satellite ground station with a dish antenna that is smaller than 3.8 m.

However, I kept the name he chose for the system: *Hermes*.

The basic idea behind the system is to centralize the data transfers, installing a pair of servers: one in Italy and one in the Antarctic base. Hermes transfers the data from the server in Antarctica to the one in Italy in an automatic and reliable way, minimizing the bandwidth usage. Because of the bandwidth constraints the system has been developed to:

1. Resume the interrupted data transfers, in order not to waste bandwidth because of the (relatively frequent.) connectivity outages;
2. Avoid to transfer the same data more than once, regardless of what the users of the system do;
3. Compress the data to transfer as much as possible, without relying on the the users doing so.

These needs and the general logistical limitations brought to some technical choices:

- Use standard tools available in any GNU/Linux distribution in order make it possible to use the system regardless of the particular distribution in use;
- Avoid polling for new data, and start the transfer as soon as some new data is available;
- Use a public key authentication system to authorize the data transfers.

In practice, Hermes is a set of interacting scripts leveraging `cron`, `inotify`, `rsync`, `ssh` and `sftp`. [Figure 1.20](#) schematically shows how the system operates, the full documentation on the system is part of the reports I produced after the expeditions and is available in [appendix A](#) (in Italian). The documentation cover also the topics of the accounting and time-dependent traffic shaping.

Data consolidation effort

The Terra Nova Bay seismic observatory (TNV), being operative since the 1988–1989 antarctic summer, is one of the longest-running observatories of

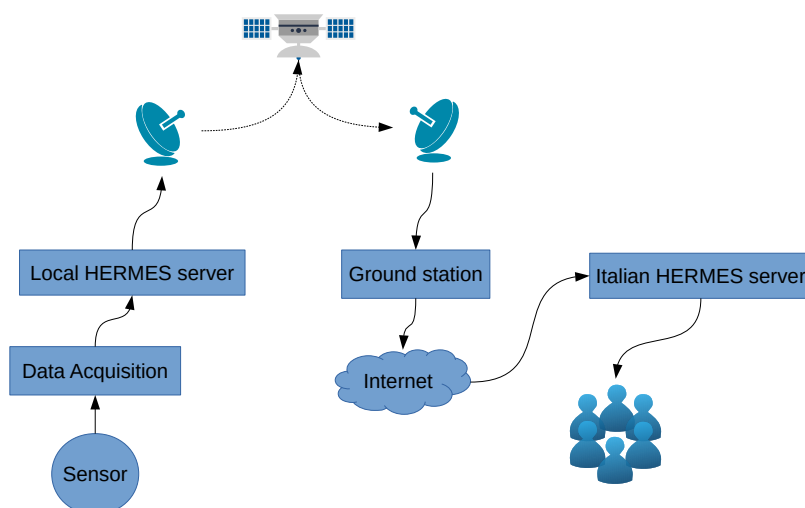


Figure 1.20 Schematic diagram of the Hermes system. When new data is transferred to the local Hermes server the data transfer to the Italian Hermes server is initiated. The peculiarity of the system is the resilience to outages, the tolerance to very high latencies, the transparent compression and the avoidance of duplicate data transfers.

the continent. The site and instrumentation are excellent and it has a long record of yearly maintenance operation, with relatively few gaps in the data.

After a careful reprocessing, cleanup and consolidation work I have done in collaboration with Dr. P. Danecek of INGV Rome, the data from TNV will soon be available in the International Federation of Digital Seismograph Networks (FDSN). This progress was brought to the 36th General Assembly of the European Seismological Commission:

P. Danecek, A. Delladio, D. Zigone, A. Cavaliere, **P. Legovini**, and D. Sorrentino (2018). Seismological Observatories in Antarctica: An Update on the Italian Program and the Evolution of the Observatories. Poster. Presented 36th General Assembly of the European Seismological Commission (ESC2018), Malta (MT).

Chapter 2

Noise interferometry

2.1 Seismic noise

Definition

In the absence of earthquakes, seismometers record a wide range of signals generated from both natural and anthropogenic sources as well as from the instruments themselves. As these signals interfere with our ability to record earthquakes, which historically generated the only signal of interest to seismologists, they have been grouped together and given the term *noise*. This situation is schematically shown in [figure 2.1](#). Noise can be divided into three broad categories:

- (i) self-noise of seismic instruments;
- (ii) non-seismic noise sources;
- (iii) non-earthquake sources of seismic energy.

The self-noise of the seismometer and digitizer (i) arises from their electronics and from thermally induced motions on the seismometer's mass. Self-noise often increases drastically at lower frequencies. Non-seismic noise sources (ii) arise because seismic instruments are sensitive to environmental conditions such as thermal variations, magnetic fields, and changes in the atmospheric pressure. Finally, non-earthquake sources of seismic energy (iii) arise from a multitude of naturally occurring surface processes as well as human activities. In this latest meaning the word *noise* is partially a historical

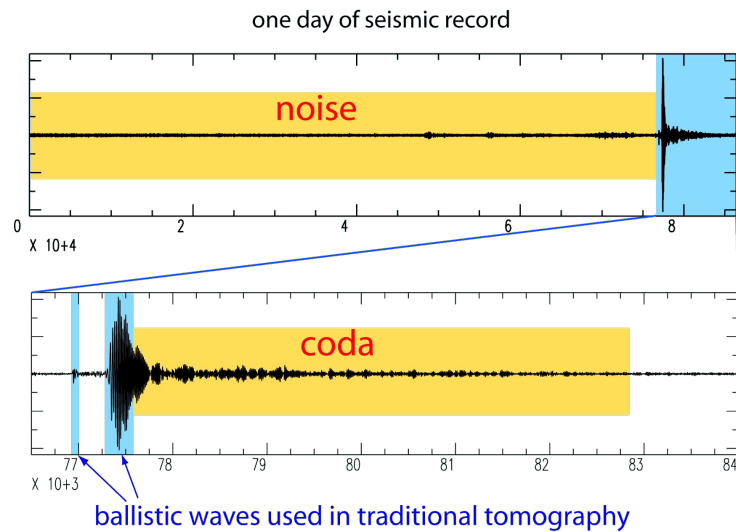


Figure 2.1 One day of seismic record showing the source-dependent, directive waves from an earthquake (also called *ballistic waves*) and seismic noise before and after the event.

misnomer: while seismologists were not very interested in this kind of signal and did normally try to get rid of it, it still is a physical signal to all effects. A more precise name could be “microseismic signal”, however in what follows we will refer to this signal as “ambient seismic noise”, “ambient wavefield” or simply as “seismic noise.”

In recent years it has emerged that ambient seismic noise is far from useless: it has been demonstrated theoretically and in practice that by applying the signal processing techniques described in this chapter to pairs of ambient noise records made at the Earth’s surface, useful information about the seismic properties of the subsurface can be obtained: this process is known as *seismic noise interferometry* (Shapiro 2005; Shapiro and Campillo 2004; Weaver 2005).

Sources of ambient seismic noise

Ambient seismic noise consists mostly of surface waves and is due to a number of causes. Higher frequency seismic noise (above 1 Hz) is mainly anthropogenic, originating from activities like road traffic and industrial work. Vibrations at around 1 Hz originate from the interaction between the solid earth and the atmosphere, and are mainly due to wind and other

atmospheric phenomena. Lower frequency noise (below 1 Hz) come from the interaction between the solid earth and the hydrosphere, and in particular from the ocean waves (Bonnetoy-Claudet, Cotton, and Bard 2006).

The longer-period end of the noise spectrum shows different features. At about $T = 14$ s we have the *primary microseismic peak*, while at about $T = 7$ s we have the *secondary microseismic peak*. The energetic peak located beyond $T = 30$ s is referred as *seismic hum*. A spectral plot displaying this subdivision is shown in figure 2.2. The distinction between the primary peak and secondary peak is due to the different noise generation mechanism (Stehly, Campillo, and Shapiro 2006).

2.2 From noise to the Green's function

Green's functions

In mathematics, a *Green's function* $G(t)$ is the impulse response of an inhomogeneous linear differential equation defined on a domain with specified initial conditions or boundary conditions. From the physical point of view, the Green's function $G(x, s, t)$ gives the displacement of a point x due to an impulsive force $\delta(t)$ located in s (Bayin 2018).

Over the time scales of seismic wave propagation we can consider Earth as a *linear* and *invariant* system: it is linearly elastic and its physical properties (density and elastic moduli) are constant. For this reason the response of the system to a linear superposition of pulses $a\delta(t) + b\delta(t - t')$ is $aG(t) + bG(t - t')$. An arbitrary force $f(t)$ can always be expressed as a superposition of impulses:

$$f(t) = \int f(t')\delta(t - t') dt' = [f * \delta](t)$$

where the asterisk is the convolution operator. It is then clear that the Green function contains the information on the response of the system to an arbitrary force $f(t)$. This response is given by:

$$\int f(t')G(t - t') dt' = [f * G](t).$$

When the system under analysis is an elastic medium, the Green's function contains all the information needed to describe how waves propagate in the

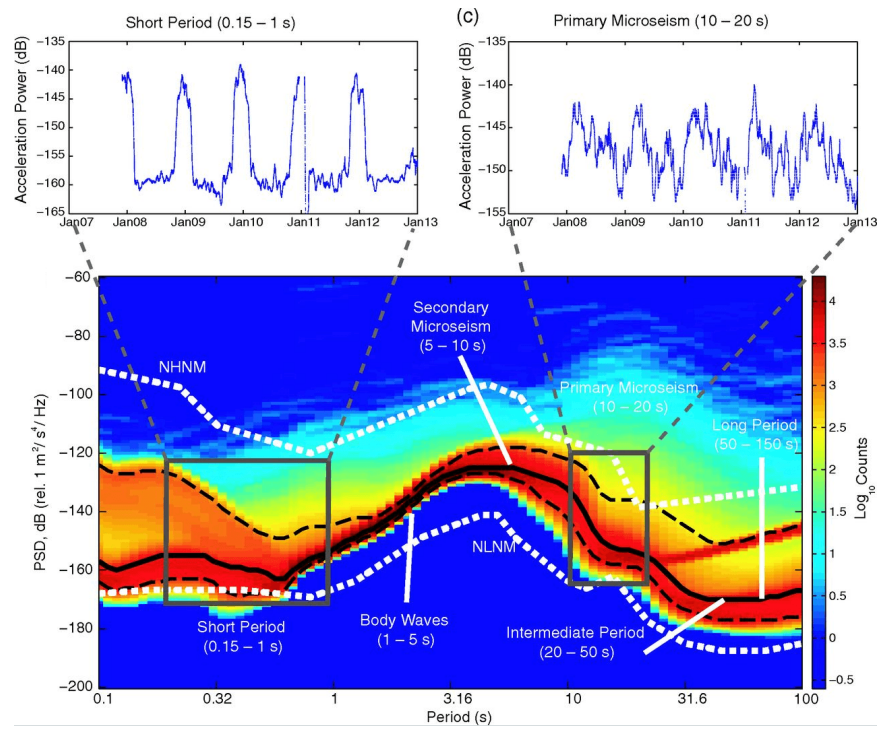


Figure 2.2 Probability density function of power spectral density (PSD) for the vertical-component of South Pole station QSPA (146 m borehole) for December 2007 to December 2012 plotted on a logarithmic scale (modified from Anthony et al. 2014).

system (Bayin 2018).

In seismology, the Green's function between a pair of locations describes the seismic energy which would result at one if there was an impulsive seismic source at the other. In other words, the Green's function describes the effect of the medium between the two locations on an impulsive source, and contains traveltime and waveform information about all the seismic phases that pass between the two locations (Stein and Wysession 2003). The Green's function can be thought as the seismogram which would be recorded at some location in response to a source at another.

Cross-correlation

In signal processing, the *cross-correlation* is a measure of similarity of two time series as a function of the displacement of one relative to the other. Its most common application is searching for a known feature in a much longer signal. For continuous, real-valued functions $f(t)$ and $g(t)$, the cross-correlation is defined as:

$$C_{fg}(\tau) = [f \star g](\tau) = \int_{-\infty}^{+\infty} f(t)g(t + \tau) dt, \quad (2.1)$$

where τ is the displacement (or *lag time*) between the functions. In the case of two real-valued discrete signals the cross-correlation is defined as:

$$C_{fg}(\tau) = (f \star g)(n) = \sum_{t=-\infty}^{+\infty} f(t) g(t + \tau) \quad (2.2)$$

where f, g are two time-series (signals) and τ is the lag time.

When f and g are similar signals the cross-correlation function is peaked at lag times for which the signals are best aligned. A cross-correlation of a signal with itself (autocorrelation) therefore has its maximum for a time lag of zero. Signals without similarities will produce a cross-correlation function that has a small amplitude for any lag time because the integrated product averages to zero.

In seismology it is useful to think the cross-correlation as a way to highlight the traveltime of seismic waves. A wavefield which has travelled between two stations will cause a similar signal to be recorded at each, shifted in time: the cross-correlation function of the records will therefore contain

a peak at a time lag which corresponds to the traveltime of the wavefield between the two stations.

Equations (2.1) and (2.2) are general mathematical definitions, but in practical applications the signals are defined over a finite time interval T and it is often useful to work with normalized correlation values. We can then define the *geometrically normalized cross-correlation* (CCGN) of two seismic signals as

$$C_{\text{ccgn}}(\tau) = \frac{\sum_{t=t_0}^{t_0+T} f(t)g(t+\tau)}{\sqrt{\sum_{t=t_0}^{t_0+T} f^2(t) \sum_{t=t_0}^{t_0+T} g^2(t+\tau)}} \quad (2.3)$$

where the symbols have the same meaning as in equation (2.2). The denominator of equation (2.3) is the geometrical mean of the energy within the time window T and normalizes the cross-correlation: we have $|C_{\text{ccgn}}| \leq 1$, with $C_{\text{ccgn}} = 1$ in the case of perfect correlation and $C_{\text{ccgn}} = -1$ in the case of perfect anticorrelation.

Noise cross-correlation

There is an important theoretical result that binds the cross-correlations of seismic noise and the Green's functions. If the noise field is *diffuse* (isotropically distributed) and *equipartitioned* (all the oscillation modes are equally excited), then the cross-correlation of such a noise field recorded at the locations A and B is related to the Green's functions G_{AB} and G_{BA} between the two points as follows

$$\frac{dC_{AB}}{dt} = -G_{AB}(t) + G_{BA}(-t). \quad (2.4)$$

and schematically shown in figure 2.4. In an ideal situation G_{AB} and G_{BA} are symmetrical because of the symmetry of the system, although in practice, when the noise distribution is not perfectly homogeneous, they may slightly differ. The negative and positive time lags correspond to noise signals traveling from B to A and A to B , respectively. The usefulness of this result has been first demonstrated by Lobkis and Weaver (2001) in the field of high frequency acoustic waves, already envisioning the applications in seismology, while Wapenaar (2004) first showed the retrieval of the Green's

function of an arbitrary inhomogeneous medium by cross correlation.

Cross-correlation is performed for positive and negative time lags, so the cross-correlation functions have both positive (*causal*) and negative (*acausal*) components (figure 2.5). Seismic noise arrives from all directions, and the noise records which are cross-correlated therefore contain energy which has travelled in both directions along an interstation path. The Green's functions calculated from equation (2.4) will therefore contain energy in both the causal and acausal parts, symmetric about zero time lag: the causal part representing energy arriving at station *B* in response to an impulsive source at station *A*, and the acausal part energy arriving at station *A* in response to a source at station *B*. Because the Green's functions are the same in both directions along a path, the two sides of the noise cross-correlation function can be treated as representing the same information. In reality a noise cross-correlation function will be perfectly symmetrical only if noise arrives from both sides of the interstation path with equal strength, which is rarely the case in practice.

In order to retrieve the complete Green's functions, which contain the whole suite of seismic waves caused by an impulsive seismic source, the required random sources must be equally distributed in the subsurface (Wapenaar 2004). As we said, this ideal condition is not verified in practice, but it has been shown (Shapiro 2005) that even in the non-ideal case the Green's functions can be at least partially reconstructed using seismic noise interferometry with the same accuracy of "traditional" earthquake observations.

Correlogram stacks

The correlation is normally done by dividing the data in time windows; the correlation is then computed on individual window pairs, and the correlograms are then stacked (summed), so their coherent part is amplified, while the incoherent part averages to zero. This classic workflow is shown schematically in figure 2.6, while a stack of cross-correlation obtained from a pair of stations in Antarctica is shown in figure 2.7. It is important to underline that in this study we are interested in the arrival times of the different phases of the seismograms, disregarding their amplitudes. For this reason there are no

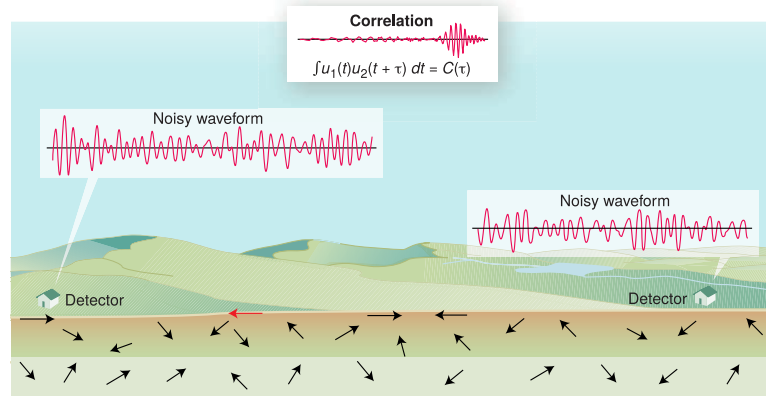


Figure 2.3 Representation of a diffuse noise field (modified from Weaver 2005). The two detectors normally record a random signal, waves that pass through both the detectors (like the red arrow) constitute a component of the two signals that is coherent and can be detected by cross-correlating them.

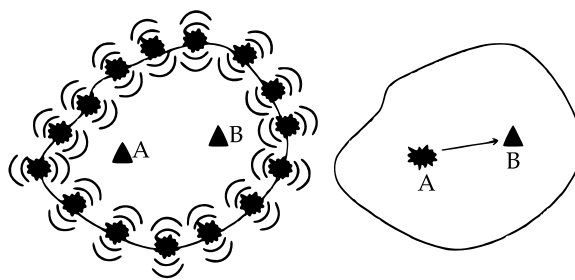


Figure 2.4 Schematic view of the principle of the seismic interferometry method. In the case of a diffuse noise field (left), the cross correlation of the signal recorded at A and B allows to derive the Green's function between the two locations (right).

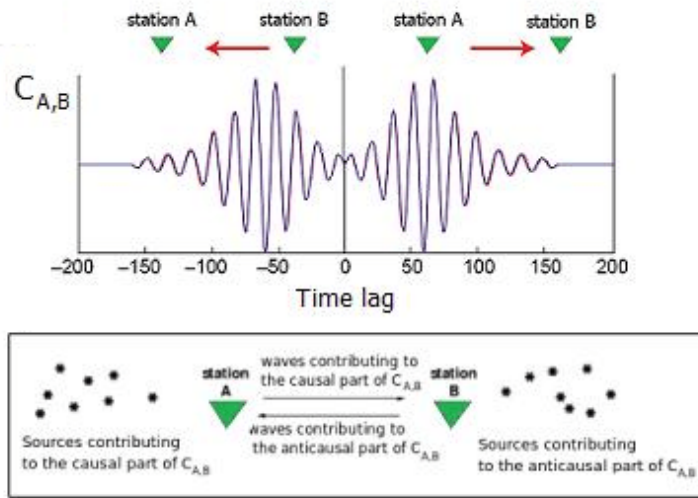


Figure 2.5 Causal and acausal parts of a noise cross-correlation function. Top: idealized noise cross-correlation function for a wavefield propagating from station *A* to station *B*. The arrows indicate the energy path which is represented by the positive and negative parts of the cross-correlation function. Bottom: representation of the noise sources which contribute to the causal and acausal components of the cross-correlation function.

problems in altering the amplitudes by stacking signals (even non-linearly, as we shall see) or normalizing. The only important thing is to keep the amplitude within the stability limits of the numerical tools.

Applications in seismic tomography

Seismic tomography has been developed on data coming from seismic events (earthquakes). The usage of earthquake data allows for an excellent tomographic analysis, as seismic waves from earthquakes are very energetic and hence it is relatively easy to detect them and extract the high amount of information they contain. At the same time the exact location of earthquake is often not perfectly determined: localizing the hypocenter of the event is not trivial, the localization depends in part on the chosen 3D model, and faults are not point-sources but are extended. Moreover, there is a number of different seismogenic mechanisms. All these effects contribute to diminish the imaging power of the tomographies computed using earthquake data.

On the other side, seismic noise is present always and everywhere. Any

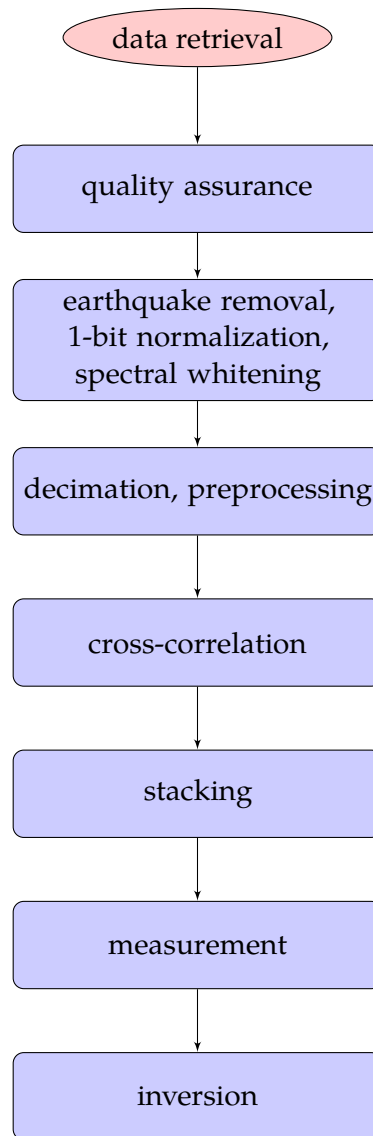


Figure 2.6 The stages of a simple seismic interferometry workflow based on the classic correlation and stacking techniques.

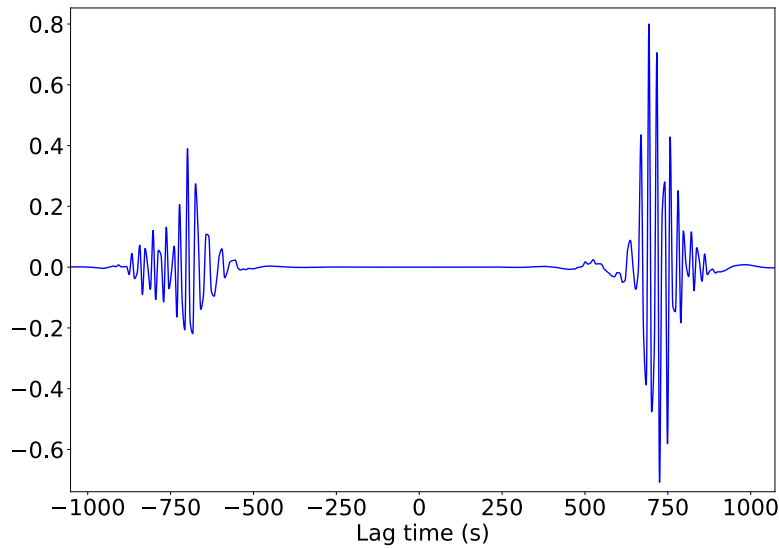


Figure 2.7 A stack of cross-correlations for a pair of stations in Antarctica. The quantity in abscissa is a stack (sum) of cross-correlation coefficients. Note that the function is not perfectly symmetrical, as it was in the ideal case of [figure 2.5](#). This is because in reality the noise field is not perfectly homogeneous.

station in any point of the planet can record it, so the data availability is virtually infinite. This is especially important in areas characterized by a low seismic activity, like the Antarctic continent.

The noise cross-correlation technique had a great impact in the scientific production of the last ten years, with several important published results, among the others: Lu et al. (2018), Nishida, Montagner, and Kawakatsu (2009), Poli, H. A. Pedersen, and and (2011), Ritzwoller, Lin, and Shen (2011), Shapiro (2005), Yao, Beghein, and Hilst (2008), and Yao, Hilst, and Hoop (2006). More specifically about Antarctica a relevant work is An et al. (2015), where a continental scale tomography is computed using classical noise cross-correlation data complemented with earthquake data.

2.3 The phase cross-correlation

Definition

The *phase cross-correlation* (PCC) is a coherence measure akin to the cross-correlation as defined in [section 2.2](#), but while [equation \(2.2\)](#) is based on the signals' amplitude, the PCC is based on the similarity of their instantaneous

phases. The PCC has been developed to evaluate the goodness of waveform fit between two time series as function of lag time by Schimmel (1999) and later used for interferometric studies, for example by Schimmel, Stutzmann, and Gallart (2011).

The basic idea of the phase cross-correlation is to use the phase of a complex function as the correlation variable instead of its amplitude. The signals we are interested in are real time-series, so to introduce the concept of phase we need to bring them in the complex domain. This is done by constructing their *analytic representation*. Given a real-valued signal $s(t)$, its analytic representation $S(t)$ is a complex signal which has $s(t)$ as its real part and the Hilbert transform of $s(t)$ as its imaginary part:

$$S(t) = s(t) + i\mathcal{H}[s(t)].$$

$S(t)$ is an *analytic signal*, that is: a complex-valued function that has no negative frequency components. As any complex function $S(t)$ can always be written in exponential form

$$S(t) = A(t)e^{i\phi(t)} \quad (2.5)$$

where $A(t)$ is called the *envelope* of $S(t)$ and $\phi(t)$ its *instantaneous phase*, which will be our correlation variable (Schimmel 1999).

Given two signals of length T with instantaneous phases $\phi(t)$ and $\psi(t)$, their phase cross-correlation is defined as (Schimmel 1999):

$$C_{\text{pcc}}(\tau) = \frac{1}{2T} \sum_{t=t_0}^{t_0+T} [|e^{i\phi(t)} + e^{i\psi(t+\tau)}| - |e^{i\phi(t)} - e^{i\psi(t+\tau)}|]$$

which is a coherence measure with the same normalization properties of equation (2.3).

Comparison with the classic correlation

One important difference between the classic cross-correlation and the phase cross-correlation consists in the fact that the classic cross-correlation favors the similarity between high amplitude features in the signals, while the

phase cross-correlation favors their overall similarity. This means that the classic approach may be a better choice when correlating energetic signals, while the phase cross-correlation works better with weaker ones, as is the case with noise. This difference is schematized in [figure 2.8](#).

Another advantage of the lack of sensibility to high-amplitude features of the phase cross-correlation consists in the fact that, when correlating noise, we don't have to deal with earthquakes, for example by removing them, performing a 1-bit normalization or spectral whitening. The signal can be processed as-is, making the workflow more simple, fast and robust.

It has to be noted that neither method is universally better: there are cases where the amplitude bias of the classic cross-correlation is desired, for example when using it to detect earthquakes in recorded data: in this case classical method is normally to be preferred. When dealing with seismic noise, where high amplitude events are normally not part of the ambient wavefield, the phase cross-correlation has been proven to be a superior method (Schimmel, Stutzmann, and Gallart 2011).

2.4 The phase-weighted stack

Definition

The idea of phase coherence can also be applied to improve the stacking stage of a seismic interferometry workflow like the one in [figure 2.6](#). While linearly stacking (that is, summing) the correlogram is the simplest approach, the technique can be improved by stacking non-linearly, giving more weight to coherent samples and less weight to the incoherent ones. This *phase-weighted stack* (PWS) has been developed by Schimmel and Paulssen (1997) and shown to bring excellent results in the field of noise interferometry Schimmel, Stutzmann, and Gallart (2011).

The phase-weighted stack weights each sample of a linear stack by a coherence measure, the *phase stack* (Schimmel and Paulssen 1997):

$$C_{pc} = \left| \frac{1}{N} \sum_{j=1}^N e^{i\phi_j(t)} \right|^v \quad (2.6)$$

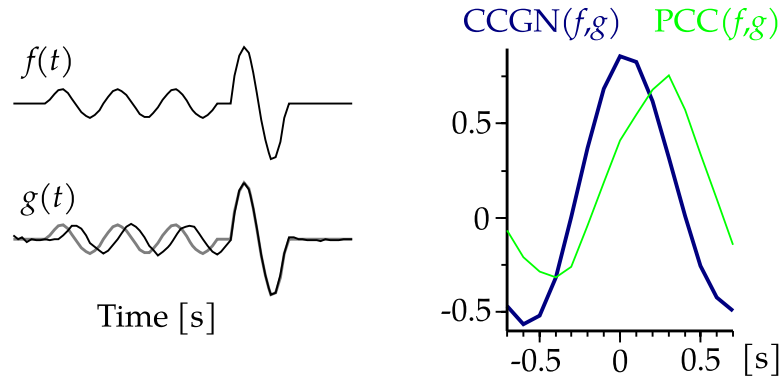


Figure 2.8 How the phase cross-correlation behaves differently from the classic cross-correlation (modified from Schimmel, Stutzmann, and Gallart 2011). The classic cross-correlation is more sensitive to the high-amplitude peak, while the phase cross-correlation favors the overall signal similarity.

where $\phi_j(t)$ are the instantaneous phases of the signals to be stacked, as defined in equation (2.5). The exponent ν can be used to fine-tune the sensitivity of the coherence measure.

While equation (2.6) contains the fundamental idea behind the phase-weighted stack, the actual implementation used in this work follows the more refined approach presented in (Schimmel and Gallart 2007), where the phase stack is based on the time-frequency decomposition of the traces obtained using the S transform. The S transform (Stockwell, Mansinha, and Lowe 1996) is a windowed Fourier transform

$$\mathcal{S}[u](\tau, f) = \int_{-\infty}^{+\infty} u(t)w(\tau - t, f)e^{-i2\pi t} dt$$

where the windows w are Gaussian and dependent on the frequency f . Their width is proportional to $|1/f|$:

$$w(\tau - t, f) = \frac{|f|}{k\sqrt{2\pi}} e^{-\frac{f^2(\tau-t)^2}{2k^2}}$$

with $k > 0$. The width of the window (and hence the resolution of the method) can be tuned by adjusting the k parameter. Schimmel and Gallart (2007) showed that the S transform is analytic for real signals at any fixed

frequency f , meaning that [equation \(2.6\)](#) can be rewritten as

$$C_{\text{ps}} = \left| \frac{1}{N} \sum_{j=1}^N \frac{S_j(\tau, f) e^{i2\pi f \tau}}{|S_j(\tau, f)|} \right|^{\nu}$$

where $S_j(t)$ is the S transform of the j -th cross-correlogram. The time-frequency phase-weighted stack S_{pws} is then obtained by multiplying the phase stack C_{ps} with the S transform S_{ls} of the linear stack of all the cross-correlograms:

$$S_{\text{pws}}(\tau, f) = C_{\text{ps}}(\tau, f) S_{\text{ls}}(\tau, f). \quad (2.7)$$

[Equation \(2.7\)](#) makes evident how the phase coherence C_{ps} is used to weight the samples of the linear stack. The inverse S transform is finally used to bring the time-frequency phase-weighted stack back to the time domain:

$$s_{\text{pws}}(t) = \mathcal{S}^{-1}[S_{\text{pws}}].$$

An essential workflow based on the phase cross-correlation and phase-weighted stack is shown in [figure 2.9](#), while a comparison of the stacks obtained using the combination of different techniques is shown in [figure 2.10](#).

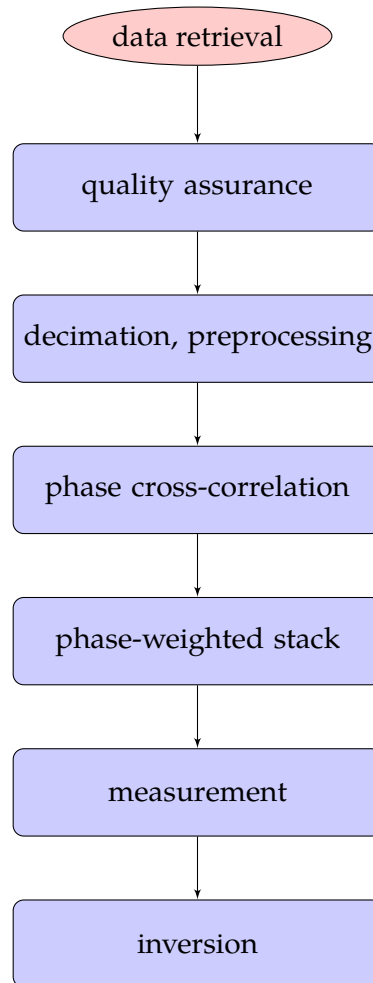


Figure 2.9 The stages of a simple seismic interferometry workflow based on the phase cross-correlation and phase-weighted stack.

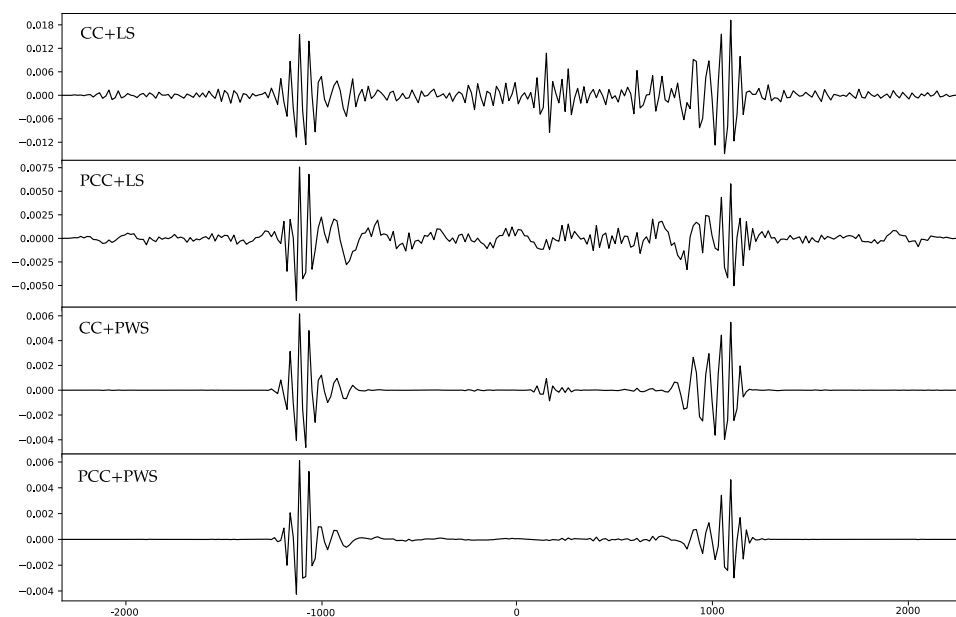


Figure 2.10 A comparison between different correlation and stacking techniques. In abscissa is lag time in seconds, the ordinate is a stack of correlation coefficients, whose absolute value is not directly comparable between the plots. From top to bottom, showing increasing improvements (better signal to noise ratio): a linear stack of classic cross-correlations; a linear stack of phase cross-correlations; a phase-weighted stack of classic cross-correlations; a phase weighted stack of phase cross-correlations. The seismograms are dominated by the high-intensity components of relatively low period, but the improvement is actually more prominent and important at the longer period.

Chapter 3

Modelling surface waves

3.1 Surface waves

General notions

Surface waves are the dominant component of correlograms: their amplitude is higher with respect to S and P-waves (figure 3.1). Surface waves owe their name to the fact that they normally propagate along the boundary between two zones with different elastic properties. The energy of surface waves decays as function of the distance r from the source as $1/r$, while the energy of body waves decays as $1/r^2$.

The two main surface wave types are Rayleigh waves, which have both compressional and shear motions, and Love waves, which are purely shear. Rayleigh waves result from the interaction of vertically polarized P and S-waves with the surface. Akin to ocean waves, Rayleigh waves wave move both vertically and horizontally in a vertical plane pointed in the direction in which the waves travel. Love waves can exist in the presence of a subsurface layer, and are only formed by horizontally polarized S-waves. Their motion is essentially that of S waves with no vertical displacement: it moves the ground from side to side in a horizontal plane at right angles to the direction of propagation. The work presented in the next chapter is based on measurements done on Rayleigh waves.

An important property of surface waves in complex media which allows us to obtain information on the structure of the medium in which they travel,

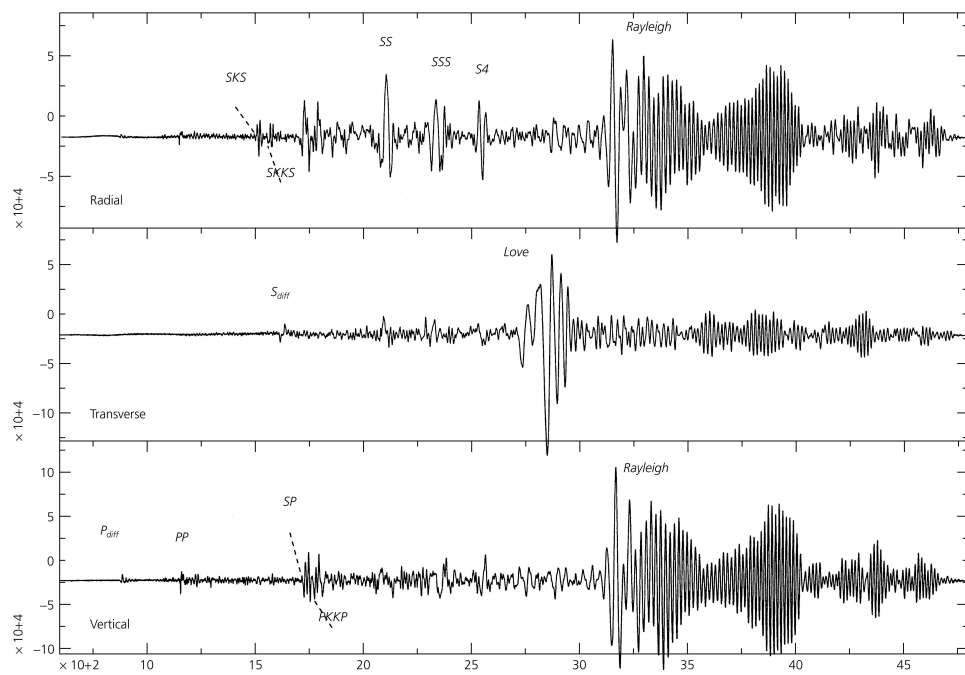


Figure 3.1 A full, three-components seismogram showing seismic noise followed by the arrival body waves and surface (Rayleigh and Love) waves from an earthquake (Stein and Wysession 2003, online resources). Note how the amplitude is dominated by the surface waves.

is the fact they are dispersive: waves with different frequencies (periods) travel at different speeds, and in this way they “sample” different depths of the medium they pass through. Long periods are sensitive to the characteristics of the layers placed at greater depths, while shorter periods are more sensitive to the shallow structure.

By filtering the seismic signal in different period bands, it is possible to measure the phase and group velocity of the surface wave between source and receiver (or between two receivers, in the case of seismic noise interferometry). These phase and group velocities are a function of the elastic parameters of the medium and are fundamental for tomographic studies and in general to get information of Earth’s internal structure. As [figure 3.2](#) shows, waves with shorter periods travel with lower velocities than waves with longer periods, as at greater depths the Earth has (on average) a higher density, which translates into higher wave velocities.

Rayleigh waves in a homogeneous halfspace

Following [Stein and Wysession 2003](#), we will now briefly review how Rayleigh waves can be described in a homogeneous half-space. Rayleigh waves are a combination of P and SV-waves which exist at the upper boundary of a half-space. The depth variable z starts from the free surface at $z = 0$ and is positive for deeper points. We consider waves propagating on the xz plane. The potential of the P and SV-waves are given by

$$\begin{cases} \phi = A \exp [i(\omega t - k_x x - k_x r_P z)] \\ \psi = B \exp [i(\omega t - k_x x - k_x r_S z)] \end{cases} \quad (3.1)$$

where ω is the angular velocity, t is time, k_x the component of the wave vector \mathbf{k} along the x direction, z is the depth, A, B are the amplitudes and $r_P = (c_x^2/v_P^2 - 1)^{1/2}$, $r_S = (c_x^2/v_S^2 - 1)^{1/2}$ are respectively the characteristic distances of the P and SV waves, and c_x is the velocity of the Rayleigh waves. In order to restrict the energy near the surface we need to apply two conditions. First we want the exponentials to decay with depth, which translates into the condition $c_x < v_S < v_P$. The other condition is the free surface

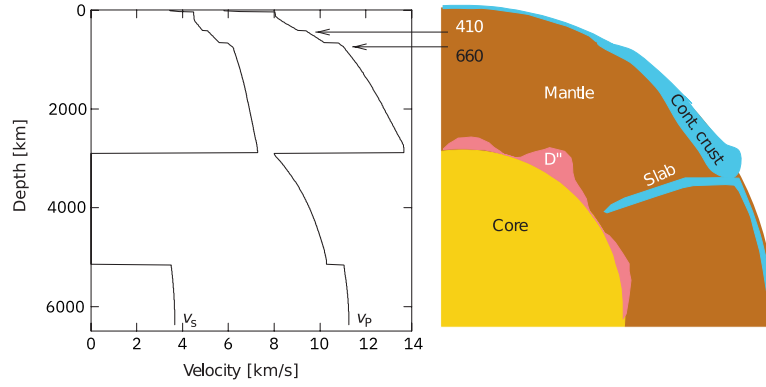


Figure 3.2 Velocity of seismic waves in the Earth versus depth (modified from Helffrich and Wood 2001). The negligible S-wave velocity in the outer core occurs because it is liquid, while in the solid inner core the S-wave velocity is non-zero.

condition, which means that the stress should vanish at the surface:

$$\begin{cases} \sigma_{xz}(x, 0, t) = 0 = 2r_P A + (1 - r_S^2) B \\ \sigma_{zz}(x, 0, t) = 0 = [\lambda(1 + r_P^2) + 2\mu r_P^2] A + 2\mu r_S B \end{cases}$$

where λ and μ are the Lamé parameters. After eliminating the Lamé parameters using $(1 + r_P^2) = c_x^2/v_P^2$ we end with a system of homogeneous equations:

$$\begin{cases} 2(c_x^2/v_P - 1)^{1/2} A + (2 - c_x^2/v_S^2) B = 0 \\ (c_x^2/v_S^2 - 2) A + 2(c_x^2/v_S^2 - 1)^{1/2} B = 0. \end{cases}$$

By solving this system in a Poisson solid (an isotropic elastic material for which the Lamé elastic constants λ and μ are equal) we find that the Rayleigh wave velocity is $c_x = (2 - 2/\sqrt{3})v_S$, which is slightly less than the shear velocity v_S . We can now derive an expression for the amplitude coefficients:

$$B = \frac{2 - c_x^2/v_S^2}{2r_S} A.$$

The potentials (3.1) are now completely defined and we can finally calculate the displacements u_x and u_z given that

$$u_x = \frac{\partial \phi}{\partial x} - \frac{\partial \psi}{\partial z}, \quad u_z = \frac{\partial \phi}{\partial z} - \frac{\partial \psi}{\partial x}.$$

Dispersion curves

The stratification of the soil makes the Rayleigh waves dispersive, meaning that their velocity is a function of the wave's frequency and consequently of the depth at which the wave propagates. This means that the velocity of a wave is a function of depth and of the elastic parameters of the medium at that depth.

The Preliminary reference Earth model (PREM) is a standard 1D model representing the average Earth properties as a function of planetary radius (Dziewonski and Anderson 1981). It includes a table of Earth properties, including its elastic properties, density, and attenuation. The model is given in tabular form; table 3.1 reports a few lines of the model, while its structure is shown schematically in figure 3.3. In figure 3.4 the group and phase velocities for the fundamental mode of the Rayleigh wave between 20 s and 300 s are shown for the PREM model. We can observe that the phase velocity increases with longer periods, while the group velocity remains bounded between 3.5 km/s and 4 km/s.

In order to perform a quantitative analysis of the dependency of the group velocity from the elastic parameters we consider the partial derivatives of the group velocity with respect to the elastic parameters. These partial derivatives are called *sensitivity kernels*. More in general, the sensitivity kernels are matrices whose elements are the partial derivatives of the observable quantity with respect to one of the depth-dependent elastic parameters, at a given period. The sensitivity kernels contain the information on how a physical parameter measured at the surface depends on the physical model variability with depth: they allow the information from a seismogram to resolve a model's parameter at depth. Figure 3.5 shows the sensitivity kernels of PREM for v_S at the periods of 30 s, 50 s, 80 s and 120 s, while figure 3.6 shows the sensitivity kernels from model of the Antarctic lithosphere used in (An et al. 2015).

r	d	ρ	v_{PV}	v_{PH}	v_{SV}	v_{SH}	Q_μ	Q_k
6371.0	0.0	1.02000	1.45000	1.45000	0.00000	0.00000	0	57823
6370.0	1.0	1.02000	1.45000	1.45000	0.00000	0.00000	0	57823
6369.0	2.0	1.02000	1.45000	1.45000	0.00000	0.00000	0	57823
6368.0	3.0	1.02000	1.45000	1.45000	0.00000	0.00000	0	57823
6368.0	3.0	2.60000	5.80000	5.80000	3.20000	3.20000	600	57823
6367.0	4.0	2.60000	5.80000	5.80000	3.20000	3.20000	600	57823
6366.0	5.0	2.60000	5.80000	5.80000	3.20000	3.20000	600	57823
6365.0	6.0	2.60000	5.80000	5.80000	3.20000	3.20000	600	57823
6364.0	7.0	2.60000	5.80000	5.80000	3.20000	3.20000	600	57823

Table 3.1 The first 10 entries from the Preliminary Reference Earth Model (PREM) as defined by Dziewonski and Anderson (1981). The radius r and depth d are measured in km, the density ρ in g/cm^3 and the velocities in km/s. Q_μ and Q_k are the shear and bulk quality factors.

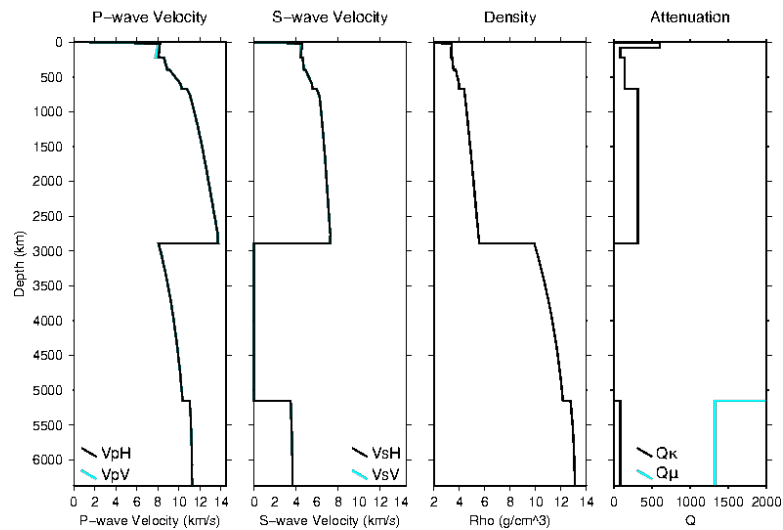


Figure 3.3 Velocity, density, shear and bulk quality factors Q_μ and Q_k of PREM (modified from Dziewonski and Anderson 1981). PREM's crust layer is defined to be 24.4 km, the weighted mean of the 35 km thick continental crust covering roughly 1/3 of the Earth's surface, and the 11 km thick oceanic crust accounting for 2/3 of the surface. This includes a 3 km thick water layer.

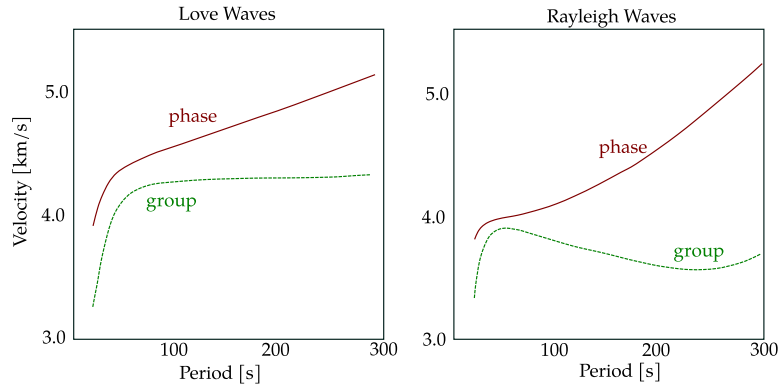


Figure 3.4 Phase and group velocities dispersion curves of Rayleigh and Love waves for PREM.

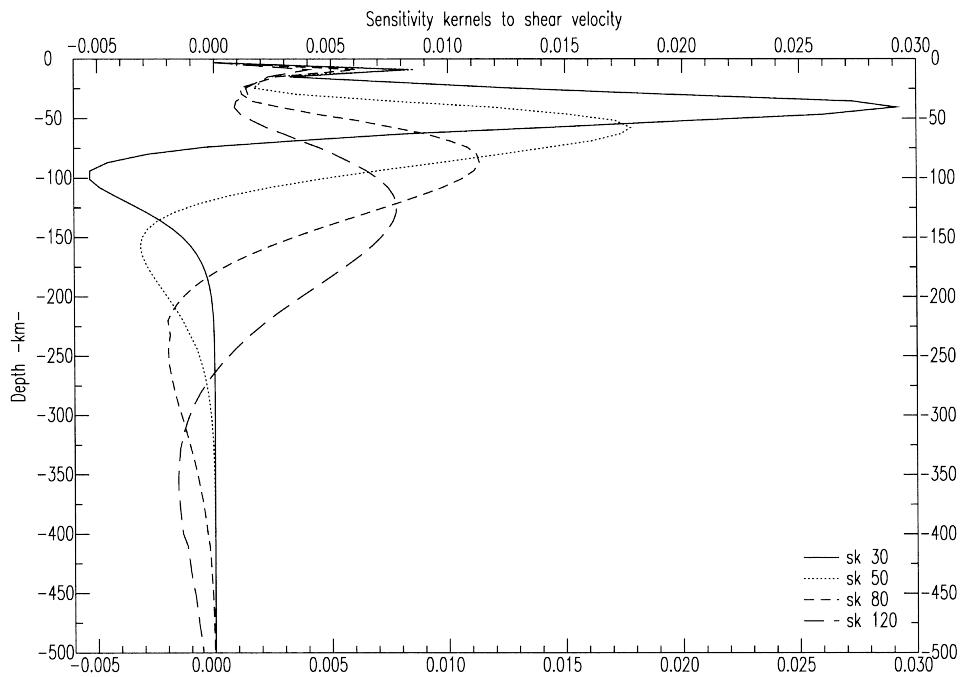


Figure 3.5 Fundamental mode group velocity partial derivatives with respect to v_s (sensitivity kernels) for PREM, computed at periods of 30 s, 50 s, 80 s, 120 s.

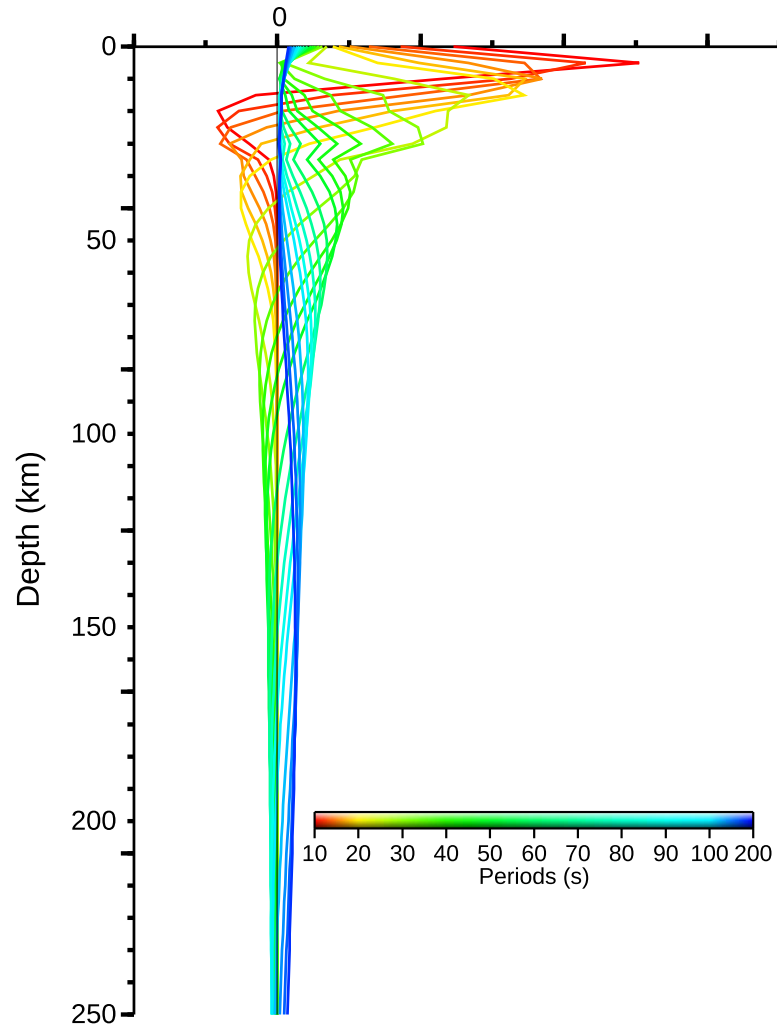


Figure 3.6 Sensitivity kernels of Antarctica from the lithosphere model used in (An et al. 2015) for periods between 30 s and 200 s.

3.2 Group and phase velocity measurements

The Frequency–Time ANalysis (FTAN)

Dispersion is the main peculiarity of surface waves: it means that velocity is dependent on frequency, so in a multi-layered medium the waves that make up the whole signal have different velocity according to medium properties. The packet of energy that propagates as surface waves contains a spectrum of wavelengths: the energy in the wave propagates as the envelope of the wave packet at the group velocity, while the individual waves that make up the wave packet travel with phase velocity.

The phase velocity $c(\omega)$ and the group velocity $U(\omega)$ are defined as

$$c(\omega) = \frac{\omega}{k(\omega)}, \quad \frac{1}{U(\omega)} = \left(\frac{dk(\omega)}{d\omega} \right)$$

where $k(\omega)$ is the wave number. The graph of $c(\omega)$ is the *phase velocity dispersion curve*, while $U(\omega)$ is the *group velocity dispersion curve*. They are related by

$$\frac{1}{U(\omega)} = \frac{1}{c(\omega)} + \omega \frac{d}{d\omega} \left[\frac{1}{c(\omega)} \right].$$

The FTAN (Frequency–Time ANalysis) method analyzes seismic signals both in frequency and in time domains. It allows extract the group velocity dispersion curves of the fundamental mode by separating the different oscillation modes of Rayleigh and Love surface waves. The method, first developed by Levshin, Pisarenko, and Pogrebinsky (1972) and Levshin, Ratnikova, and Berger (1992), represents a significant improvement to the multiple filter analysis originally developed by Dziewonski, Bloch, and Landisman (1969).

Let's now consider a signal $W(t)$ and its Fourier transform $K(\omega)$. The FTAN analysis consists in passing the dispersed signal through a system of narrow band-pass filters $H(\omega - \omega_H)$ with varying central frequency ω_H . These filters are to be chosen to achieve the best possible resolution without distorting the signal's phase. The optimal choice is to apply Gaussian filters

centered in ω_H and with width β :

$$H(\omega) = \frac{1}{\sqrt{2\pi}\beta} \exp\left[-\frac{(\omega - \omega_H)^2}{2\beta^2}\right].$$

and the combination of all the filtered signals is a complex function of the two variables ω_H and t :

$$S(\omega_H, t) = \int_{-\infty}^{+\infty} H(\omega - \omega_H)K(\omega)e^{i\omega t} d\omega$$

A contour map of $|S(\omega_H, t)|$ is called a FTAN diagram (or map), and it is used to visualize the dispersion curves. This map is characterized by a “ridge” of increased amplitudes: this is the area where the energy of the signal is concentrated and its peak identify the dispersion curve. [Figure 3.7](#) shows four FTAN diagrams.

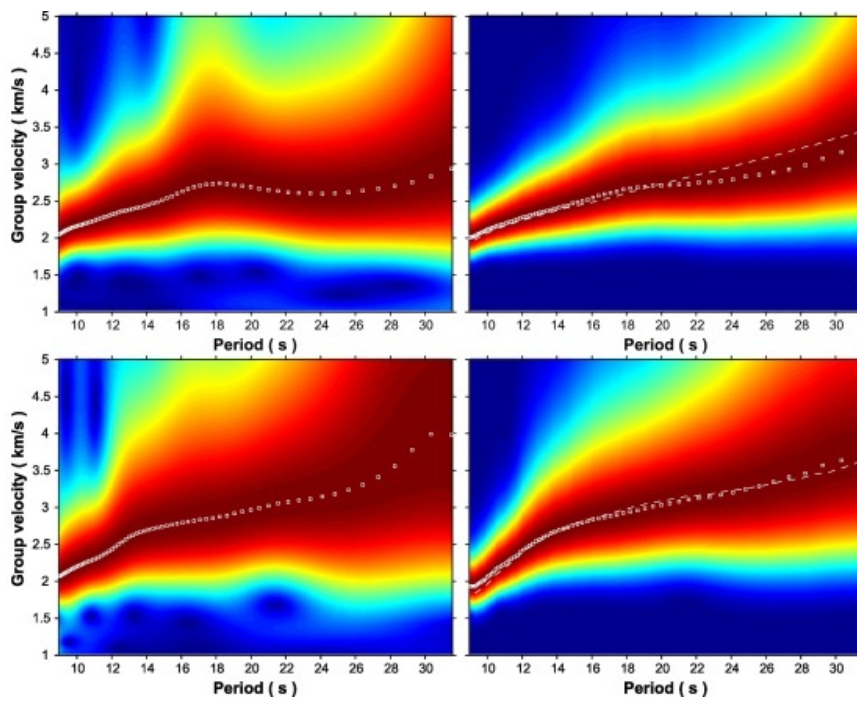


Figure 3.7 Four FTAN diagrams. The color scale is the logarithm of the square of the envelope of the analytic signal, normalized in each period band. The dark red “ridge” identifying the dispersion curve (white) is clearly visible.

Chapter 4

Data retrieval and processing

4.1 Introduction

Antarctic seismic data

Approaching the study of seismic data for Antarctica is not a trivial task. This begins from the data acquisition, made hard by the remoteness of the continent, which is difficult to reach, lacks any kind of communication and power infrastructure, and by its extreme climate which poses unique challenges to the personnel working there and to the scientific and logistic equipment. These practical obstacles immediately translate in less tangible but still prominent issues with the seismic data: antarctic data is scarce and the distribution of the seismic stations on the continent is uneven and in general sparse. Moreover, seismic stations are often installed in a less than optimal environment (e.g. on ice), suffer from power outages, and often operate out of their temperature specifications.

These difficulties also imply something else: being scarce, antarctic data precious, and all the possible effort has to be made to extract all the available information from it. The techniques described in this chapter work in this direction. While proven to be useful to deal with the peculiarities of antarctic seismic noise recordings, they are quite general and easily adaptable.

Computational resources

The data analysis has been performed on server with 48 Intel Xeon E5-4607 v2 cores running at 2.60 GHz (see [table 4.1](#) for the CPU specifications) and 377 GiB. The computing facility has been made available by the Bologna section of the National Institute of Geophysics and Volcanology (INGV).

The data retrieval, most of the pre- and post-processing and the data visualization have been performed with ObsPy, an open-source (LGPL-3.0) project dedicated to provide a Python framework for processing seismological data. It provides parsers for common file formats, clients to access data centers and signal processing routines which allow the manipulation of seismological time series (Beyreuther et al. 2010; Krischer et al. 2015; Megies et al. 2011).

Part of the pre-processing has been done with SAC (Seismic Analysis Code), a general purpose interactive program designed for the study of seismic time series developer by the Incorporated Research Institutions for Seismology (IRIS). SAC's analysis capabilities include general arithmetic operations, Fourier transforms, three spectral estimation techniques, IIR and FIR filtering, signal stacking, decimation, interpolation, correlation, and seismic phase picking.

The central part of the analysis (the noise cross-correlation and the phase-weighted stack) has been done with specialized code written and made available online by Schimmel (2018) and Ventosa (2018). The velocity measurements were performed with the AFTAN tool developed at the University of Colorado Boulder (*Research Products from CU-Boulder* 2018). References to the associated scientific publications are given in the relevant sections.

Family	Intel Xeon E5 v2
Processor Number	E5-4607V2
Number of cores	6
Number of threads	12
Base frequency	2.60 GHz
Cache	15 MB
TDP	95 W

Table 4.1 Intel Xeon Processor E5-4607 v2 technical specifications.

Most of the data analysis that follows is a so-called *embarrassingly parallel* workload, as there is little or no dependency or need for communication between the parallel tasks. The parallelization of the workload has been achieved using Python's `concurrent.futures` module and GNU Parallel (Tange 2018) to complement the standard Unix toolchain.

The plotting of the models has been done with the Generic Mapping Tools (GMT), an open source (LGPL-3 or later) collection of command-line tools for manipulating geographic and Cartesian data sets (Wessel et al. 2013).

4.2 Raw data operations

Data availability

The first issue any study based on Antarctica's seismic noise faces is the one of data availability. The first continuous data recorded south of 60° S and publicly available in the Federation of Digital Seismograph Networks dates back the late 1980s, but it is not until the mid 1990s that more than ten stations can be counted on the whole continent. The number of stations steadily increased, peaking at 129 stations for 2010, thanks to the extraordinary campaigns happened during the International Polar Years 2007–2009.

An all-inclusive survey of all the publicly available data as of today counts about 350 stations, but the whole picture can't be represented by a single figure. Given that many of these stations were operative in different time periods, the actual useful number is quite smaller when there is a time constrain in place as it happens, for example, with cross-correlation studies. Moreover, the distributions of the seismic stations over the continent is very uneven: some regions are well covered (Victoria Land, part of the Antarctic peninsula, coastlines in general), while the whole mainland East Antarctica is almost uncovered. Representative of this one fact: only two permanent observatory stations are operative on the Antarctic plateau; one is located at the South Pole Station and operated by the United States Geological Survey, while the other is at the Concordia research station (Dome C), and is jointly operated by the Italian National Institute for Geophysics and Volcanology and the French GEOSCOPE network. For each year between 1990 and 2017

table 4.2 shows the number of stations installed south of 60° for which data is available in the FDSN federation.

Figure 4.1 is a map of the subset of these station for which at least one year of data is available: the coverage is clearly sparse and not homogeneous, as seismic stations were mostly installed in areas that are geologically more interesting. This is the reason why the coverage of East Antarctica is so scarce. These stations could ideally bring to the ray coverage shown in figure 4.2, which a pretty optimistic: as we will see, other factors other than the simultaneous recording of seismic noise are relevant in deciding if a station pair will bring useful correlogram stacks.

Data retrieval

The data retrieval has been done using the ObsPy's *mass downloader* functions, which are able to query and integrate data from any number of FDSN providers simultaneously. The library aims to submit download requests in a way that is convenient for user without having to worry about the specific data center issues. The module allows to

1. specify the geographical region from which to download data;
2. define a number of other restrictions (temporal, data quality, ...);
3. launch the download.

The mass downloader module will acquire all waveforms and associated station information across all known FDSN web service implementations producing a clean data set ready for further use. It works by figuring out what stations each provider offers and downloading MiniSEED¹, dealing with the data issues like missing or incomplete data, duplicate data across data centers, resuming interrupted downloads and performing optional quality control by assuring that the data has no-gaps or overlaps. The library also takes care of downloading the relevant metadata in StationXML format.

1. The Standard for the Exchange of Earthquake Data (SEED) is a data format intended primarily for the archival and exchange of seismological time series data and related metadata. *MiniSEED* is a stripped down version of SEED containing only waveform data, without metadata

year	#	year	#	year	#
1990	1	2000	27	2010	129
1991	3	2001	55	2011	117
1992	3	2002	52	2012	100
1993	7	2003	59	2013	90
1994	6	2004	37	2014	90
1995	11	2005	41	2015	83
1996	19	2006	23	2016	69
1997	16	2007	58	2017	61
1998	22	2008	82		
1999	28	2009	86		

Table 4.2 Number of seismic stations south of 60° for which seismic data is available in the FDSN federation.

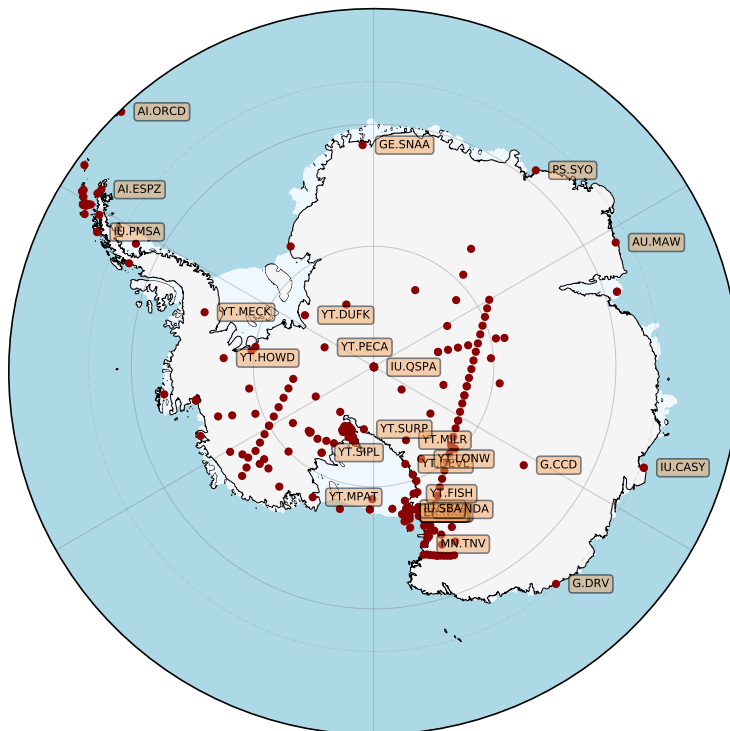


Figure 4.1 Map of the antarctic seismic stations for which at least one year of data is available. The ones with a label have at least four years of available data.

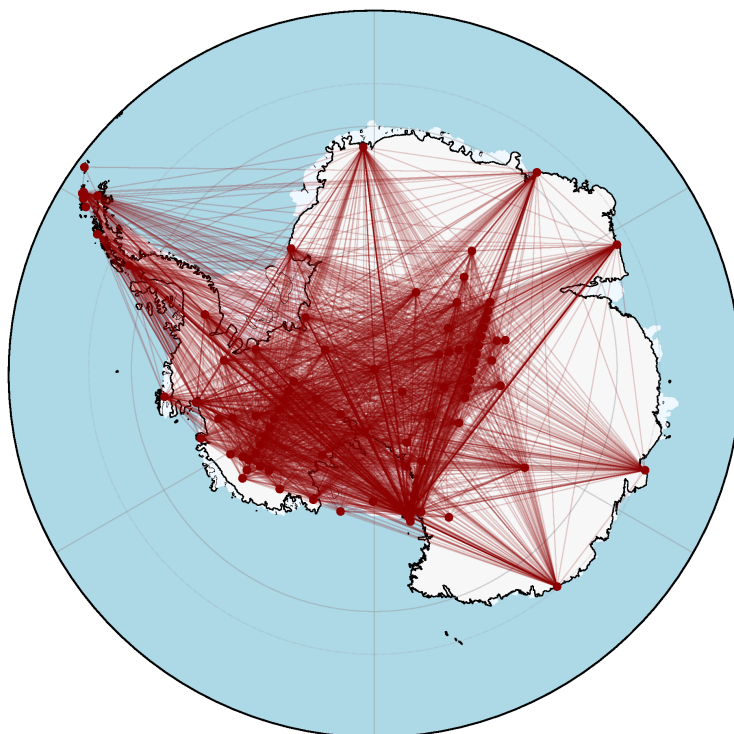


Figure 4.2 The theoretical availability of pairs of seismic stations in Antarctica having enough data in common to perform a noise cross-correlation. Even in this optimistic map it is evident how parts of the continent do not have a significant coverage.

The mass downloader has been programmed to download the vertical component from any station from the beginning of time to 31 December 2017, regardless of gaps or overlaps, which are taken into account in a later stage of the analysis. Data are downloaded for any location (a *location* being an additional number to identify different instruments installed as part of the same seismic station) and sampled at 1 sps, or at the lowest available sampling rate of only higher sampling rates are available. This sampling rate is more than enough for a continental scale study, as it allows to work up to relatively high frequencies (theoretically up to 0.5 Hz). For many stations data is published only at higher sampling rates: 20 sps, 40 sps or even 100 sps, and it will be necessary to decimate this data. The mass downloader library takes care of dividing the download data in daily chunks (86 400 seconds).

At the end of this process data for 356 stations have been download more than 360 000 daily chunks, for a total of about 380 GiB before downsampling. During this intensive data retrieval operation a bug in ObsPy emerged, I reported to the upstream developers and got it been fixed: <https://github.com/obspy/obspy/issues/2029>.

4.3 Preprocessing

The preprocessing stage prepares the data to be fed to the cross-correlation code. The process happens in several stages, which are all applied to the available daily chunks.

First the data are decimated (downsampled), as even 1 sps happens to be more than what is needed, and decimated speeds up the computation in a significant way. A finite response filter (FIR) is applied to the data as it is being decimated to prevent the aliasing effects normally associated with downsampling digitized analog signals. This filter also preserves the phase information.

Some quality assurance checks are then done on this decimated data. In principle this could be done before downsampling, but decimating is very cheap and speeds up everything that comes after it. In this stage the daily chunks that present very long gaps, overlaps or heavy amplitude anomalies are discarded. For observatory stations these issues normally correspond

to maintenance being done to the station and are therefore more frequent during the austral summer.

This shortlisted data has any linear trend or offset removed, so the signals always have zero mean. These data are then filtered in the frequency band of interest. This filtering is quite wide: it goes between about half of the Nyquist frequency and the frequency corresponding to the period of 320 s. The purpose of this filtering is to remove the very long frequency components of the signal. The filtering is applied in two passes, which results in a non-causal filter impulse response that does not shift the signal's phases.

After tapering the signals the instrument's response is removed (deconvolved). The previous filtering ensures that the signal has no frequency components that could get amplified by the response deconvolution, while the tapering is important to stabilize the operation. A non-tapered signal (that is, a finite signal that does not go smoothly to zero at its beginning and end) can result in an unstable deconvolution operation. The correct choice of the filter corner frequency and of the tapering length is important for the success of this operation.

Any linear trend of the signal is again removed, and the data series are finally converted in SAC format with the right header parameters, ready to be fed to the cross-correlation and stacking codes.

4.4 Cross-correlation and stacking

After the preprocessing the data is fed to the phase cross-correlation code. This operation is one of the most time-consuming of the whole process, but luckily is it heavily parallelizable. This is done by wrapping the calls to the cross-correlation program in a Python script which will take call the actual binary using the `concurrent.futures` module: a high-level interface for asynchronously executing callables. The asynchronous execution can be performed with threads or separate processes. Both implement the same abstract interface. Given the nature of the task, this is more efficient than a parallelization done with OpenMP² or similar paradigms.

2. *OpenMP* is an application programming interface (API) that supports multi-platform shared memory multiprocessing programming in various programming languages. It gives programmers a simple and flexible interface for developing parallel applications.

The output of the cross-correlation is a set of cross-correlograms, one for each data chunk. These are now to be stacked, which will be done with the phase-weighted stack defined in [chapter 2](#). Some sample results of this operation for the stations in [table 4.3](#) are shown in [figures 4.3 to 4.11](#). In these figures the abscissa is a phase-weighted stack of phase-cross correlations.

The pairs of stations to correlate are selected upon their common data availability, while the correlation time window (the lag time) is chosen automatically for each pair based on the distance between the stations and a reasonable wave velocity. Far stations will need longer lag times, compare for example [figure 4.3](#) and [figure 4.6](#).

Station code	Location	Latitude	Longitude
AU.MAW	Mawson Station	67.604° S	62.871° E
G.DRV	Dumont d'Urville	66.664° S	140.002° E
GE.SNAA	Sanae Station	71.670° S	2.837° W
IU.CASY	Casey Station	66.279° S	110.535° E
IU.QSPA	South Pole	89.928° S	144.438° E
IU.SBA	Scott Base	77.849° S	166.757° E

Table 4.3 Approximate coordinates of the seismic stations for which the correlograms are shown in [figures 4.3 to 4.11](#).

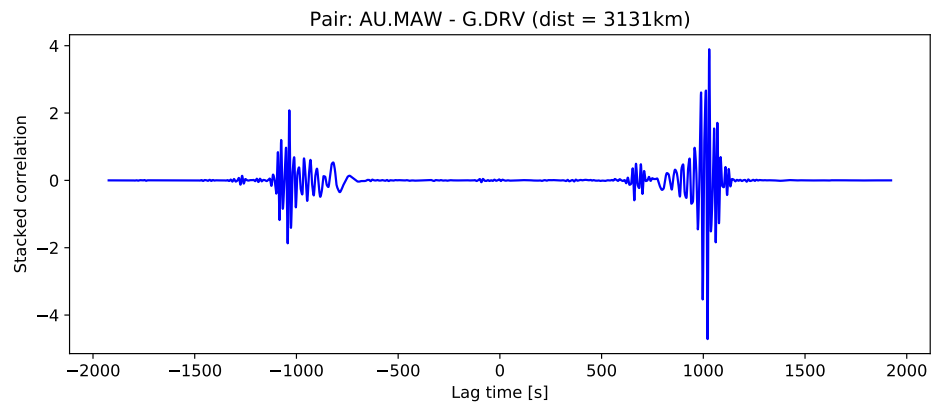


Figure 4.3 Cross correlation: AU.MAW G.DRV.

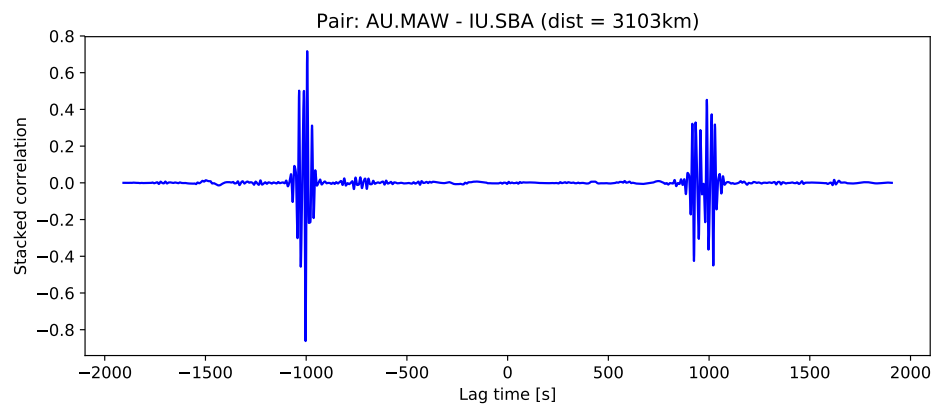


Figure 4.4 Cross correlation: AU.MAW IU.SBA.

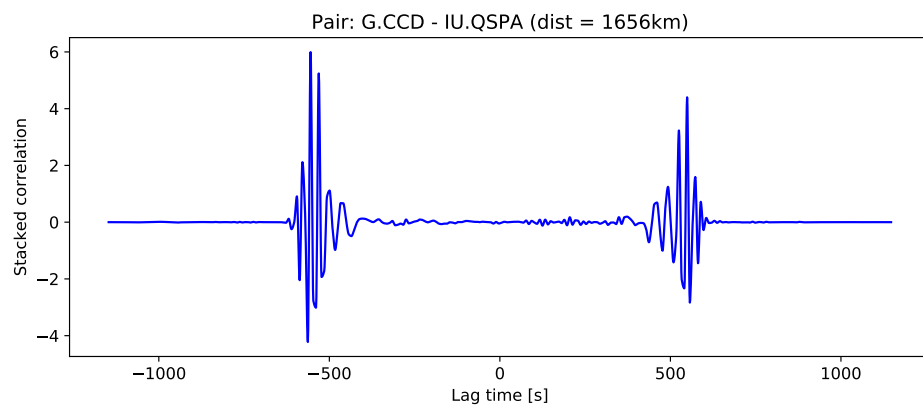


Figure 4.5 Cross correlation: G.CCD IU.QSPA.

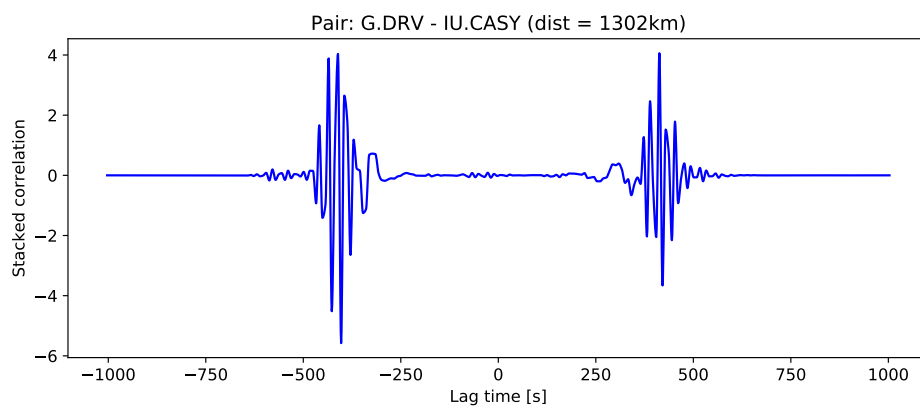


Figure 4.6 Cross correlation: G.DRV IU.CASY.

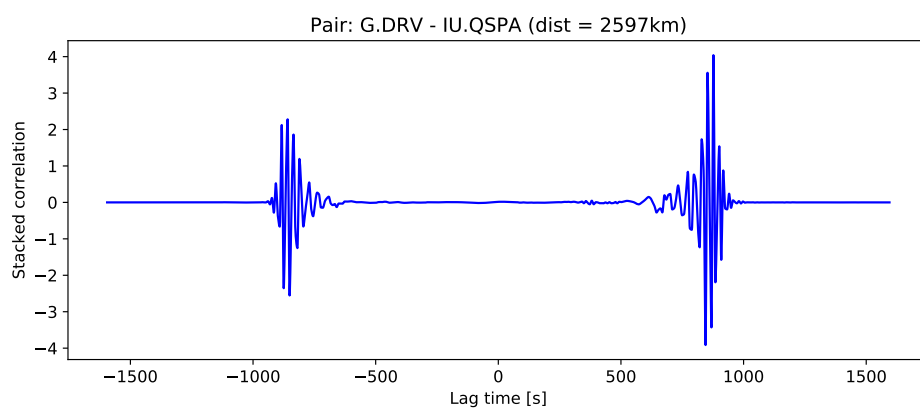


Figure 4.7 Cross correlation: G.DRV IU.QSPA.

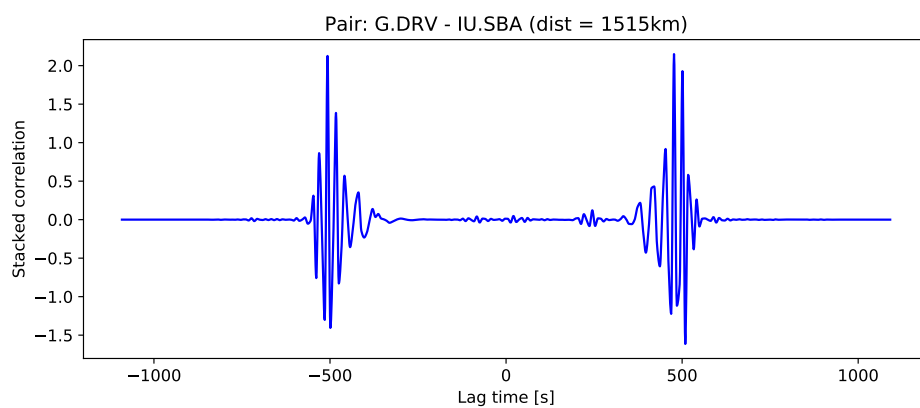


Figure 4.8 Cross correlation: G.DRV IU.SBA.

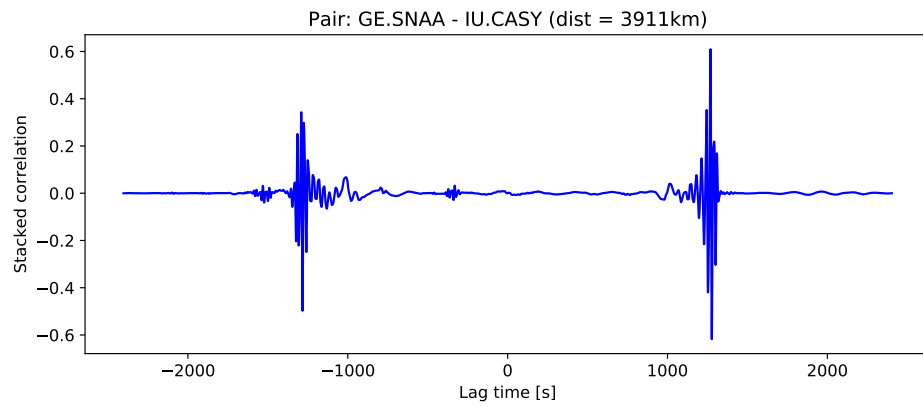


Figure 4.9 Cross correlation: GE.SNAA IU.CASY.

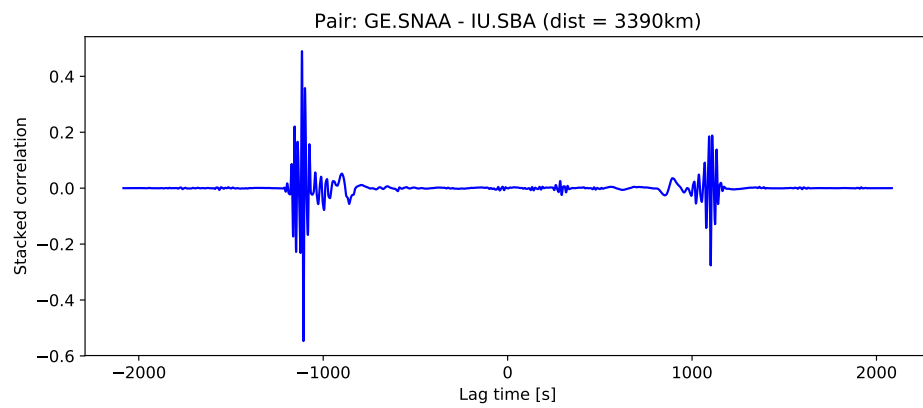


Figure 4.10 Cross correlation: GE.SNAA IU.SBA.

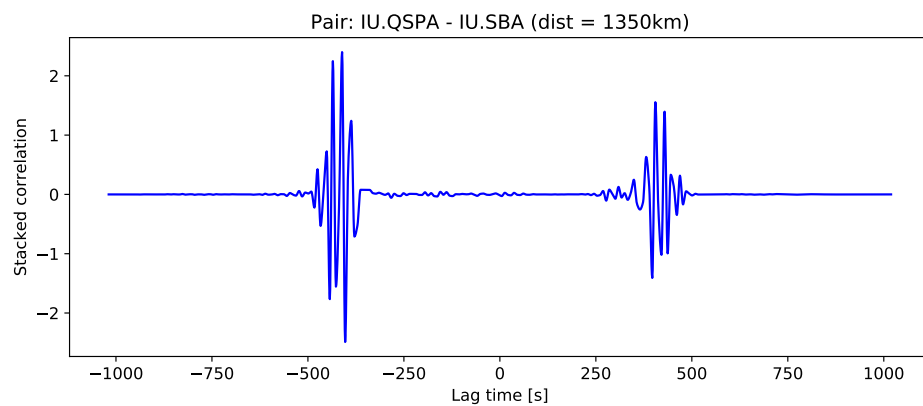


Figure 4.11 Cross correlation: IU.QSPA IU.SBA.

4.5 Velocity measurements

Automatic FTAN

The group and phase velocity measurements have been done using the FTAN method explained in 3.2. What has been used more specifically is Automatic FTAN (AFTAN) implementation as described in (Bensen et al. 2007) and publicly available (*Research Products from CU-Boulder 2018*). The AFTAN converts a time series of cross-correlation functions into frequency-time diagrams of signal power as a function of frequency and group time using a multiple narrow-band filtering. It then automatically provides measurements of group and phase velocities together with estimates of signal/noise ratios of these measurements.

The AFTAN code expects a (quasi) symmetric waveform as the one shown in [figure 2.7](#), the causal and acausal components are then averaged. Some FTAN diagrams for the already shown correlograms are shown in [figures 4.12 to 4.16](#). In these figures the blue line is the dispersion curve (the ridge of the FTAN diagram), while the black line is PREM, which is not expected to be a good fit for continental crust at the lower periods. For an explanation of the color scale see the caption of [figure 2.2](#).

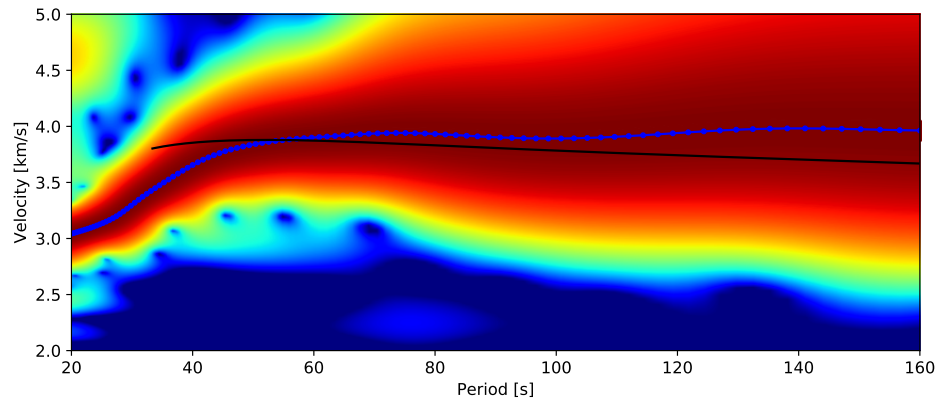


Figure 4.12 Dispersion curve for: AU.MAW G.DRV.

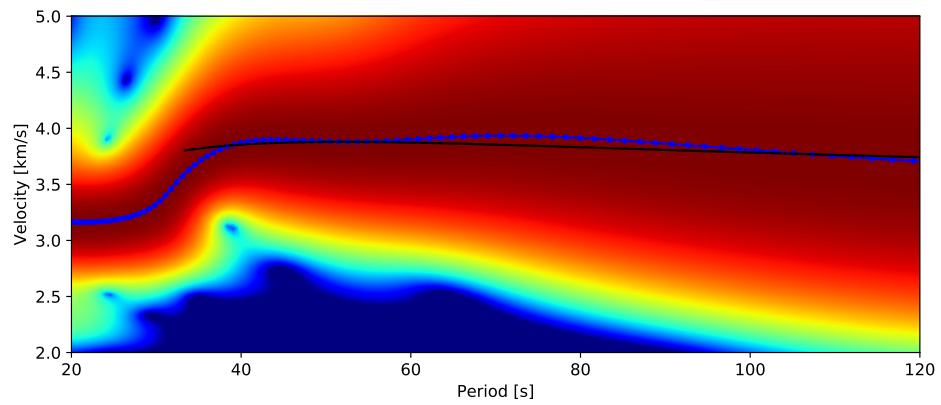


Figure 4.13 Dispersion curve for: G.DRV IU.CASY.

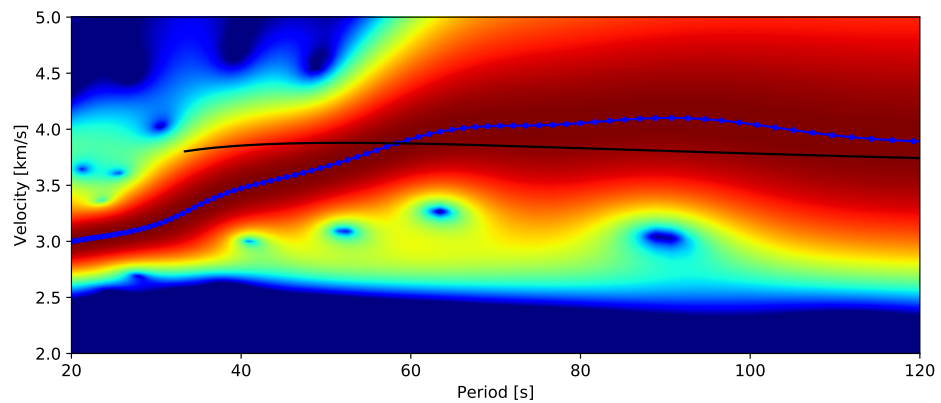


Figure 4.14 Dispersion curve for: G.DRV IU.QSPA.

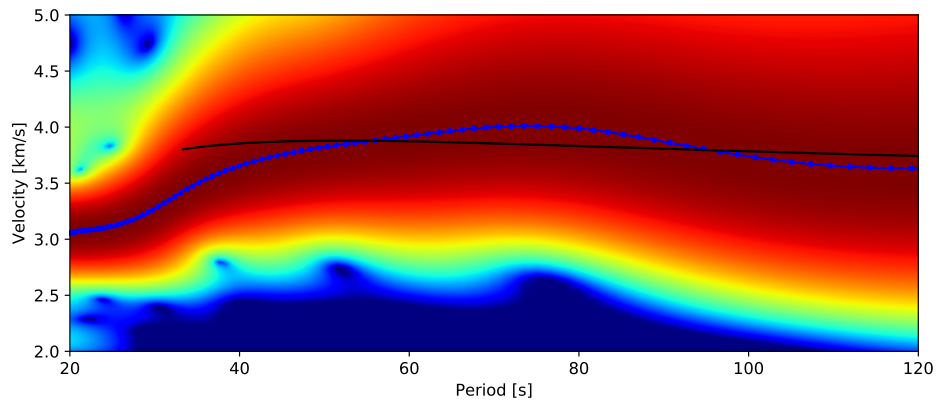


Figure 4.15 Dispersion curve for: G.DRV IU.SBA.

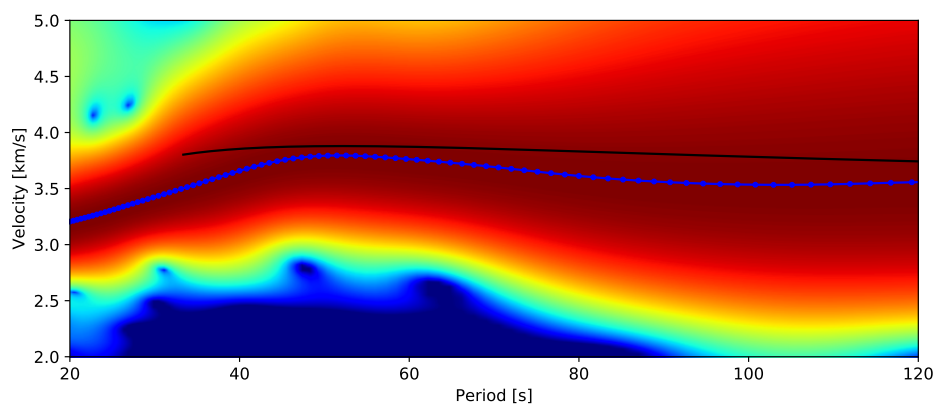


Figure 4.16 Dispersion curve for: IU.QSPA IU.SBA.

The problem of the “spectral notches”

What explained so far was enough to perform velocity measurements on many stacks of correlograms, however a significant subset of the available stacks did exhibit “spectral notches” in the FTAN diagram like the one shown in [figure 4.17](#). While this phenomenon is known and sometimes expected when working with earthquake data and may depend on the signal’s source, “spectral notches” are not expected when working with seismic noise.

It has been found that a hybrid, two-stage stack heavily mitigates the issue. In the first stage, a linear stack of groups cross-correlograms happens, then these pre-stacks are stacked using the phase-weighted stacking method. This approach did bring to a major improvement in the dispersion curve, causing the spectral notches to almost disappear. The rationale behind this improvement is that the phase-weighted stack requires some coherence to already be present in the input data, and the daily cross-correlograms are probably not coherent enough for the method to work correctly. A linear pre-stack allows for some coherence to build up, then the phase-weighted stack works as expected on the pre-stacks.

The two-stage phase-weighted stack has been shown to improve noise attenuation, quality of the extracted signals and convergence speed (Ventosa, Schimmel, and Stutzmann 2017). The same paper also described the *time-scale* phase-weighted stack (ts-PWS) (opposed to the *time-frequency* PWS described in [chapter 2](#)). The ts-PWS is an alternative formulation of the phase-weighted stack that uses complex frames of wavelets to build a time-frequency representation which computationally more efficient while preserving the performance and flexibility of the time-frequency PWS defined in [section 2.4](#) (Ventosa, Schimmel, and Stutzmann 2017). The actual implementation I have used has been written by the first author of the same paper (Ventosa 2018).

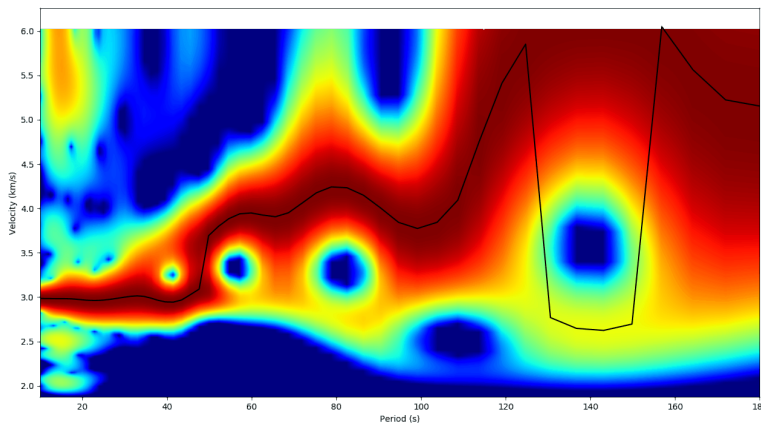


Figure 4.17 A FTAN diagram showing “spectral notches”.

4.6 Convergence measurements

While working with the cross-correlation stacks, several questions arose. Do we have enough data? Is the result of the stack converging to a stable and physically meaningful result? To answer these questions, we visualize the convergence and stability of the dispersion curves as the relative difference from the stack made with all the available data. This brings to “convergence plots” like the ones in figures 4.18 and 4.19.

These stability plots visualize the speed of convergence of the stacks when more daily cross-correlograms are added, and check that the stack actually converges to a stable solution. As it can be seen from the figures, the speed and quality of the convergence varies greatly with the period that is considered. While for shorter periods the convergence is very fast and stable, this is not the case for longer periods, where thousands of stacked days may be necessary to be able to reach a stable solution.

Given this possibility to evaluate the quality and relevance of each ray and hence filter out the outliers from the dataset, it is possible to show the actual ray coverage of the dataset. This is done in figure 4.20, where rays for which the group velocity at $T = 30$ s is lower than the regional average (computed over all the available rays) are red, while rays whose group velocity at $T = 30$ s exceeds the regional average are represented in blue. The difference in coverage (and hence in the expected resolvable power) between West Antarctica and East Antarctica is apparent.

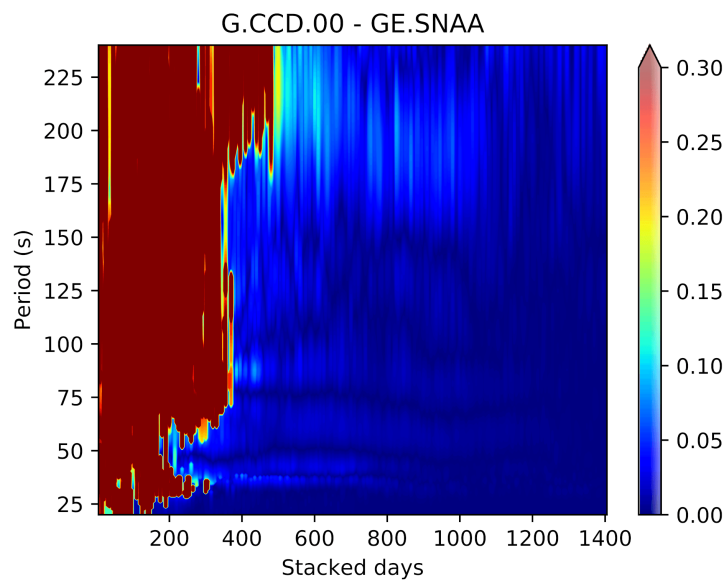


Figure 4.18 Convergence plot for the noise cross-correlation between G.CCD (Concordia Station, Dome C) and GE.SNAA (SANAE Station). The convergence is computed relatively to the full stack. While about 400 days are enough to get stable measurements up to a period of 175 s, about two years of data are necessary to reach the same result for longer periods. The color scale indicates the relative difference from the full stack.

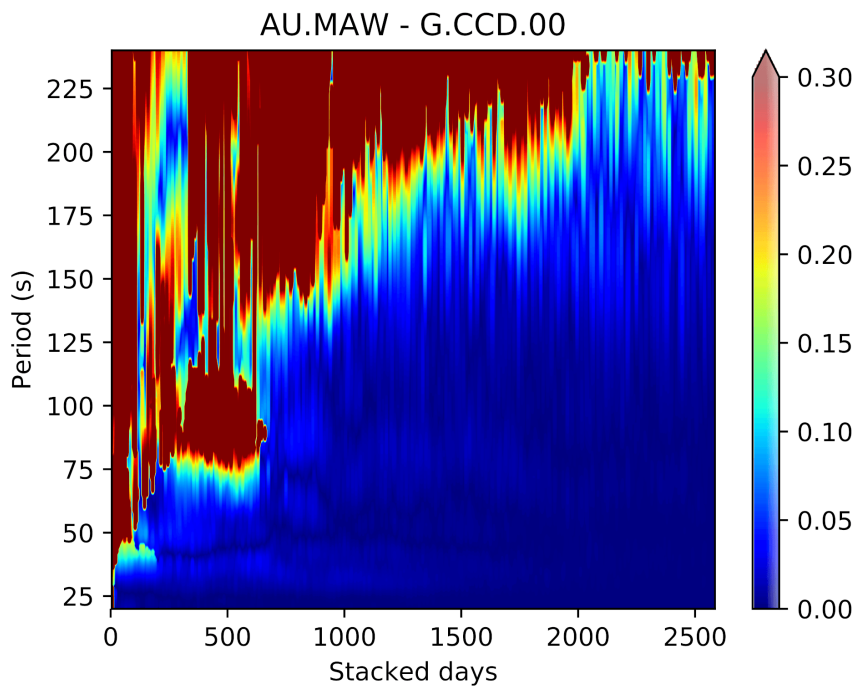


Figure 4.19 Convergence plot for the noise cross-correlation between G.CCD (Concordia Station, Dome C) and AU.MAW (Mawson Station, Holme Bay). The convergence is computed relatively to the full stack. In this case the convergence is not as steep as in [figure 4.18](#). The longer the period, the more data is necessary to stack to get stable measurements. The color scale indicates the relative difference from the full stack.

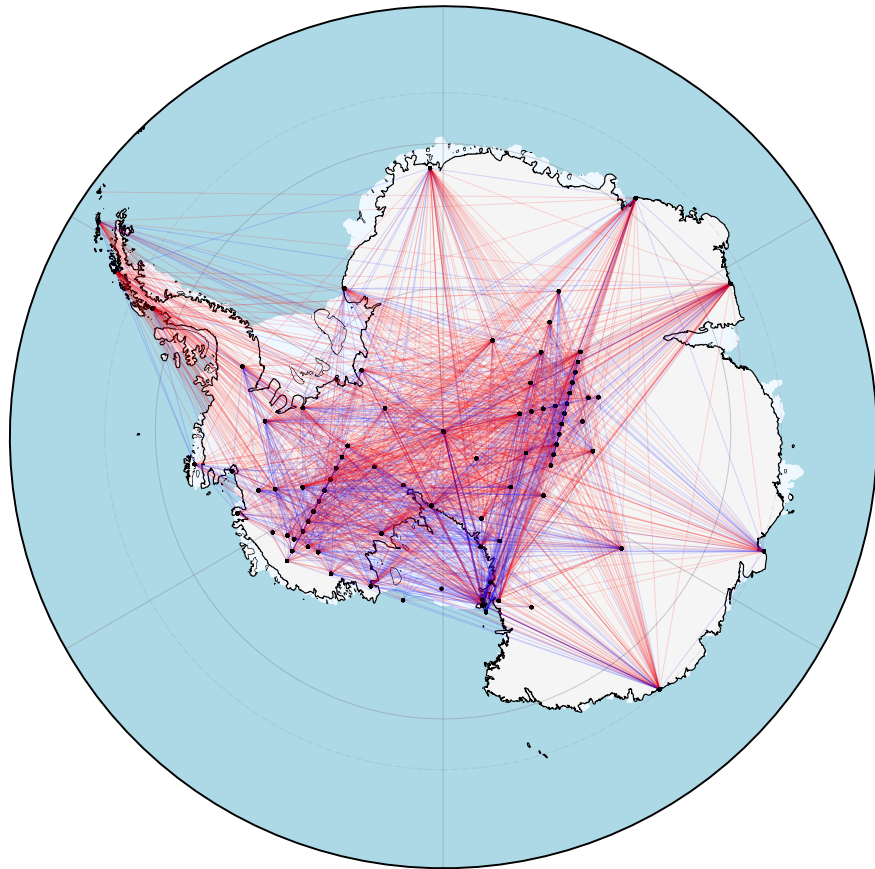


Figure 4.20 Actual ray coverage of the dataset. Rays for which the group velocity at $T = 30$ s is lower than the regional average are red, while rays whose group velocity at $T = 30$ s exceeds the regional average are represented in blue.

4.7 Seasonal variations

While studying the aforementioned convergence plots, I noticed some peculiar cases where adding more days to the stack didn't bring to a monotonic behavior toward the final solution, but exhibited a periodical behavior with a period of roughly one year. One of these cases is represented in [figure 4.21](#).

The intensity of this behavior does vary in a significant way between different pair of stations, but there is clearly a pattern calling for an explanation. The question at this point is: is convergence faster (that is: do we get better data) during the austral winter months? How much is this effect period-dependent? How much does it depend on the location on the station, for example on the distance from the coast?

We proceeded toward this investigation separating the analysis for the data recorded in the austral summer (considered as the period between the first of November and the end of March of the following year) and the data recorded in the austral winter (the rest of the year). The results of this division are shown in [figures 4.22](#) and [4.23](#). What is evident from these plots is that, especially for the longer periods, the convergence is much faster when using data from the winter months and, as [figure 4.21](#) shows, adding data from summer days could actually be harmful to the analysis.

In [figures 4.22](#) and [4.23](#) the lower plot is the relative difference of the stack from PREM, taken as a reasonable reference model. From these plots it can be seen how in this case the convergence to a stable result and the convergence to a physically meaning full result (a result compatible with PREM) go in a good measure together. The velocity measurements are not expected to fit PREM very well for the shorted periods: PREM is a *global* average model and this means that it described the faster oceanic crust better than the continental crust. Our data, however, are on continental crust. This should not cause any worry, as here PREM is taken as a coarse grained indicator.

This empirical observation needs to be explained, and there are a few plausible hypotheses, both related to the extreme differences in climate between the Antarctic summer and winter. The most plausible explanation of this difference is the presence and extension of the sea ice. Sea ice reaches

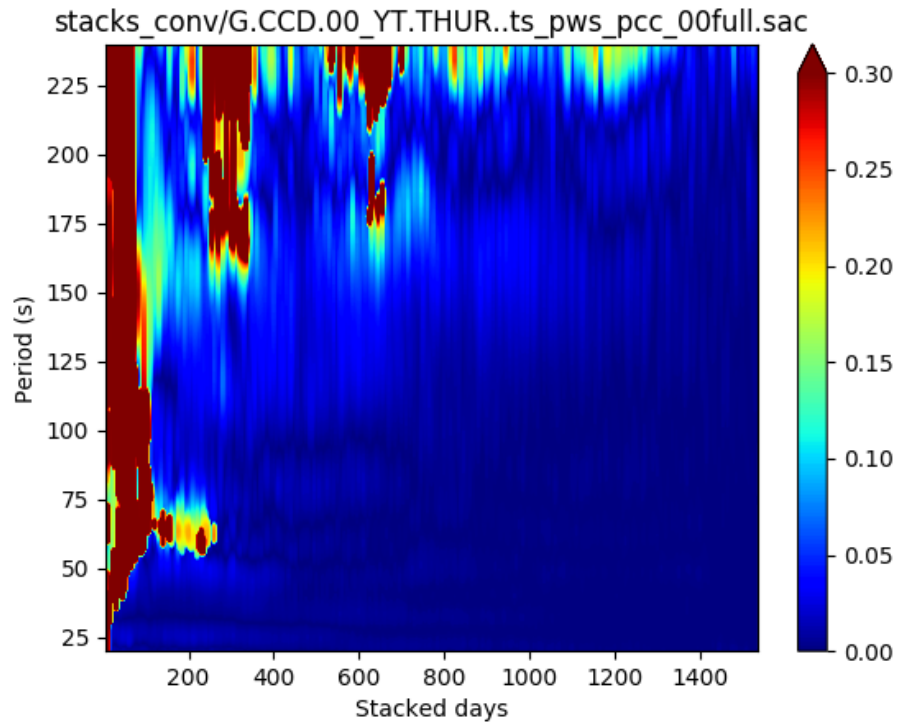


Figure 4.21 Strong seasonality effect with a period of about one year.

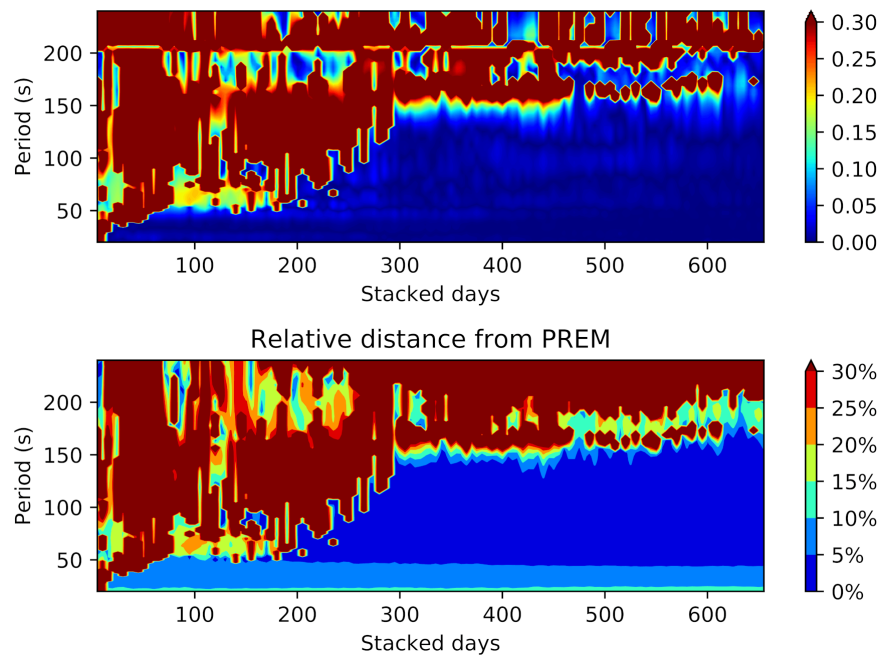


Figure 4.22 Convergence using the austral summer month. Lower plot: distance from PREM.

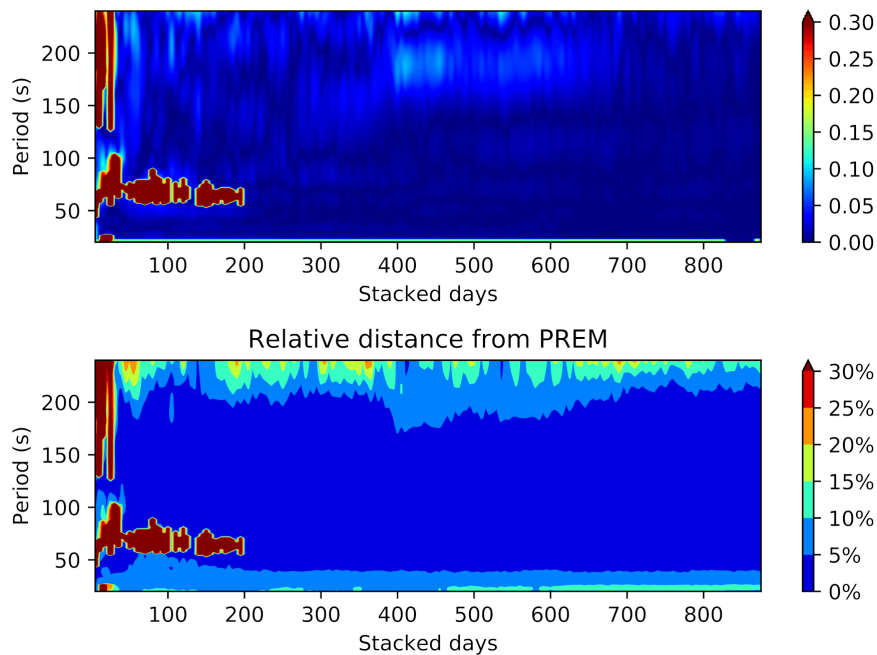


Figure 4.23 Convergence using the austral winter months. Lower plot: distance from PREM.

its maximum extension in September, reaching up to $18 \times 10^6 \text{ km}^2$. This means that the noise coming from the activity of the sea will arrive much attenuated to the continent, resulting in better correlations in the periods that are outside of the frequency band of noise caused by ocean waves (the microseism signals, localized roughly between 5 s and 30 s).

Anthropic noise can likely be ruled out as a cause of the observed difference, as the most important differences are in frequency bands that are outside of the band of anthropogenic noise sources.

Chapter 5

Inversion

A synthetic version of this chapter is going to be submitted as: **P. Legovini**, A. Morelli, and M. Schimmel (in preparation). Seismic Tomography of Antarctica using ambient seismic noise.

5.1 Seismic tomography

Seismic tomography is a seismic imaging technique used to study the internal structure of the Earth based on the knowledge of how seismic waves propagate through it.

In seismic tomography a physical model (the Earth's structure) is constructed from a set of indirect observations made on seismic waves. This kind of problem is called an *inverse problem*, and as the name suggests to solve it it is necessary to work backwards: the observable quantities are the starting point and the other characteristics of the system are derived from these.

In the specific case, seismic travel time data are compared to an initial velocity model; this model is then modified until the best possible fit between the model predictions and observed data is found. The modified model will then reflect the Earth's internal structure. The solutions to the inverse problem are often not unique and they have to be constrained with some *a priori* information that can't be derived from the data.

Solving an inverse problem in a physically meaningful way is a challenging task and a number of mathematical tools have been developed around it.

We will follow the theory as developed in (Tarantola 2005).

The linear inverse problem

In general in an inverse problem we want to infer the parameters of an unknown model \mathbf{m} given the experimental observations \mathbf{d}_{obs} and a theory g that is able to relate the model with the observations, so that

$$\mathbf{d}_{\text{obs}} = g[\mathbf{m}].$$

In travel-time seismic tomography \mathbf{d}_{obs} are the travel-time observations, \mathbf{m} is a velocity model (or a slowness model), while g is a linear operator that we can represent with the matrix G :

$$\mathbf{d}_{\text{obs}} = G\mathbf{m}.$$

This problem can be solved as a least-squares problem, looking for the vector \mathbf{m} that minimizes the difference $\|\mathbf{d}_{\text{obs}} - G\mathbf{m}\|$. In this ideal case the least-squares solution is given by

$$\mathbf{m} = (G^T G)^{-1} G^T \mathbf{d}_{\text{obs}},$$

which is valid when the problem is overdetermined, that is: we have more equations than unknowns, and $G^T G$ is not singular. In real scenarios this tomographic inverse problem is not well posed, as $(G^T G)$ can be singular or almost singular because of the uneven ray coverage of the area being studied. In this case the solution has to be constrained by adding some *a priori* information on the model. One possibility is to complement the minimization constrain with some conditions on the norm and the roughness of the solution. The problem becomes:

$$\left\{ \begin{array}{l} \mathbf{d} - G\mathbf{m} = 0 \\ \gamma \mathbb{1}(\mathbf{m} - \mathbf{m}_0) = 0 \\ \lambda H\mathbf{m} = 0 \end{array} \right. \quad \begin{array}{l} (5.1a) \\ (5.1b) \\ (5.1c) \end{array}$$

where $\mathbb{1}$ is the identity and H is a smoothing operator, normally the

gradient or the Laplacian of the solution. The constrained problem defined by equations (5.1a–c) is composed by the misfit minimization condition (5.1a), while (5.1b) is the bound to the *a priori* model \mathbf{m}_0 , and (5.1c) is the requirement for a smooth solution, which translates into minimizing the model's gradient or Laplacian. These constraints are weighted by the parameters λ and γ . The least-squares solution to this problem will be given by

$$\mathbf{m} = (G^T G + \gamma^2 \mathbf{1} + \lambda^2 H^T H)^{-1} (G^T \mathbf{d}_{\text{obs}} + \gamma^2 \mathbf{m}_0). \quad (5.2)$$

Bayesian approach

Equation (5.2) is a particular case of the general Bayesian treatment of the inverse problem, which is based on the analysis of uncertainties and on the description of the *states of information* as probability densities (Tarantola 2005). This section will briefly present this kind of approach.

First of all, we need to represent the physical theory that relates the model \mathbf{m} and the observable quantities \mathbf{d} . This relation can be written in statistical terms as a conjunct probability density:

$$\Theta(\mathbf{d}, \mathbf{m}) = \theta(\mathbf{d}|\mathbf{m})\mu_M(\mathbf{m})$$

where $\theta(\mathbf{d}|\mathbf{m})$ is the conditional probability density of finding the observables \mathbf{d} given the model \mathbf{m} , while $\mu_M(\mathbf{m})$ is the probability density of having the model \mathbf{m} in the model space M .

The *a priori* probability density on the space $D \times M$ is chosen in the form

$$\rho(\mathbf{d}, \mathbf{m}) = \rho_D(\mathbf{d})\rho_M(\mathbf{m}),$$

which means that the observables and the model's parameter are obtained independently from the D and M spaces respectively. The two states are combined to construct the *a posteriori* probability density function

$$\sigma(\mathbf{d}, \mathbf{m}) = k \frac{\rho(\mathbf{d}, \mathbf{m})\Theta(\mathbf{d}, \mathbf{m})}{\mu_D(\mathbf{d})\mu_M(\mathbf{m})} = k \frac{\rho(\mathbf{d}, \mathbf{m})\Theta(\mathbf{d}, \mathbf{m})}{\mu(\mathbf{d}, \mathbf{m})}$$

where $\mu(\mathbf{d}, \mathbf{m})$ is the homogeneous probability density function and k is a normalization coefficient. The information on the models space is then given

by marginal probability density

$$\sigma_M(\mathbf{m}) = \int_D \sigma(\mathbf{d}, \mathbf{m}) = k\rho(\mathbf{m}) \int_D \frac{\rho(\mathbf{d})\theta(\mathbf{d}|\mathbf{m})}{\mu_D(\mathbf{d})}.$$

The same applies on the observables space, but the integration has to be done over M . This equation can be written as

$$\sigma_M(\mathbf{m}) = k\rho(\mathbf{m})L(\mathbf{m})$$

where L is a likelihood function which measures how well \mathbf{m} is able to describe the observed data.

If we assume the uncertainties on the data \mathbf{d} and on the a priori model \mathbf{m} to be gaussian, then the *a posteriori* probability function will be gaussian too, with mean

$$\langle \mathbf{m} \rangle = (G^T C_D^{-1} G + C_M^{-1})^{-1} (G^T C_D^{-1} \mathbf{d}_{\text{obs}} + C_M^{-1} \mathbf{m}_0), \quad (5.3)$$

where C_M and C_D are covariance matrices. If the error on the data is not correlated, then the covariance matrices is simply the variance times the identity matrix:

$$C_D = \sigma_d^2 \mathbf{1}, \quad C_M = \sigma_m^2 \mathbf{1}. \quad (5.4)$$

By substituting [equation \(5.4\)](#) in [equation \(5.3\)](#) we find an expression which is equivalent to the least-squares solution [\(5.2\)](#).

5.2 Tomographic inversion

Selecting good measurements

Even the limited number of seismic stations available in Antarctica brings a high number of cross-correlations and hence to a high number of velocity measurements. A fraction of these measurement are not actually usable, as they carry no physical meaning. This may happen for several reasons: the geographical position and distance between the stations, the quality of the site, the capabilities of the instrumentation, local noise sources, and others.

We need a method to automatically identify good data points within

our period-velocity dataset, at least for a first, coarse-grained data quality assessment. This has been accomplished by binning all the available velocity measurement in a 2D histogram (figure 5.1), and by rejecting data points that are not within some statistical parameters. The rejected measurements are those who fall in bins which are scarcely populated; more precisely whose population puts them outside of the 85th percentile of the totality of the bins. By applying this condition outliers are rejected, and we are left with measurements which lie in a physically meaningful band, as figure 5.2 shows.

The shape of the populated region of figure 5.2 is worth a comment. The fact that the measurements band is broader for shorter periods ($T \lesssim 50$ s) is expected: as explained in chapter 3 shorter periods are sensitive to shallower features of the crust, which is more variable, especially in West Antarctica. On the contrary, longer periods are associated with greater depths, where the crust is more uniform, which explains the narrower spread of measurements for $T \gtrsim 50$ s. This different period-dependent dispersion of the measurement means that other statistical parameters (for example, mean and standard deviation computed over the entire set of measurements) are not good candidates to identify and eliminate the outliers.

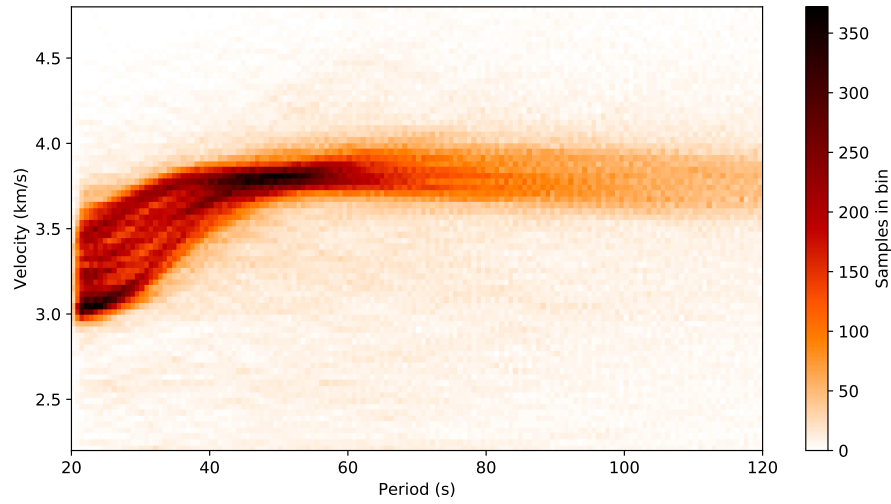


Figure 5.1 Velocity measurements binning without any cut applied. A highly populated band of measurement is visible along with several outliers.

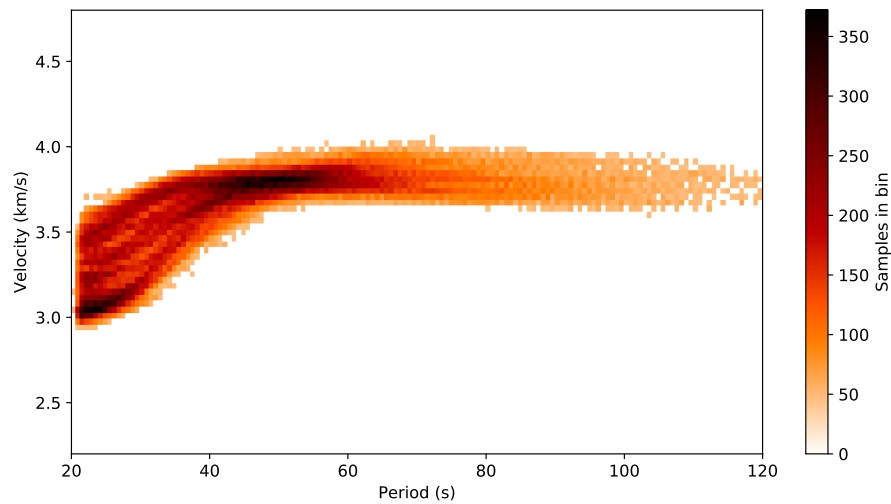


Figure 5.2 Velocity measurements binning where the outliers have been removed.

Parametrization

The inversion is done by dividing the region of interest in discrete cells and by computing the quantities of interest within each cell, a process that is called *parametrization*. There are several ways to parametrize the problem, here what I used is a grid constructed on a “cubed sphere” (figure 5.3), a gridding technique for the solution of partial differential equations in spherical geometry (Ronchi, Iacono, and Paolucci 1996), akin to what has been done in (Schivardi and Morelli 2009, 2011).

This parametrization is built starting from the cube inscribed in the Earth, neglecting the planet’s ellipticity. The cube is oriented so one of its faces is centered on the South pole. The twelve edges of the cube are projected onto the Earth surface; each face projected on the sphere is then divided into a grid of squared cells (pixels) of approximate size of 83 km × 83 km and identified by their median point. A trigonometric correction to minimize the cell stretching near the angles is applied. I used the linearized ray theory, where lateral velocity anomalies are small enough not to deviate the ray from its path in a reference laterally homogeneous model, and neglected second-order effects such as azimuthal anisotropy, scattering, finite frequency effects, and multipathing. This allows to assume that seismic waves propagate along the great-circle arc that connects the receivers. A separate linear inverse problem has been set up for each period and solved it to obtain two-dimensional group velocity maps of the studied region. For each ray j the total traveltime t_j is expressed as the sum of the traveltime t_0 (corresponding to the ray in the reference laterally homogeneous model PREM) plus a perturbation δt_i due to the local perturbation in slowness. For each ray, the partial derivatives for the slowness inversion in a pixel are simply the length of the ray lying within the pixel.

The inversion code has been run on the velocity data set built as explained in the previous paragraph, leading to the data necessary to finally plot the surface wave velocity maps.

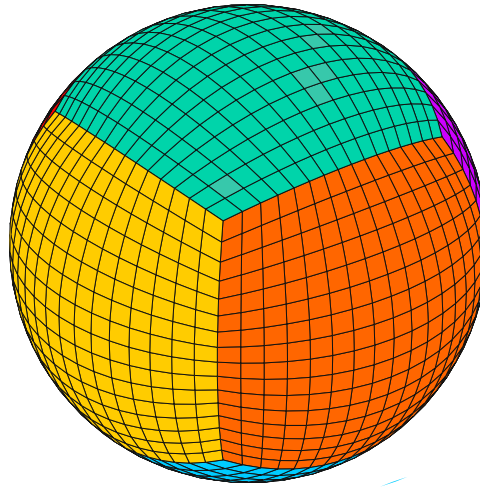


Figure 5.3 A 3D view of the tiling of the cubed sphere used for the inversion. In the actual run each face has been divided in 120×120 pixels.

5.3 Velocity maps and profiles

Rayleigh group velocity maps

Seismic tomographic problems are generally over-determined (i.e., there is some redundancy of data, that we require to fit only within their errors) but — more critically — under-determined (i.e., there is not enough information to uniquely determine a solution). As a consequence, we need to add some *a priori* information to constrain the solution. *A priori* information explicitly enters into the solution as shown by equation (5.3). In our case, it is legitimate to impose some lateral “smoothness”, as we do not expect dispersion maps to be rough for structure in nature. Legitimate *a priori* information consists then of a reference model, from which the inversion result should not differ greatly, and some condition on smoothness. A condition on smoothness could be implemented on the expected correlation of model values among near points, as a limitation on horizontal gradient, or as a condition in the model’s curvature through the computation of the model’s Laplacian. A similar approach has been used by Schivardi and Morelli (2009).

Tomographic inversion is the only way to look into the geographical coherence of measurements. Therefore, as a first step I have done an inversion with minimal constraints, accepting any roughness deriving from the data.

This perhaps will not be a plausible representation of the real model, but will be a useful test for the outcome of the measurements. Also, the model grid representation will be obvious in such images, but the goal of the inversion is diagnostic, rather than to provide an acceptable representation of true structure.

As ray theory is used to compute the dependence of group arrival times on structure, sensitivity to individual measurements will be concentrated along narrow paths between stations. An a priori condition, that keeps the inversion result tied to the reference, laterally homogeneous, model is needed in order to find a solution. This condition will constrain the inversion result to the reference model where there are no rays, for this reason we expect to see ray paths. This is, again, a good test to get a feeling of the information contained in the data.

Figures 5.4 and 5.7 show this “raw” model for two sample periods of 30 s and 80 s. These two periods have been chosen to look at because they are roughly representative of crustal and upper mantle structure. This derives from the sensitivity kernels (figure 3.5): sensitivity of group velocity of Rayleigh waves at 30 s is peaked at approximately 40 km, while sensitivity at 80 s reaches maximum at about 80 km.

Figure 5.4 shows that measurements indicate variations of group velocity of $\pm 15\%$, a value expected from previous earthquake-based studies (e.g. Danesi and Morelli 2000). This is due to a shallower crust in West Antarctica, so that waves are also sensitive to higher mantle v_S velocity. On the other hand, the thick crust in East Antarctica is such that sensitivity does not reach the mantle (figure 3.5), so group velocity is entirely determined by v_S in the crust. These results, entirely based on ambient noise, agree very well with results obtained from earthquake-based tomography (e.g. Danesi and Morelli 2000). It is interesting to note that the few ray paths that cross oceanic crust (at low latitude, longitude between -60° and 0° are also faster.

Figure 5.5 shows the similar result, for $T = 80$ s. There are fewer ray paths here, because measurements based on noise become more difficult at longer periods. Here, the color pattern is switched: now we have a faster East Antarctica and a slower West. This, again, compares well with previous results (e.g. Danesi and Morelli 2000) and is easily understandable on the

basis of sensitivity kernels of [figure 3.5](#). East Antarctica is a stable, cold and thick craton, while West Antarctica is seat of active tectonics, spreading, and volcanism (a picture compatible with relatively low velocity).

This model can be smoothed by applying a Laplacian damping condition. The Laplacian has been implemented numerically through a finite-difference moving stencil to calculate second derivatives. This will produce a better looking result, with one caveat: without anchoring the solution to an a priori model the smoothing operation will bring to extrapolated values of the model in the area which is outside of the polygon delimited by the seismic stations. This extrapolation is likely to be divergent. [Figures 5.6](#) and [5.7](#) show the smoothed model, cropped at the coast of the continent.

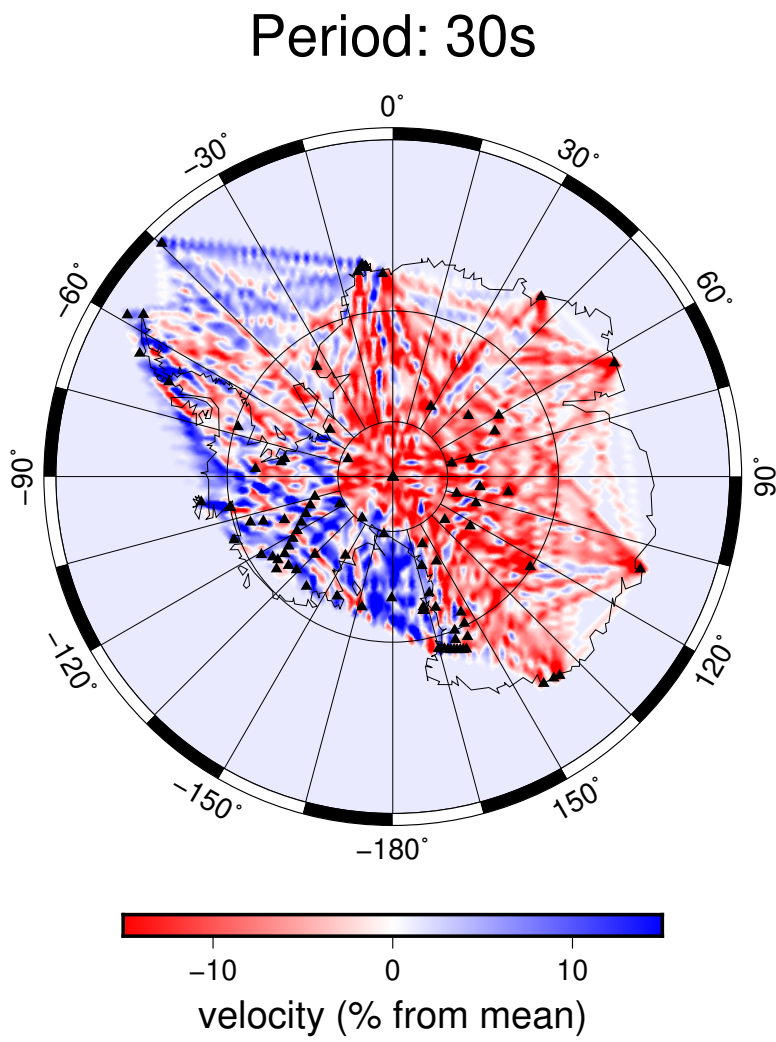


Figure 5.4 Rays for $T = 30$ s.

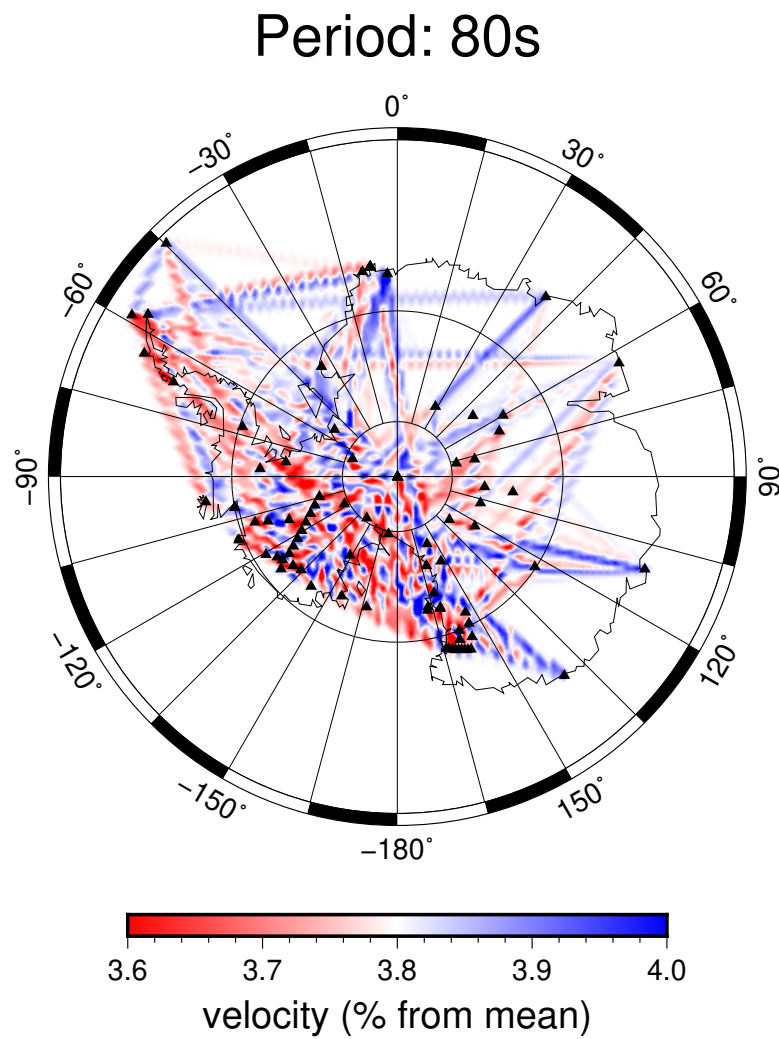


Figure 5.5 Raw model: rays for $T = 80$ s.

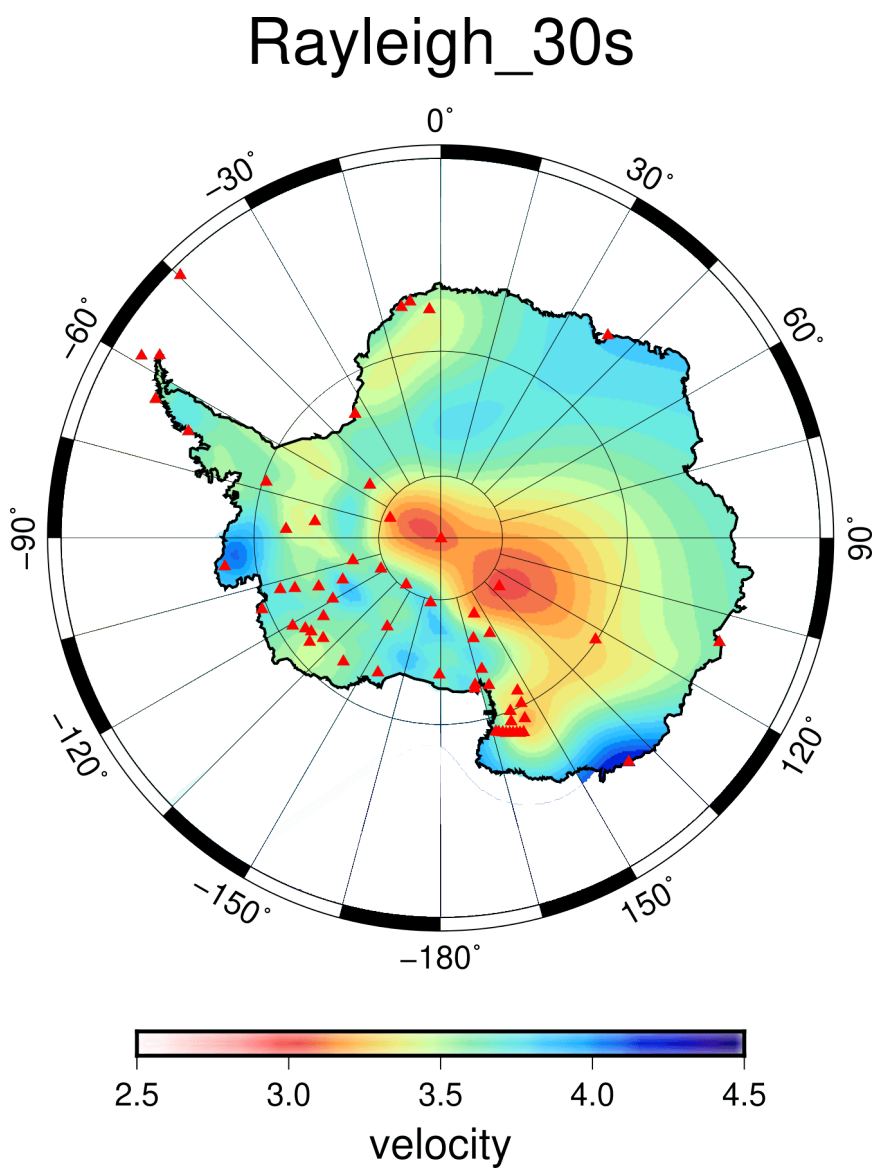


Figure 5.6 Group velocity (km/s) map for 30 s Rayleigh waves.

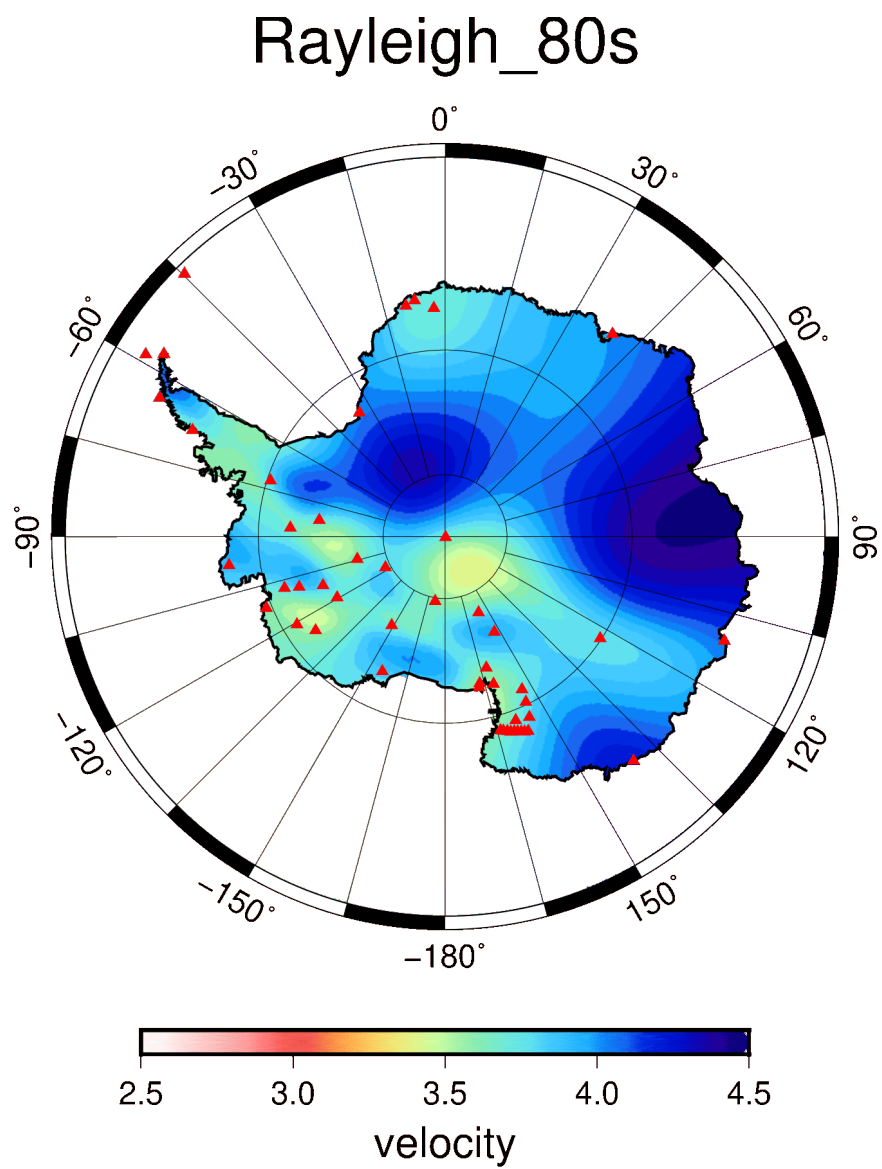


Figure 5.7 Group velocity (km/s) map for 80 s Rayleigh waves.

Average 1D v_S profiles

Antarctica is made by two main tectonically distinct regions, West Antarctica and East Antarctica, as explained in [chapter 1](#). This means that we do expect some major differences in the average 1D profiles for v_S in these two regions, especially for the shorter periods. I already commented on the dispersion curve distribution shown in [figure 5.2](#), and on the fact that the range of measured velocities is broader for $T \lesssim 50$ s, as shorter periods are sensitive to shallower features of the crust, which are more variable. On the contrary, longer periods are associated with greater depths ([figure 3.6](#)), where the mantle is more uniform, which explains the narrower spread of measurements for $T \gtrsim 50$ s.

[Figures 5.8](#) and [5.9](#) have been constructed with the same technique used for [figure 5.2](#), but selecting only the rays entirely contained in West and East Antarctica, respectively. The different velocities around which the measurements cluster is apparent. The two average dispersion curves are represented in a single graph in [figures 5.10](#) and [5.11](#). The crossing of the curves is expected. Rayleigh waves with a period shorter than 40 s are highly sensitive to crustal depth, and for this reason higher velocities are expected in West Antarctica, due to its thinner and unstable structure, while lower velocities are expected for the thick cratonic crust of East Antarctica. The opposite is true per periods longer than 50 s, which are sensitive to the structure of the upper mantle: in this case the thin continental crust of West Antarctica is expected to show lower velocities.

A preliminary 1D inversion for v_S has been computed from these average curves using the Monte Carlo neighborhood sampling algorithm (Wathelet 2008) implemented in the Geopsy software package ([Geopsy project 2019](#)). The inversion is based on a very simple reference model and neglects the mantle's anisotropy; its purpose is to serve as a qualitative comparison between the different crustal thickness in West and East Antarctica and the associated difference in v_S . The best fitting inverted profiles are shown in [figure 5.12](#), the difference in crustal thickness and in v_S at different depths in the two halves of the continent is apparent. However simple, these average v_S profiles compare well to the sample v_S profiles for West and East Antarctica shown in (An et al. 2015).

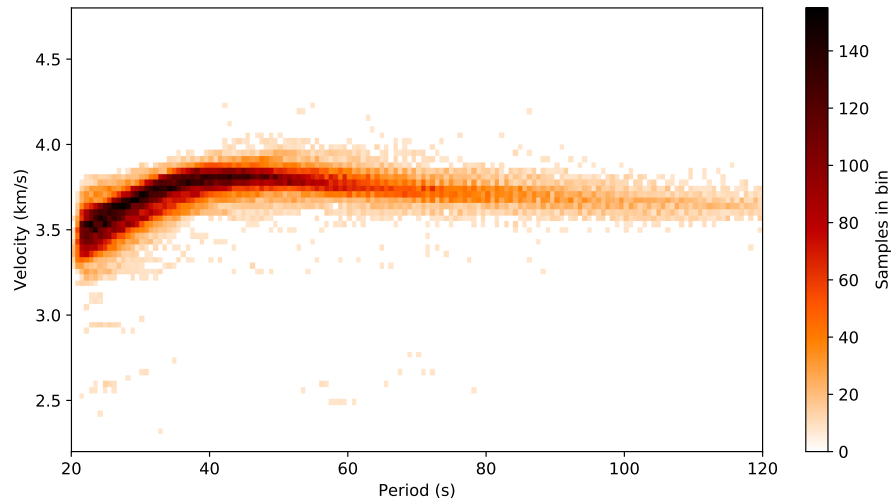


Figure 5.8 Velocity measurements binning for rays entirely in West Antarctica. Note that for $T \approx 20$ s most of the dispersion curves show a velocity of about 3.5 km/s. Compare with [figure 5.9](#).

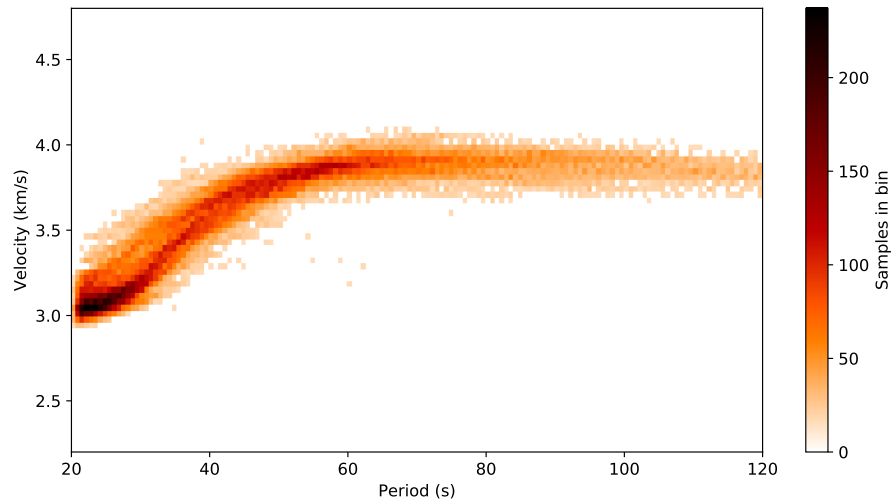


Figure 5.9 Velocity measurements binning for rays entirely in West Antarctica. Note that for $T \approx 20$ s most of the dispersion curves show a velocity of about 3 km/s. Compare with [figure 5.8](#).

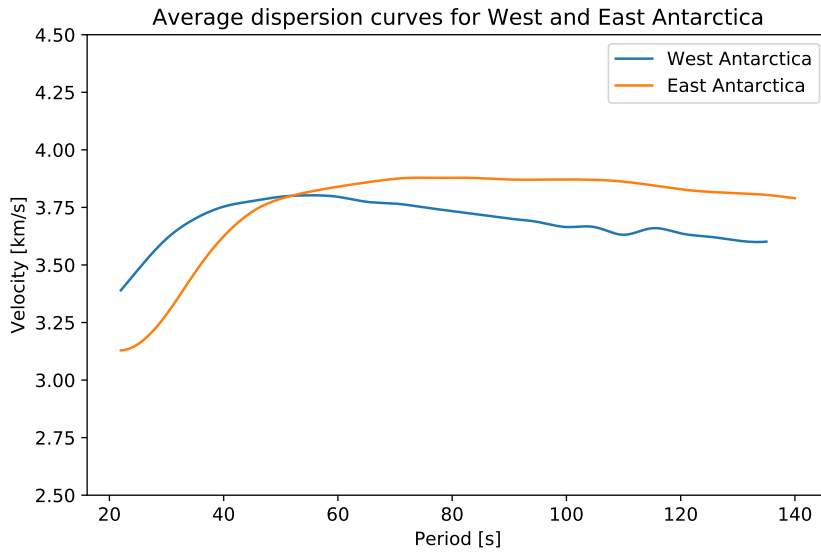


Figure 5.10 The average dispersion curves for West and East Antarctica (velocity in function of period).

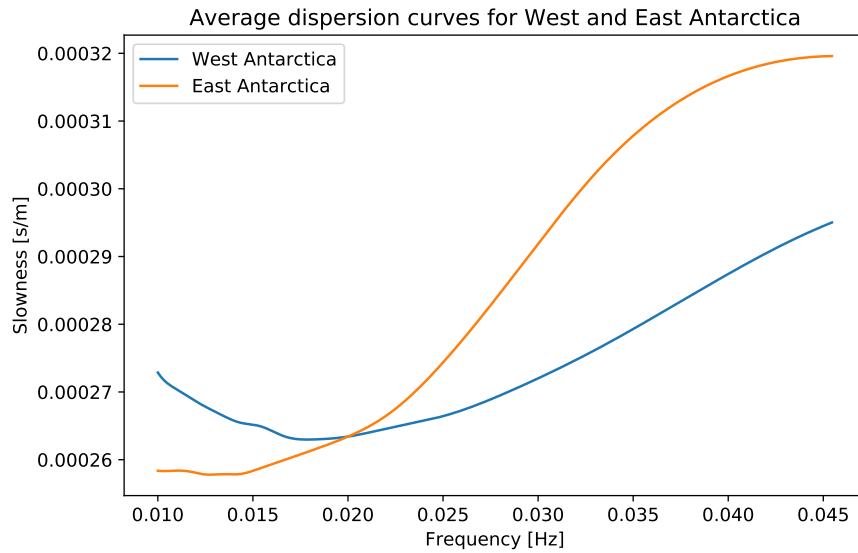


Figure 5.11 The average dispersion curves for West and East Antarctica (slowness in function of frequency).

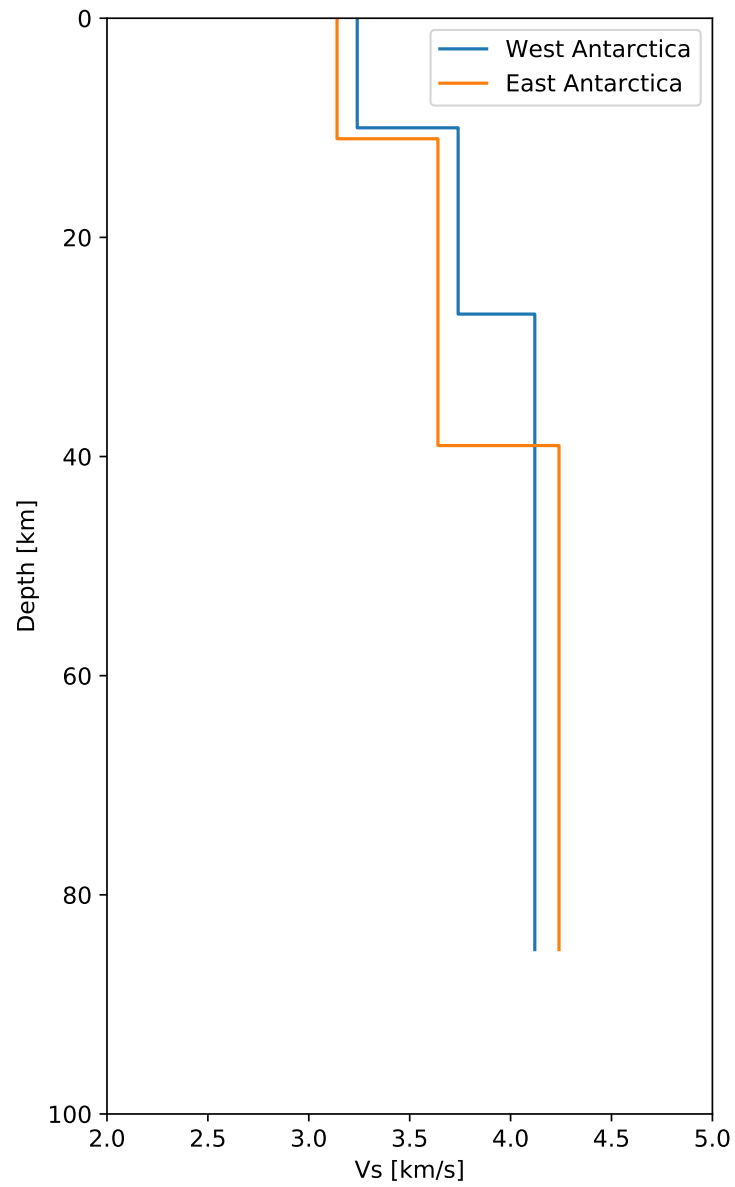


Figure 5.12 Preliminary v_s profiles for the average dispersion curves of West and East Antarctica.

Discussion

Using only seismic ambient noise, I have produced tomographic solutions comparable to those obtained using earthquake data. This is an encouraging result, and shows that indeed ambient noise tomography is a tool with universal application. Ambient noise tomography has mostly been used on continental arrays with relatively local aperture, and centered with measurements in period bands, say, between 6 to 12 seconds — where ocean-generated microseismic signal has higher amplitude. Longer-period, and larger-scale, studies do exist, e.g. Nishida, Montagner, and Kawakatsu (2009) and Lu et al. (2018), reaching 120 s in the whole European region, but are not common. Haned et al. (2016) have shown that ambient noise tomography can also be applied at global scale using only very-long period data but broad-band, continental-scale studies are not common. I have obtained excellent results that compare very well to earthquake-based studies.

Ambient noise tomography shows to be an appropriate tool to study Antarctic continental structure. In East Antarctica, however, the small number of stations limits the resolution of the model obtainable. To this extent, I can notice that ambient noise tomography only builds on inter-station paths, hence it is sensitive to the number of stations, while earthquake-based tomography can attain more diffuse path coverage due to the fact that earthquake epicenters are more spread in space. Specifically, one single station in Antarctica can record earthquakes distributed along the oceanic ridges encircling the plate. I may therefore point out that, in order to obtain the maximum resolution possible, it may be advantageous to combine measurements taken on noise interferograms, with those taken on earthquake wave packets. This integration may be the topic for further study.

On the other hand, I can point out that a major advantage of ambient noise tomography for continental studies consists in its sensitivity being limited to the region between stations, hence its results are not contaminated by oceanic structure.

Chapter 6

Conclusions

In this thesis, I constructed a tomographic model of the Antarctic continent analysing seismic ambient noise recorded by permanent and temporary stations. Seismic ambient noise is becoming a rather common tool for imaging Earth structure, and many studies are showing its potential. To compute interferograms between stations, I used phase cross-correlation (Schimmel, Stutzmann, and Gallart 2011; Schimmel 1999), rather than the more common linear cross-correlation used by most authors. Phase cross-correlation is based on correlation of the instantaneous phase of the analytical signal associated to a seismogram (calculated adding the Hilbert transform as imaginary part), and by being constructed on instantaneous phase only, is quite insensitive to local disturbances. In my application, the phase cross-correlation (complemented by a phase weighted stack) produced much cleaner seismograms than linear cross-correlation. I was able to often detect some cyclic seasonal variation in the convergence rate of the stacked correlations to a final dispersion curve, but this is not a general feature and its reason is still unexplained. One can hypothesize that the generally better winter conditions are due to more clear signal, caused by ocean storms, while worse summer conditions are connected to larger local disturbances due to atmospheric effects.

Figures 5.6 and 5.7 show the result of this work: the group velocity models for the fundamental mode Rayleigh waves for periods of 30 s and 80 s. The two maps use a color scale to represent the deviations of the group velocity from the regional average values, which has been computed from

the whole dataset.

In order to give an interpretation to the model we will take the sensitivity kernels for PREM of [figure 3.5](#) as a reference. At a period of 30 s Rayleigh waves are sensitive to the crustal depth. The distinction between the older and stable cratonic crust of East Antarctica and thinner and more active structure of West Antarctica we mentioned in [chapter 1](#) is clearly visible. In [figure 5.6](#) the positive and negative velocity anomalies coincide with the oceanic and continental domains. Shifting to the 80 s period the pattern is almost inverted, showing a relevant negative anomaly locates in the Ross Sea region. This is in agreement with the lithosphere thickness models, which implies that at 80 km (where the peak of the $T = 80$ s sensitivity kernel is located) East Antarctic is still in the high-velocity lithospheric upper mantle (An et al. 2015). These results are in good accordance with previous regional models (An et al. 2015; Danesi and Morelli 2000, 2001; Morelli and Danesi 2004).

These models are promising and have been obtained with techniques that, to the best of my knowledge, were not applied before to Antarctic data, however some work still has to be done in order to improve on the state of the art. The resolution of the model can be improved a finer parametrization grid. Given that the model is constructed using only cross-correlation, it is actually a polygon delimited by pairs of seismic stations; what is outside of this polygon is extrapolated and this operation can be unstable. This is not optimal, and the model could be constrained to a known *a priori* model in the regions that have no rays. This could be done with a global model like (Schaeffer and Lebedev 2013), or with a regional model like AN1-S (An et al. 2016), which is based on An et al. (2015). An average oceanic crust model could be used where appropriate. Techniques on how to constrain a problem to some *a priori* conditions have been described in [section 5.1](#) and are treated extensively in (Tarantola 2005).

Finally, an inversion for v_s has to be performed in order to construct a three dimensional model of the continent. This could be done using the iterative linearized least squares inversion method implemented in the Computer Programs in Seismology (Herrmann 2013).

Appendix A

Hermes: technical documentation

Configurazione del sistema Hermes

Paride Legovini
paride.legovini@ingv.it

Indice

1	Obiettivi e scelte tecniche	2
2	Funzionamento	2
3	Requisiti per l'installazione	3
	Pacchetti necessari	3
	Solo per CentOS: aggiunta del repository EPEL	3
	Installazione di incron	4
	Installazione di rssh	4
4	Configurazione di Hermes	4
	Installazione dello script	4
	Creazione gruppi e directory di base	4
5	Come aggiungere un utente	5
	Sul server in Italia	5
	Sul server a Concordia	5
	Limitare l'accesso con rssh	5
	Prove di funzionamento	5
	Rimuovere un utente	6
6	Trasferire i dati nel server in Antartide	6
	Funzionamento manuale	6
	Trasferimento automatico	6
7	Limitazione della banda	7
8	Sorgenti degli script	7

1 Obiettivi e scelte tecniche

Il sistema Hermes (High Efficiency Relay of Mission Experiments data Sharing) nasce dall'esigenza di trasferire i dati scientifici generati presso la stazione Concordia verso l'Europa, in modo da renderli disponibili ai gruppi di ricerca interessati. Un sistema dedicato è reso necessario dalla limitata connettività di cui dispongono le stazioni antartiche. Nel caso di Concordia si tratta di un link satellitare a 512 kbit/s a cui si affidano tutti i servizi della base. Il collegamento non è per sua natura stabile, inoltre la latenza è molto alta (spesso arriva a diversi secondi).

L'idea di base è quella di centralizzare il trasferimento dati, installando una coppia di server, uno in Italia e uno in Antartide. Il sistema Hermes si occupa di trasferire i dati dal server in Antartide a quello in Italia in modo automatico e affidabile, minimizzando la banda utilizzata. Una prima implementazione del sistema è stata fatta da Antonio Litterio durante la scorsa campagna invernale, io l'ho successivamente modificato per renderlo più stabile e semplice.

Per via delle limitazioni di banda il sistema Hermes dovrà avere almeno le seguenti caratteristiche:

- i Essere in grado di riprendere i trasferimenti interrotti, così da non sprecare banda durante le frequenti interruzioni;
- ii Evitare per quanto possibile di ritrasferire gli stessi dati, a prescindere dalle operazioni svolte dagli utenti sui server;
- iii Comprimere il più possibile i dati, senza "fidarsi" che gli utenti l'abbiano già fatto.

e questo è stato implementato tenendo in mente alcune scelte tecniche:

- iv Uso di tool standard presenti in tutti i sistemi GNU/Linux, in modo che il sistema sia implementabile a prescindere dalla particolare distribuzione installata;
- v Avvio automatico del trasferimento dati nel momento in cui questi vengono caricati sul server in Antartide, *evitando fare polling*;
- vi Sicurezza: l'autenticazione tra i due server deve avvenire tramite un sistema a chiave pubblica, evitando l'uso di password in chiaro;
- vii Confidenzialità: tutti i dati viaggiano crittografati.

2 Funzionamento

Il funzionamento di base del sistema è il seguente:

1. Ogni progetto ha un utente sul server a Concordia. I dati da trasferire vanno messi nella directory `~/from_dmc` (al solito `~` rappresenta la home directory dell'utente). I dati possono venire copiati nel server usando i protocolli standard: `sftp`, `scp`, `rsync`. L'accesso alla shell via `ssh` è interdetto tramite l'uso di `rssh`¹.

¹<http://www.pizzashack.org/rssh/>

2. Quando viene aggiunto un file da copiare lo script principale di Hermes viene lanciato automaticamente per l'utente interessato. Questa funzionalità è implementata usando l'interfaccia inotify del kernel e il servizio incron (INotify Cron), in modo da evitare di fare polling su ~/from_dmc.
3. Lo script Hermes attende un tempo predeterminato (breve) e lancia un rsync con il server installato in Italia. Su questo server dovrà dunque esistere un utente con lo stesso username e a cui l'utente sul server hermes possa accedere in modo automatico, senza che venga richiesta una password. L'autenticazione avviene tramite chiave pubblica. Rsync provvede alla compressione dei dati e alla continuazione di eventuali upload interrotti, facendo un checksum delle parti già trasferite.
4. Lo script ha un ciclo che continua a lanciare rsync fino a che tutti i dati sono stati trasferiti, al che i dati vengono cancellati dal server a Concordia.
5. Il sistema torna in stato di attesa.

3 Requisiti per l'installazione

Pacchetti necessari

Sul lato italiano si necessita di un server con installati ssh e rsync. Sono pacchetti presenti di default in ogni distribuzione.

Sul lato Concordia devono essere installati: ssh, rsync e incron. Il pacchetto incron lancia comandi in corrispondenza di modifiche del filesystem utilizzando l'interfaccia inotify del kernel², la quale genera eventi in corrispondenza di modifiche al filesystem.

Se si vuole impedire che gli utenti abbiano accesso ssh ai server (cosa fortemente consigliata) è necessario installare anche il pacchetto rssh (ReSTricted SHell).

Solo per CentOS: aggiunta del repository EPEL

Per installare rssh e incron su CentOS è necessario aggiungere il repository EPEL (Extra Packages for Enterprise Linux)³. Al momento rssh e incron sono disponibili solo per CentOS 6, ma è probabile che vengano presto aggiunti anche per CentOS 7.

Per aggiungere il repository EPEL a CentOS 6 (64 bit) dare da root i comandi:

- 1 `wget http://download.fedoraproject.org/pub/epel/6/x86_64/epel-release-6-8.noarch.rpm`
- 2 `rpm -ivh epel-release-6-8.noarch.rpm`

Verificare poi che il repository sia abilitato con `yum repolist`.

²Vedi <https://en.wikipedia.org/wiki/Inotify>.

³Vedi <https://fedoraproject.org/wiki/EPEL>.

Installazione di incron

In CentOS il pacchetto si installa normalmente con yum dopo aver abilitato il repository EPEL. In Debian (*wheezy* e successive) il pacchetto è nei repository ufficiali e si installa normalmente con apt-get (o aptitude).

Di default incron funziona solo per l'utente root. Per abilitare tutti gli utenti all'uso di incron si deve cancellare il file /etc/incron.allow (se presente):

```
rm -f /etc/incron.allow
```

Installazione di rssh

Rssh è una shell che di fatto limita l'utente all'uso di alcuni protocolli di trasferimento dati. In questo modo è possibile usare la semplice e potente autenticazione SSH senza dare agli utenti accesso alla linea di comando.

In CentOS il pacchetto si installa normalmente con yum dopo aver abilitato il repository EPEL. In Debian (*wheezy* e successive) il pacchetto è nei repository ufficiali e si installa normalmente con apt-get (o aptitude).

Una volta installato il pacchetto si tratta di decidere quali protocolli sono abilitati. In /etc/rssh.conf decommentare i protocolli che si vogliono abilitare, per esempio:

```
1 allowscp
2 allowsftp
3 #allowcvs
4 #allowrdist
5 allowrsync
6 #allowsvsserve
```

La configurazione di rssh è completa.

4 Configurazione di Hermes

Installazione dello script

Tutto quello che segue va eseguito con i privilegi di root. Per prima cosa lo script hermes_rsync_new.sh va copiato in /usr/local/bin/ nel server a Concordia e gli vanno dati i permessi di esecuzione:

```
chmod +x /usr/local/bin/hermes_rsync_new.sh
```

Lo script è leggibile e commentato, consiglio di leggerlo, anche per capire quali sono i parametri modificabili. In particolare all'interno dello script è impostato l'hostname del server Hermes italiano; questo va modificato nel caso sia diverso da hermes.enea.pnra.it.

Creazione gruppi e directory di base

Vogliamo che gli utenti dei progetti facciano parte del gruppo projects e che le home directory si trovino in /home/projects/, in modo da facilitare la gestione del sistema. Su entrambi i server diamo quindi i comandi:

```
1 groupadd projects
2 mkdir /home/projects
```

5 Come aggiungere un utente

Aggiungiamo ora un utente chiamato prova, seguendo la procedura passo passo.

Sul server in Italia

Da root eseguire:

```
1 NEWUSER=prova
2 useradd -b /home/projects -g projects -m -K UMASK=077 $NEWUSER
3 passwd $NEWUSER # Settare la password dell'utente (lato Italia)
4 sudo -u $NEWUSER mkdir /home/projects/$NEWUSER/.ssh
```

Sul server a Concordia

In questo esempio supporremo che il server italiano abbia indirizzo hermes.enea.pnra.it. Lo script hermes_rsync_new.sh contiene esplicitamente questo indirizzo, se necessario va modificato opportunamente.

Da root eseguire:

```
1 NEWUSER=prova
2 useradd -b /home/projects -g projects -m -K UMASK=077 $NEWUSER
3 passwd $NEWUSER # Settare la password dell'utente (lato Concordia)
4 sudo -u $NEWUSER mkdir /home/projects/$NEWUSER/from_dmc
5 sudo -u $NEWUSER ssh-keygen -t rsa -N "" -f /home/projects/$NEWUSER/.ssh/id_rsa
6 sudo -u $NEWUSER ssh-copy-id hermes.enea.pnra.it
```

al che verrà richiesta la password impostata sul server italiano. Dare poi il comando

```
incrontab -e -u $NEWUSER
```

si aprirà un editor (come avviene con il “solito” crontab -e). Aggiungere la linea

```
/home/projects/prova/from_dmc IN_MODIFY,IN_CREATE,IN_NO_LOOP /usr/local/bin/hermes_rsync_new.sh
```

e salvare. Il percorso da monitorare (nell'esempio /home/projects/prova/from_dmc deve essere assoluto e va naturalmente modificato per un utente diverso da prova.

Limitare l'accesso con rssh

Dopo avere aggiunto l'utente come spiegato sopra eseguire su entrambi i server e da root:

```
chsh -s /usr/bin/rssh prova
```

Prove di funzionamento

Per provare se tutto è in ordine basta copiare un file nella directory from_dmc dell'utente prova. Questo può essere fatto per esempio con sftp, o con uno qualsiasi dei protocollo abilitati da rssh. Ci aspettiamo che:

1. Il file venga trasferito sul server italiano;

2. Il file venga cancellato dal server a Concordia;
3. Il log del trasferimento venga salvato nel file `~/hermes/rsync.log`, insieme a tutti i dettagli (dimensione dei file, eventuali interruzioni...).

Rimuovere un utente

Su entrambi i server dare da root: `userdel -r <nomeutente>`.

6 Trasferire i dati nel server in Antartide

Funzionamento manuale

Per trasferire manualmente i file dai computer scientifici al server Hermes basta usare un qualsiasi client che supporti i protocolli SCP o SFTP.

Se il sistema è Linux si possono usare i comandi standard `scp`, `sftp` ed `rsync`. Se invece il sistema è Windows si può usare FileZilla⁴ (client grafico) o WinSCP⁵ (client sia grafico che testuale).

I file da trasferire vannu naturalmente messi nella cartella `from_dmc`.

Trasferimento automatico

Se il sistema è Linux la cosa migliore è configurare l'autenticazione SSH tramite chiave pubblica e lanciare un `scp` (o `rsync`) periodico che copi i dati che si vogliono trasferire in `from_dmc`. Una soluzione meno raffinata ma funzionante e accettabile nel contesto "protetto" di Concordia consiste nell'usare l'utility `sshpass`, la cui sintassi è banale.

Su sistemi Windows si può installare l'ambiente `cygwin` e risolvere il problema allo stesso modo in cui lo si fa su Linux. In alternativa si può usare il client testuale di WinSCP (`winscp.com`), che ha un suo linguaggio di scripting che permette di automatizzare tutte le operazioni. Il comando può essere inserito in un file batch da richiamare attraverso le "operazioni pianificate" di Windows. Uno script di `winscp` per esempio può essere:

```

1 # Termina in caso di errori
2 option batch abort
3 # Sovrascrivi senza chiedere
4 option confirm off
5 # Connettiti al server
6 open sftp://username:password@hermes2.concordiastation.aq
7 # Upload dei file
8 cd from_dmc
9 put c:\data\file1.dat
10 put c:\data\file2.dat
11 # Disconnetti
12 close

```

⁴<http://filezilla.net/>

⁵<http://winscp.net/>

Se il file contenente questo script si chiama `hermes.txt`, il comando da lanciare per trasferire i dati è:

```
winscp.com /script=hermes.txt
```

Sul sito <http://winscp.net/> è disponibile molta documentazione ben fatta, l'esempio precedente è preso da http://winscp.net/eng/docs/guide_automation.

7 Limitazione della banda

Se lo si desidera è possibile limitare la banda in uscita verso il server Hermes italiano usando le funzioni di Traffic Control offerte dal kernel Linux. Di questo si occupa lo script `hermes_shaping.sh`, che prende come unico argomento la banda massima a disposizione verso l'indirizzo IP del server Hermes italiano. Se l'indirizzo dovesse cambiare lo script andrà dunque modificato. Un esempio di utilizzo:

```
/usr/local/bin/hermes_shaping.sh 256kbit
```

da eseguire con i privilegi di root.

Questo script è specialmente utile se chiamato periodicamente dalla crontab dell'utente root, per esempio come segue:

```
1 # m h dom mon dow  command
2
3 MAILTO=""
4
5 @reboot /usr/local/bin/hermes_shaping.sh 128kbit
6 0 0 * * * /usr/local/bin/hermes_shaping.sh 400kbit
7 0 7 * * * /usr/local/bin/hermes_shaping.sh 128kbit
```

Queste impostazioni fanno sì che alle 00:00 la banda disponibile per Hermes sia limitata a 400 kbit/s, mentre alle 07:00 questa venga ulteriormente ristretta a 128 kbit/s. La linea che inizia con `@reboot` imposta un limite prudente quando il sistema viene avviato. Per modificare la crontab si usa il comando `crontab -e`. Bisogna ricordare che cron usa sempre il fuso orario di sistema.

È bene che anche durante il giorno ci sia una piccola parte di banda a disposizione di Hermes, così chi ha bisogno di trasferire file piccoli non deve aspettare la notte per riceverli. Questo è utile per esempio nel caso della telemetria.

8 Sorgenti degli script

Omessi.

Bibliography

- Adams, R. D. (1982). Source Properties of the Oates Land Earthquake. *Antarctic Geoscience*, 955–958.
- Adams, R. D., A. A. Hughes, and B. M. Zhang (1985). A confirmed earthquake in continental Antarctica. *Geophysical Journal International* 81(2), 489–492. DOI: [10.1111/j.1365-246x.1985.tb06416.x](https://doi.org/10.1111/j.1365-246x.1985.tb06416.x) (cit. on p. 25).
- An, M., D. A. Wiens, Y. Zhao, M. Feng, A. A. Nyblade, M. Kanao, Y. Li, A. Maggi, and J.-J. L ev eque (2015). S-velocity model and inferred Moho topography beneath the Antarctic Plate from Rayleigh waves. *Journal of Geophysical Research: Solid Earth* 120(1), 359–383. DOI: [10.1002/2014jb011332](https://doi.org/10.1002/2014jb011332) (cit. on pp. 55, 67, 70, 113, 120, 129).
- An, Wiens, Zhao, Feng, Nyblade, Kanao, Li, Maggi, and L ev eque (2016). *Crust/Lithosphere model (AN1) of the Antarctic Plate*. URL: <http://www.seismolab.org/model/antarctica/lithosphere/index.html> (visited on 2019) (cit. on p. 120).
- Anandakrishnan, S. and D. Wiens (2000). A Broadband Seismic Investigation of Deep Continental Structure Across the East-West Antarctic Boundary. DOI: [10.7914/sn/xp_2000](https://doi.org/10.7914/sn/xp_2000) (cit. on p. 28).
- Anthony, R. E., R. C. Aster, D. Wiens, A. Nyblade, S. Anandakrishnan, A. Huerta, J. P. Winberry, T. Wilson, and C. Rowe (2014). The Seismic Noise Environment of Antarctica. *Seismological Research Letters* 86(1), 89–100. DOI: [10.1785/0220140109](https://doi.org/10.1785/0220140109) (cit. on p. 48).
- Baranov, A. and A. Morelli (2013). The Moho depth map of the Antarctica region. *Tectonophysics* 609, 299–313. DOI: [10.1016/j.tecto.2012.12.023](https://doi.org/10.1016/j.tecto.2012.12.023).
- Bayin, S. S. (2018). *Mathematical Methods in Science and Engineering*. 2nd ed. Wiley. ISBN: 978-1-119-42545-8 (cit. on pp. 47, 49).

- Bensen, G. D., M. H. Ritzwoller, M. P. Barmin, A. L. Levshin, F. Lin, M. P. Moschetti, N. M. Shapiro, and Y. Yang (2007). Processing seismic ambient noise data to obtain reliable broad-band surface wave dispersion measurements. *Geophysical Journal International* 169(3), 1239–1260. DOI: [10.1111/j.1365-246x.2007.03374.x](https://doi.org/10.1111/j.1365-246x.2007.03374.x) (cit. on p. 87).
- Beyreuther, M., R. Barsch, L. Krischer, T. Megies, Y. Behr, and J. Wassermann (2010). ObsPy: A Python Toolbox for Seismology. *Seismological Research Letters* 81(3), 530–533. DOI: [10.1785/gssrl.81.3.530](https://doi.org/10.1785/gssrl.81.3.530) (cit. on p. 76).
- Bonnefoy-Claudet, S., F. Cotton, and P.-Y. Bard (2006). The nature of noise wavefield and its applications for site effects studies. *Earth-Science Reviews* 79(3-4), 205–227. DOI: [10.1016/j.earscirev.2006.07.004](https://doi.org/10.1016/j.earscirev.2006.07.004) (cit. on p. 47).
- British Antarctic Survey (2018). *Antarctic Factsheet*. URL: <https://www.bas.ac.uk/science/science-and-society/education/antarctic-factsheet-geographical-statistics/> (visited on 10/20/2018) (cit. on p. 22).
- Chapman, W. L. and J. E. Walsh (2007). A Synthesis of Antarctic Temperatures. *Journal of Climate* 20(16), 4096–4117. DOI: [10.1175/jcli4236.1](https://doi.org/10.1175/jcli4236.1) (cit. on p. 22).
- Council of Managers of National Antarctic Programs (2018). *COMNAP Antarctic Facilities*. URL: <https://github.com/PolarGeospatialCenter/comnap-antarctic-facilities> (visited on 10/21/2018) (cit. on pp. 22, 24).
- Danecek, P., A. Delladio, D. Zigone, A. Cavaliere, P. Legovini, and D. Sorrentino (2018). Seismological Observatories in Antarctica: An Update on the Italian Program and the Evolution of the Observatories. Poster. Presented 36th General Assembly of the European Seismological Commission (ESC2018), Malta (MT) (cit. on p. 44).
- Danesi, S. and A. Morelli (2000). Group velocity of Rayleigh waves in the Antarctic region. *Physics of the Earth and Planetary Interiors* 122, 55–66 (cit. on pp. 107, 120).
- Danesi, S. and A. Morelli (2001). Structure of the upper mantle under the Antarctic Plate from surface wave tomography. *Geophysical Research Letters* 28(23), 4395–4398. DOI: [10.1029/2001gl013431](https://doi.org/10.1029/2001gl013431) (cit. on p. 120).
- Division, A. A. (2018). *Antarctic territorial claims*. Australian Government, Department of the Environment and Energy. URL: <http://www.antarctica.gov.au/territorial-claims/>

- gov.au/law-and-treaty/history/antarctic-territorial-claims (visited on 10/20/2018) (cit. on pp. 19, 20).
- Drewry, D. J. (1976). Sedimentary basins of the east antarctic craton from geophysical evidence. *Tectonophysics* 36(1-3), 301–314. DOI: [10.1016/0040-1951\(76\)90023-8](https://doi.org/10.1016/0040-1951(76)90023-8) (cit. on p. 22).
- Drewry, D. J. (1983). *Antarctica glaciological and geophysical folio*. Scott Polar Research Institute, University of Cambridge (cit. on p. 17).
- Dziewonski, A. M. and D. L. Anderson (1981). Preliminary reference Earth model. *Physics of the Earth and Planetary Interiors* 25(4), 297–356. DOI: [10.1016/0031-9201\(81\)90046-7](https://doi.org/10.1016/0031-9201(81)90046-7) (cit. on pp. 67, 68).
- Dziewonski, A. M., S. Bloch, and M. Landisman (1969). A Technique for the Analysis of Transient Seismic Signals. *Bulletin of the Seismological Society of America* 59(1), 427–444 (cit. on p. 71).
- Fretwell, P. et al. (2013). Bedmap2: improved ice bed, surface and thickness datasets for Antarctica. *The Cryosphere* 7(1), 375–393. DOI: [10.5194/tc-7-375-2013](https://doi.org/10.5194/tc-7-375-2013) (cit. on pp. 17, 20).
- Geopsy project* (2019). URL: <http://www.geopsy.org/> (visited on 2019) (cit. on p. 113).
- Haned, A., E. Stutzmann, M. Schimmel, S. Kiselev, A. Davaille, and A. Yelles-Chaouche (2016). Global tomography using seismic hum. *Geophysical Journal International* 204(2), 1222–1236. DOI: [10.1093/gji/ggv516](https://doi.org/10.1093/gji/ggv516). eprint: [/oup/backfile/content_public/journal/gji/204/2/10.1093/gji/ggv516/2/ggv516.pdf](http://oup/backfile/content_public/journal/gji/204/2/10.1093/gji/ggv516/2/ggv516.pdf) (cit. on p. 117).
- Harley, S. L. (2011). The geology of Antarctica. *Geology* 4, (cit. on pp. 21, 23).
- Hatherton, T. and F. F. Evison (1962). A special mechanism for some Antarctic earthquakes. *New Zealand Journal of Geology and Geophysics* 5(5), 864–873. DOI: [10.1080/00288306.1962.10417642](https://doi.org/10.1080/00288306.1962.10417642) (cit. on p. 28).
- Helffrich, G. R. and B. J. Wood (2001). The Earth's mantle. *Nature* 412(6846), 501–507. DOI: [10.1038/35087500](https://doi.org/10.1038/35087500) (cit. on p. 66).
- Herrmann, R. B. (2013). Computer Programs in Seismology: An Evolving Tool for Instruction and Research. *Seismological Research Letters* 84(6), 1081–1088. DOI: [10.1785/0220110096](https://doi.org/10.1785/0220110096) (cit. on p. 120).
- Himeno, T., M. Kanao, and Y. Ogata (2011). Statistical analysis of seismicity in a wide region around the 1998 Mw 8.1 Balleny Islands earthquake in

- the Antarctic Plate. *Polar Science* 5(4), 421–431. doi: [10.1016/j.polar.2011.08.002](https://doi.org/10.1016/j.polar.2011.08.002).
- Howat, I., P. Morin, C. Porter, and M.-J. Noh (2018). The Reference Elevation Model of Antarctica. doi: [10.7910/DVN/SAIK8B](https://doi.org/10.7910/DVN/SAIK8B) (cit. on p. 19).
- Institut de Physique du Globe de Paris (IPGP) and École et Observatoire des Sciences de la Terre (EOST) (1982). GEOSCOPE, French Global Network of broad band seismic stations. doi: [10.18715/GEOSCOPE.G](https://doi.org/10.18715/GEOSCOPE.G).
- Istituto Nazionale di Geofisica e Vulcanologia (INGV) (1990). Mediterranean Very Broadband Seismographic Network (MedNet). doi: [10.13127/SD/fBBtDtd6q](https://doi.org/10.13127/SD/fBBtDtd6q) (cit. on p. 29).
- Kaminuma, K. and M. Ishida (1971). Earthquake Activity in Antarctica. *Antarctica Record* 42, 53–60.
- Kanao, M. (2014). Seismicity in the Antarctic Continent and Surrounding Ocean. *Open Journal of Earthquake Research* 3(1), 5–14. doi: [10.4236/ojer.2014.31002](https://doi.org/10.4236/ojer.2014.31002) (cit. on p. 27).
- Krischer, L., T. Megies, R. Barsch, M. Beyreuther, T. Lecocq, C. Caudron, and J. Wassermann (2015). ObsPy: a bridge for seismology into the scientific Python ecosystem. *Computational Science & Discovery* 8(1), 014003. doi: [10.1088/1749-4699/8/1/014003](https://doi.org/10.1088/1749-4699/8/1/014003) (cit. on p. 76).
- Lander, J. F. (1959). Seismicity of Antarctica and Guam. *Seismological Research Letters* 30(2), 16–17. doi: [10.1785/gssrl.30.2.16b](https://doi.org/10.1785/gssrl.30.2.16b) (cit. on p. 28).
- Legovini, P.**, A. Morelli, and M. Schimmel (2017). Seismic tomography in Antarctica using ambient seismic noise. Poster. 3rd TIDES Advanced Training School, Oxford (UK).
- Legovini, P.**, A. Morelli, and M. Schimmel (2018a). Noise-based seismic tomography of Antarctica: data processing. Poster. 4th TIDES Advanced Training School, Prague (CZ).
- Legovini, P.**, A. Morelli, and M. Schimmel (2018b). Towards noise-based seismic tomography in Antarctica: data processing. Poster.
- Legovini, P.**, A. Morelli, and M. Schimmel (in preparation). Seismic Tomography of Antarctica using ambient seismic noise, (cit. on p. 99).
- Levshin, A., V. F. Pisarenko, and G. A. Pogrebinsky (1972). On a Frequency-Time Analysis of Oscillations. *Annales Geophysicae* 128(2), 211–218 (cit. on p. 71).

- Levshin, A., L. I. Ratnikova, and J. Berger (1992). Peculiarities of Surface Wave Propagation across Central Eurasia. *Bulletin of the Seismological Society of America* 82(6), 2464–2493 (cit. on p. 71).
- Lobkis, O. I. and R. L. Weaver (2001). On the emergence of the Green's function in the correlations of a diffuse field. *The Journal of the Acoustical Society of America* 110(6), 3011–3017. DOI: [10.1121/1.1417528](https://doi.org/10.1121/1.1417528) (cit. on p. 50).
- Lu, Y., L. Stehly, A. Paul, and AlpArray Working Group (2018). High-resolution surface wave tomography of the European crust and uppermost mantle from ambient seismic noise. *Geophysical Journal International* 214(2), 1136–1150. DOI: [10.1093/gji/ggy188](https://doi.org/10.1093/gji/ggy188) (cit. on pp. 55, 117).
- Macelloni, G., M. Brogioni, F. Montomoli, **P. Legovini**, and T. Casal (2015). Analysis of L-band brightness temperature time series at DOME C — Antarctica. *2015 IEEE International Geoscience and Remote Sensing Symposium (IGARSS)*. IEEE. DOI: [10.1109/igarss.2015.7326713](https://doi.org/10.1109/igarss.2015.7326713).
- Megies, T., M. Beyreuther, R. Barsch, L. Krischer, and J. Wassermann (2011). ObsPy – What can it do for data centers and observatories? *Annals of Geophysics* 54(1), ISSN: 2037-416X. DOI: [10.4401/ag-4838](https://doi.org/10.4401/ag-4838) (cit. on p. 76).
- Morelli, A. and S. Danesi (2004). Seismological imaging of the Antarctic continental lithosphere: a review. *Global and Planetary Change* 42(1–4), 155–165. DOI: [10.1016/j.gloplacha.2003.12.005](https://doi.org/10.1016/j.gloplacha.2003.12.005) (cit. on p. 120).
- Nicolson, H., A. Curtis, B. Baptie, and E. Galetti (2012). Seismic interferometry and ambient noise tomography in the British Isles. *Proceedings of the Geologists' Association* 123(1), 74–86. DOI: [10.1016/j.pgeola.2011.04.002](https://doi.org/10.1016/j.pgeola.2011.04.002).
- Nield, G. A., P. L. Whitehouse, W. van der Wal, B. Blank, J. P. O'Donnell, and G. W. Stuart (2018). The impact of lateral variations in lithospheric thickness on glacial isostatic adjustment in West Antarctica. *Geophysical Journal International* 214(2), 811–824. DOI: [10.1093/gji/ggy158](https://doi.org/10.1093/gji/ggy158) (cit. on p. 11).
- Nishida, K., J.-P. Montagner, and H. Kawakatsu (2009). Global Surface Wave Tomography Using Seismic Hum. *Science* 326(5949), 112–112. DOI: [10.1126/science.1176389](https://doi.org/10.1126/science.1176389) (cit. on pp. 55, 117).

- obspsy/CONTRIBUTORS.txt at master · obspsy/obspsy* (2018). ObsPy. URL: <https://github.com/obspsy/obspsy/blob/master/obspsy/CONTRIBUTORS.txt> (visited on 10/29/2018).
- Okal, E. A. (1981). Intraplate seismicity of antarctica and tectonic implications. *Earth and Planetary Science Letters* 52(2), 397–409. DOI: 10.1016/0012-821x(81)90192-8 (cit. on p. 28).
- Parish, T. R. and D. H. Bromwich (1991). Continental-Scale Simulation of the Antarctic Katabatic Wind Regime. *Journal of Climate* 4(2), 135–146. DOI: 10.1175/1520-0442(1991)004<0135:cssota>2.0.co;2 (cit. on p. 22).
- Poli, P., M. Campillo, and H. Pedersen (2012). Body-Wave Imaging of Earth's Mantle Discontinuities from Ambient Seismic Noise. *Science* 338(6110), 1063–1065. DOI: 10.1126/science.1228194.
- Poli, P., H. A. Pedersen, and M. C. and (2011). Emergence of body waves from cross-correlation of short period seismic noise. *Geophysical Journal International* 188(2), 549–558. DOI: 10.1111/j.1365-246x.2011.05271.x (cit. on p. 55).
- Programma Nazionale di Ricerche in Antartide (PNRA) (2015a). “Concordia Station Activity Report on the Antarctic Campaign. Winter 2014 — DC10” (cit. on pp. 33, 41).
- Programma Nazionale di Ricerche in Antartide (PNRA) (2015b). “Rapporto sulla Campagna Antartica. Estate Australe 2014–2015 — Trentesima spedizione” (cit. on p. 33).
- Programma Nazionale di Ricerche in Antartide (PNRA) (2016). “Rapporto sulla Campagna Antartica. Estate Australe 2015–2016 — Trentesima spedizione” (cit. on pp. 33, 38, 41).
- Reading, A. M. (2007). The seismicity of the Antarctic plate. *Special Paper 425: Continental Intraplate Earthquakes: Science, Hazard, and Policy Issues*. Geological Society of America, pp. 285–298. DOI: 10.1130/2007.2425(18) (cit. on pp. 25, 27, 28).
- Research Products from CU-Boulder* (2018). University of Colorado Boulder. URL: <http://ciei.colorado.edu/Products/> (visited on 10/20/2018) (cit. on pp. 76, 87).
- Ricaud, P., P. Grigioni, R. Zbinden, J.-L. Attié, L. Genoni, A. Galeandro, L. Moggio, S. Montaguti, I. Petenko, and P. Legovini (2015). Review

- of tropospheric temperature, absolute humidity and integrated water vapour from the HAMSTRAD radiometer installed at Dome C, Antarctica, 2009–14. *Antarctic Science* 27(06), 598–616. DOI: [10.1017/s0954102015000334](https://doi.org/10.1017/s0954102015000334).
- Ritzwoller, M. H., F.-C. Lin, and W. Shen (2011). Ambient noise tomography with a large seismic array. *Comptes Rendus Geoscience* 343(8-9), 558–570. DOI: [10.1016/j.crte.2011.03.007](https://doi.org/10.1016/j.crte.2011.03.007) (cit. on p. 55).
- Ronchi, C., R. Iacono, and P. Paolucci (1996). The Cubed Sphere: A New Method for the Solution of Partial Differential Equations in Spherical Geometry. *Journal of Computational Physics* 124(1), 93–114. DOI: [10.1006/jcph.1996.0047](https://doi.org/10.1006/jcph.1996.0047) (cit. on p. 105).
- Schaeffer, A. J. and S. Lebedev (2013). Global shear speed structure of the upper mantle and transition zone. *Geophysical Journal International* 194(1), 417–449. DOI: [10.1093/gji/ggt095](https://doi.org/10.1093/gji/ggt095) (cit. on p. 120).
- Schimmel, M. and J. Gallart (2007). Frequency-dependent phase coherence for noise suppression in seismic array data. *Journal of Geophysical Research: Solid Earth* 112(B4), DOI: [10.1029/2006jb004680](https://doi.org/10.1029/2006jb004680) (cit. on p. 58).
- Schimmel, M., E. Stutzmann, and J. Gallart (2011). Using instantaneous phase coherence for signal extraction from ambient noise data at a local to a global scale. *Geophysical Journal International* 184(1), 494–506. DOI: [10.1111/j.1365-246x.2010.04861.x](https://doi.org/10.1111/j.1365-246x.2010.04861.x) (cit. on pp. 56–58, 119).
- Schimmel, M. (1999). Phase cross-correlations: design, comparisons and applications. *Geophysical Journal International* 89(5), 1366–1378 (cit. on pp. 56, 119).
- Schimmel, M. (2018). *Martin Schimmel, ICTJA–CSIC, Barcelona, distinct results, pdfs & programs for download*. ICTJA–CSIC. URL: <http://diapiro.ictja.csic.es/gt/mschi/SCIENCE/tseries.html> (visited on 10/20/2018) (cit. on p. 76).
- Schimmel, M. and H. Paulssen (1997). Noise reduction and detection of weak, coherent signals through phase-weighted stacks. *Geophysical Journal International* 130(2), 497–505. DOI: [10.1111/j.1365-246x.1997.tb05664.x](https://doi.org/10.1111/j.1365-246x.1997.tb05664.x) (cit. on p. 57).
- Schivardi, R. and A. Morelli (2009). Surface wave tomography in the European and Mediterranean region. *Geophysical Journal International* 177(3), 1050–1066. DOI: [10.1111/j.1365-246x.2009.04100.x](https://doi.org/10.1111/j.1365-246x.2009.04100.x) (cit. on pp. 105, 106).

- Schivardi, R. and A. Morelli (2011). EPmantle: a 3-D transversely isotropic model of the upper mantle under the European Plate. *Geophysical Journal International* 185(1), 469–484. DOI: [10.1111/j.1365-246x.2011.04953.x](https://doi.org/10.1111/j.1365-246x.2011.04953.x) (cit. on p. 105).
- Shapiro, N. M. (2005). High-Resolution Surface-Wave Tomography from Ambient Seismic Noise. *Science* 307(5715), 1615–1618. DOI: [10.1126/science.1108339](https://doi.org/10.1126/science.1108339) (cit. on pp. 46, 51, 55).
- Shapiro, N. M. and M. Campillo (2004). Emergence of broadband Rayleigh waves from correlations of the ambient seismic noise. *Geophysical Research Letters* 31(7), n/a–n/a. DOI: [10.1029/2004gl019491](https://doi.org/10.1029/2004gl019491) (cit. on p. 46).
- Stehly, L., M. Campillo, and N. M. Shapiro (2006). A study of the seismic noise from its long-range correlation properties. *Journal of Geophysical Research* 111(B10), DOI: [10.1029/2005jb004237](https://doi.org/10.1029/2005jb004237) (cit. on p. 47).
- Stein, S. and M. Wysession (2003). *Introduction to Seismology, Earthquakes, and Earth Structure*. English. Blackwell Publishing. ISBN: 978-1-118-68745-1 (cit. on pp. 49, 64, 65).
- Stockwell, R. G., L. Mansinha, and R. P. Lowe (1996). Localization of the complex spectrum: the S transform. *IEEE Transactions on Signal Processing* 44(4), 998–1001. DOI: [10.1109/78.492555](https://doi.org/10.1109/78.492555) (cit. on p. 58).
- Stonehouse, B. (2002). *Encyclopedia of Antarctica and the Southern Oceans*. Wiley. ISBN: 0471986658 (cit. on p. 19).
- Tange, O. (2018). *Gnu Parallel 2018*. en. Zenodo. DOI: [10.5281/zenodo.1146014](https://doi.org/10.5281/zenodo.1146014) (cit. on p. 77).
- Tarantola, A. (2005). *Inverse Problem Theory and Methods for Model Parameter Estimation*. SIAM. ISBN: 978-0-89871-572-9. DOI: [10.1137/1.9780898717921](https://doi.org/10.1137/1.9780898717921) (cit. on pp. 100, 101, 120).
- Tsuboi, S., M. Kikuchi, Y. Yamanaka, and M. Kanao (2000). The March 25, 1998 Antarctic Earthquake: Great earthquake caused by postglacial rebound. *Earth, Planets and Space* 52(2), 133–136. DOI: [10.1186/bf03351621](https://doi.org/10.1186/bf03351621).
- Turner, J., P. Anderson, T. Lachlan-Cope, S. Colwell, T. Phillips, A. Kirchgassner, G. J. Marshall, J. C. King, T. Bracegirdle, D. G. Vaughan, V. Lagun, and A. Orr (2009). Record low surface air temperature at Vostok station, Antarctica. *Journal of Geophysical Research* 114(D24), DOI: [10.1029/2009jd012104](https://doi.org/10.1029/2009jd012104) (cit. on p. 22).

- United States Geological Survey (2018). *Landsat Image Mosaic Of Antarctica*. URL: <https://lima.usgs.gov/> (visited on 10/20/2018) (cit. on p. 18).
- Ventosa, S. (2018). *Time-scale phase-weighted stack software for seismic signal denoising*. ICTJA–CSIC. URL: <https://github.com/sergiventosa/ts-PWS> (visited on 10/20/2018) (cit. on pp. 76, 90).
- Ventosa, S., M. Schimmel, and E. Stutzmann (2017). Extracting surface waves, hum and normal modes: time-scale phase-weighted stack and beyond. *Geophysical Journal International* 211(1), 30–44. DOI: [10.1093/gji/ggx284](https://doi.org/10.1093/gji/ggx284) (cit. on p. 90).
- Wapenaar, K. (2004). Retrieving the Elastodynamic Green’s Function of an Arbitrary Inhomogeneous Medium by Cross Correlation. *Physical Review Letters* 93(25), DOI: [10.1103/physrevlett.93.254301](https://doi.org/10.1103/physrevlett.93.254301) (cit. on pp. 50, 51).
- Wathelet, M. (2008). An improved neighborhood algorithm: Parameter conditions and dynamic scaling. *Geophysical Research Letters* 35(9), DOI: [10.1029/2008gl033256](https://doi.org/10.1029/2008gl033256) (cit. on p. 113).
- Weaver, R. L. (2005). Information from Seismic Noise. *Science* 307(5715), 1568–1569. DOI: [10.1126/science.1109834](https://doi.org/10.1126/science.1109834) (cit. on pp. 46, 52).
- Wessel, P., W. H. F. Smith, R. Scharroo, J. Luis, and F. Wobbe (2013). Generic Mapping Tools: Improved Version Released. *Eos, Transactions American Geophysical Union* 94(45), 409–410. DOI: [10.1002/2013eo450001](https://doi.org/10.1002/2013eo450001) (cit. on p. 77).
- Wiens, D. and A. Nyblade (2007a). A Broadband Seismic Experiment to Image the Lithosphere beneath the Gamburtsev Mountains, East Antarctica. DOI: [10.7914/sn/zm_2007](https://doi.org/10.7914/sn/zm_2007) (cit. on p. 28).
- Wiens, D. and A. Nyblade (2007b). IPY POLENET-Antarctica: Investigating links between geodynamics and ice sheets. DOI: [10.7914/sn/yt_2007](https://doi.org/10.7914/sn/yt_2007) (cit. on p. 29).
- Yan, P., Z. Li, F. Li, Y. Yang, W. Hao, and F. Bao (2018). Antarctic ice sheet thickness estimation using the horizontal-to-vertical spectral ratio method with single-station seismic ambient noise. *The Cryosphere* 12(2), 795–810. DOI: [10.5194/tc-12-795-2018](https://doi.org/10.5194/tc-12-795-2018) (cit. on p. 30).
- Yao, H., C. Beghein, and R. D. van der Hilst (2008). Surface wave array tomography in SE Tibet from ambient seismic noise and two-station analysis - II. Crustal and upper-mantle structure. *Geophysical Journal*

International 173(1), 205–219. DOI: [10.1111/j.1365-246x.2007.03696.x](https://doi.org/10.1111/j.1365-246x.2007.03696.x)
(cit. on p. 55).

Yao, H., R. D. van der Hilst, and M. V. de Hoop (2006). Surface-wave array tomography in SE Tibet from ambient seismic noise and two-station analysis - I. Phase velocity maps. *Geophysical Journal International* 166(2), 732–744. DOI: [10.1111/j.1365-246x.2006.03028.x](https://doi.org/10.1111/j.1365-246x.2006.03028.x) (cit. on p. 55).